The Investigation of Spin Effects in

(e,2e) Collisions

A thesis submitted for the degree of Doctor of Philosophy of

The Australian National University.

by

Joanne May Hurn, B.Sc.(Hons)

in the

Electron Physics Group

Atomic and Molecular Physics Laboratories

Research School of Physical Sciences and Engineering

The Australian National University

(http://rsphysse.anu.edu.au/~sjb107/AMPL.HTML)

May 1996

Dedicated to my Mum and Dad for their continued support and love and Trevor and Judith for welcoming me into their family.
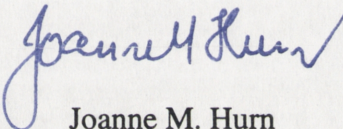
Most of all this is dedicated to my partner Graeme, whom has always believed in my abilities and in our dreams. Thankyou, Graeme.

"Women hold up half the sky" Ancient Chinese saying.

(from Baltimore Charter for Women in Astronomy, http://stsci.edu/pubinfo/BaltoCharter.html).

Declaration

I certify that this thesis does not incorporate without acknowledgment any material previously submitted for a degree or diploma in any university; and that to the best of my knowledge and belief it does not contain any material previously published or written by another person except where due reference is made in the text.

Joanne M. Hurn

Acknowledgments

Abstract

Experimental atomic physics has used electron-atom collisions and specifically the (e,2e) technique for many decades. An (e,2e) experiment involves firing an electron beam at a target and mapping the momenta of the two outgoing electrons in coincidence. It is used to probe the structure of a target or to investigate the ionisation processes. This information is of use for many reasons, it improves the understanding of reactions in the upper atmosphere, plasma formation, gas discharge and laser physics.

The experimental technique involves a multiparameter detection system, *i.e.*, data is gathered over a range of outgoing energies simultaneously. Here electrons are passed though an energy-dispersing element before impinging on a position sensitive detector which determines spatial coordinates of the detected electrons. The PSD consists of chevron mounted multichannel plates followed by a position sensitive resistive anode. This type of experiment has been performed previously, *e.g.*, Lower and Weigold (1989) and is widely used.

It is possible to gather more information from (e,2e) collisions by using well defined targets or projectiles, to investigate spin effects in electron-atom collisions. In this case, a polarised electron source is used, *i.e.*, the electrons have a preferred spin. This allows for a more detailed examination of the ionisation process. Previous experiments have shown that spin asymmetries are observable in certain conditions, *i.e.*, low energy elastic scattering. Preliminary results in Granitza *et al.* (1993) showed that asymmetries are measurable for ionisation in an (e,2e) experiment at an intermediate energy. In this work experiments are performed which further demonstrate that spin effects are observable as spin asymmetries in xenon ($5p^5$ $^2P_{1/2}$ and $^2P_{3/2}$ states) at an incident energy of 147eV, for scattered, fixed angles of $\theta_s = 28°$, 15° and 40° at 100eV and at 35eV for the ejected, scanned angle. This spin effect is explained via the analogue to the "fine-structure effect". This fine-structure effect has been observed in excitation processes as a spin asymmetry, *e.g.* Hanne (1983).

The results are presented as cross sections, (total, state resolved and spin resolved), asymmetries and branching ratios. This work confirms the use of polarised electrons in (e,2e) collisions as a powerful tool for unraveling competing spin and non-spin dependent effects in the ionisation process. Some of the effects are clearly dependent upon the dynamics of the reaction mechanism, and others, such as the branching ratio, depend largely on the details of the target wave function.

Contents

Chapter 1

Introduction

Electron-atom collisions have been used in atomic physics to improve the understanding of such things as the details of the upper atmosphere, plasma formation, gas discharge and laser physics. There are various methods used in experimental studies of electron-atom collisions, including for example, the 'crossed beam' experiments, where a single electron is detected after elastic scattering, or an excitation or ionisation event (Gulley *et al.*, 1994), coincidence experiments, which detect an electron-photon coincidence and (e,2e) experiments (McCarthy and Weigold, 1976). An (e,2e) experiment is a kinematically complete electron impact ionisation measurement which detects two outgoing electrons from the same scattering event in coincidence. This work employs the (e,2e) technique.

The (e,2e) experiment was an innovative technique introduced to atomic physics almost three decades ago (Amaldi *et al.*, 1969 and Ehrhardt *et al.*, 1969). The (e,2e) experiment can gather more information by using a spin polarised electron source, thereby improving the power of electron-atom collision experiments. Various sources of producing polarised electrons have been researched see *e.g.*, Kessler (1985) and Gay (1983). Pierce *et al.* (1975) were the first to measure spin polarisation of photoemitted electrons from a non-magnetic semiconductor. The experiment for this work utilises a spin polarised electron source based of the type of Pierce, Meier and Zürcher (1975) and Pierce *et al.* (1980). A polarised electron source alone is of little advantage, unless the polarisation of the electron beam can be determined. A popular method to measure the polarisation of electron beams is to employ a so called "Mott polarimeter" (*e.g.*, Hodge *et al.*, 1979 and Gay and Dunning, 1992a).

The primary aim of the experiments described here is to test the validity of theoretical models describing electron-atom collision processes. In an (e,2e) experiment, where the kinematics of the collision partners are known, simply determining the differential cross sections is not always enough to stringently test a theory. Previously, (e,2e) experiments have provided a good testing ground for the theory. The electron-atom collision is a many body problem, but it is often treated as a three body problem, governed by the long range Coulomb interaction. An (e,2e) experiment with a hydrogen target is exactly the three body problem. Solutions to this three body problem are found by solving the Schrödinger equation with correct asymptotic boundary conditions. This

is not a trivial task and generally requires an appropriate choice of approximations. In such experiments if an averaging process, such as the spin orientation of the projectile or target, is removed, the theory would be tested more rigorously.

The work in this thesis does just that. By conducting an (e,2e) experiment using a polarised electron beam, the sum over the intrinsic angular momentum (spin) of the incident particle is removed. Hence, the theories need to resolve the spin channel of the scattering event to describe the (e,2e) experiment. Typically in experiments investigating spin effects, a spin dependent asymmetry is observed. That is, the cross section of an event may differ depending on the spin orientation the particles involved in the collision. Observing a spin asymmetry implies observing a ratio of the scattered intensities, hence measurements of absolute target densities and absolute scattering intensities, are not required in polarisation measurements. 'Complete scattering experiments' as first suggested by Bederson (1969) aim to measured all channels of the electron-atom collision, in which the states of the collision partners are well defined before and after the collision. These types of experiments are not yet generally possible, however experiments which involve spin polarised electrons are being conducted in various laboratories *e.g.*, Hanne (1983), Baum *et al.* (1985) and Shi *et al.* (1996). These experiments will be commented on later in this chapter.

The level of sophistication of the theory has gradually increased in recent years. In electron-atom collision experiments, large numbers of independent parameters are measurable. Furthermore, there is a wide range of different experimental arrangements which theorists are required to assimilate with available theoretical models. The general density matrix formalism (Bartschat, 1992) is a framework from which a systematic description of the scattering process is possible. The density matrix formalism is an invaluable tool for theorists, as it can describe many different aspects of an experiment within the same formalism, using appropriate approximations for certain conditions.

Many experiments have been performed which consider polarisation effects (see Kessler (1985) for a full review). The work of McClelland, Kelley and Celotta (1987) is an example of spin polarised experiments. That experiment measured spin-orbit and exchange effects in elastic scattering from sodium, where both collision partners (target and projectile) were polarised. The results for the sodium atom were presented as spin and exchange asymmetries. The data does show evidence of an asymmetry and the agreement with theory is reasonable. Shi *et al.* (1996) have recently reported the first azimuthal asymmetries for elastic scattering from sodium. The experiment reported by Shi *et al.* (1996) found asymmetries, due to the Coulomb interaction, of the order of 0.3, for incident electron energies below 5eV. Spin asymmetries have also been measured for alkali atoms such as lithium and potassium, (Zhang *et al.*, 1992 and references therein). Exchange effects in chromium have also been studied (Hanne *et al.*, 1993), at low energies in a superelastic scattering experiment. Spin dependent polarisation effects had been observed in superelastic scattering from sodium (Nickich *et al.*, 1990). In this experiment a polarised electron beam was superelastically scattered from laser-excited unpolarised sodium atoms. This was a low energy experiment (6 - 20eV), where spin asymmetries were observed.

Polarisation effects have also been reported by Sohn and Hanne (1992) for excitation of mercury (Hg*(6³P₁)). This is an electron-photon, (e,eγ) coincidence experiment, where an electron and photon are detected in coincidence. An (e,eγ) coincidence experiment conventionally obtains information on the magnetic sub-levels of the excited atom. However, the inclusion of a spin polarised electron beam as in the (e,eγ) experiment of Sohn and Hanne (1992), implies that the reflection symmetry in the scattering plane is, in general, broken. Consequently, the charge-cloud distribution may be tilted by an angle ε, with respect to the scattering plane (Hanne, 1992). The charge cloud, with anisotropically populated atoms, emits linearly polarised photons and measurement of these photons yields parameters which can characterise the anisotropic charge cloud distribution (Hanne, 1992).

In the experiment conducted by Sohn and Hanne (1992), differential Stokes parameters (*i.e.*, photon polarisation components) were determined at low incident energies (8eV and 15eV). The results were compared to an R-matrix calculation, where agreement was good at the lower energy, but was not satisfactory at 15eV. The (e,eγ) coincidence experiment was also used by Uhrig, Hanne and Kessler (1994) to study the polarisation of the resonance lines in xenon. The polarisation results of this experiment were presented as integrated Stokes parameters and as a spin up-down asymmetry. Both of these experiments were low energy electron impact excitation studies which proved to be effective in examining spin effects in inelastic electron-atom collisions.

Garcia-Rosales, Müller and Kessler (1988) showed strong polarisation effects are observed in low energy elastic scattering and excitation for heavier atoms. This experiment was conducted to measure the Sherman function for xenon, by two different methods, a polarisation measurement and an asymmetry measurement. The first method analysed electrons which were elastically scattered from a xenon target in a Mott detector. In the second method, polarised electrons were elastically scattered from a xenon target and the asymmetry was measured. These experiments were conducted at low energy (30eV), both gave similar results for the Sherman function. Other experiments have been performed using polarised electron sources and noble gases, *e.g.*, Dümmler *et al.* (1990) and Berger and Kessler (1986). Dümmler *et al.* (1995) observed spin dependent effects (left-right asymmetries) in argon, krypton and xenon in low energy excitation experiments. Berger and Kessler (1986) measured the change in the polarisation of the polarised incident electron beam when elastically scattered from mercury and xenon (the S, T, U parameters). These experiments were conducted in the intermediate energy regime, (40 - 350eV). It was found that the complete set of observables (*i.e.*, S, T, U parameters, the absolute differential cross section and the moduli and relative phase of the scattering amplitudes) is needed to stringently test the theory.

The first (e,2e) spin polarised ionisation experiment investigated the competing processes of direct and exchange scattering. Baum *et al.* (1992) achieved this by scattering a low energy (54.4eV) polarised electron beam from a beam of polarised lithium atoms. By performing the experiment with a light target, it was possible to examine the scattering process under conditions where the spin-orbit interaction of the continuum electrons in the atomic and ionic fields is negligible.

Another recent spin polarised (e,2e) ionisation experiment by Prinz *et al.* (1995) measured spin asymmetries for ionisation of *K*-shell electrons in unpolarised silver atoms by high energy (300keV) polarised electrons. This experiment shows that large spin asymmetries result from the spin-orbit interaction of the continuum electrons.

Geesmann *et al.* (1991) performed low energy elastic and inelastic scattering experiments from heavy target systems. The targets in this case were unpolarised thallium and lead atoms. This showed that at these low energies, the fine-structure effect was the dominant spin effect, which resulted in spin dependent asymmetries. This fine-structure effect is discussed below.

Polarisation effects are usually caused by more than one spin dependent interaction. Spin effects caused by only one spin dependent interaction are the exception. It is known that exchange, in conjunction with the atomic fine-structure interaction, is responsible for spin effects in inelastic collisions of slow electrons, (Hanne, 1983). Later, Hanne (1992) indicated that the fine-structure effect was apparent in excitation processes. It was postulated that this polarisation effect could be observed in ionisation processes. The theory for the fine-structure effect must consider limiting conditions which fulfill the following requirements, a) neglecting the spin-orbit interaction and b) assuming that the internal spin-orbit coupling of the target is weak and therefore the LS coupling scheme is valid (Kessler, 1991).

The work in this thesis proposes that the fine-structure effect is observable in an (e,2e) experiment, where a polarised electron beam is used to study the ionisation processes in the xenon atom. These experiments demonstrate that the conditions required for measuring this effect are achievable. That is, in the absence of any explicit spin dependent forces and if,
a) the angular momentum of the target is non-vanishing, *i.e.*, $\langle L \rangle \neq 0$, the orbital angular momentum is orientated after a collision (Anderson, Gallagher and Hertel, 1988),
b) electron exchange is possible during the electron-atom collision
and c) the fine structure states of the $5p$ ionisation level of xenon are resolvable by the experimental apparatus employed.
If this can be done, then the polarisation effects should be observed as a measurable spin up-down asymmetry in the cross section.

Following this introduction, chapters 2 and 3 discuss the theoretical details of the experiment. Chapter 2 begins with the (e,2e) theory which is the building block of this work. The last sections of chapter 2 describe the physics behind polarisation phenomena, including using Mott scattering as an analysis tool. The theory in chapter 3 concentrates on the inclusion of the spin of the electron and the introduction of the density matrix formalism. In this chapter 3, exchange, spin-orbit interaction and the fine-structure effect are discussed. It is this fine-structure effect which this experiment aims to verify.

The experimental apparatus is reported in chapter 4. This chapter comprises of all relevant practical aspects of the experiment, including the polarised electron source, the Mott polarimeter and the (e,2e) spectrometers. In addition to a description of the hemispherical analysers and multichannel plates which are used to detect the two outgoing electrons in coincidence, there is a discussion of the electronics associated with

the coincidence circuit. Schematic diagrams of the experimental apparatus and selected parts of the apparatus are included here, along with typical energy and timing spectra.

Chapter 5 introduces the results and the details of the theoretical calculations which are used as a comparison. The kinematics and the experimental conditions are also outlined in this chapter. It is in this chapter that the observables of the experiment are given, the cross sections, asymmetries and branching ratios are all shown and accompanied by a discussion of these results. This chapter also includes details of the data analysis.

Finally in chapter 6, a summary is presented. This summary briefly recaps the two theories used for comparisons, the experimental aspect and the data analysis involved in this work. This chapter concludes this work with some suggestions about the future direction of these experiments.

Chapter 2

Theoretical Considerations

In experimental physics it is essential to consider the relevant theory, so that the information gathered from the experiment can be optimised. That is, the theory guides the experiment to areas of interest and which may be measurable. The experiment then in turn indicates where further improvements are required (it is therefore an iterative process). Thus improving the understanding of atomic systems. This chapter presents a general introduction to the theory of (e,2e) collisions. A more detailed look at this theory will be presented in chapter three, where a spin component will be included. Good reviews can be found in Stefani *et al.* (1993) and McCarthy and Weigold (1995), for more insight into the details of atomic physics and (e,2e) experiments. This thesis is restricted to only that theory which is relevant to the experimental work. The final stages of this chapter detail the theory concerned with the generation and analysis of polarised electron beams.

Section 2.1   The (e,2e) Reaction

(e,2e) theory evolved from (p,2p) theory in nuclear physics almost three decades ago and has since been successfully used as a spectroscopic tool in atomic physics. The (e,2e) technique has been used in a variety of situations, most notably for studying ionization processes and target structure. At high energies and high momentum transfers the ionisation mechanism is well understood and it has been used extensively to describe the electronic structure of many atoms, from the simplest one electron atoms (H, Na) to more complex atoms such as xenon. Molecules have also been studied using this technique (Samardzic *et al.*, 1993 and Zheng *et al.*, 1995) and more recently this type of experiment has been extended to include solids, *e.g.*, amorphous carbon (Vos *et al.*, 1995).

Essentially the (e,2e) experiment is firing a beam of electrons at a target and detecting two outgoing electrons in coincidence. There are three possible reactions, either the target electron may be excited, (excitation) or knocked out, (ionisation) and of course elastic scattering is possible. It is the ionisation reaction which is studied in this work. The two outgoing electrons are selected by energy and although they are

indistinguishable, they are labelled as a fast, scattered electron and a slow, ejected electron. Conventionally $E_s > E_e$. The ionisation reaction is expressed as:

$$e + A \rightarrow e_e + e_s + A^+ . \qquad \qquad ... 2.1$$

In such a reaction the kinematics (shown in figure 2.1) are complete and must obey the law of conservation of energy:

$$E_0 = E_s + E_e + \varepsilon , \qquad \qquad ... 2.2$$

where E_0 is the incident energy and ε is the binding energy (here the kinetic energy of the ion is assumed to be negligible). The reaction must also obey the law of conservation of momentum

$$\mathbf{k}_0 = \mathbf{p} + \mathbf{k}_s + \mathbf{k}_e , \qquad \qquad ... 2.3$$

where $\mathbf{k}$ is the momentum and the subscript 0 represents the incoming electron and s, e are the scattered and ejected electron respectively and $\mathbf{p}$ is the ion recoil momentum.

Usually the momentum transfer is defined as

$$\mathbf{K} = \mathbf{k}_0 - \mathbf{k}_s , \qquad \qquad ... 2.4$$

which is often fixed in an (e,2e) experiment. The momentum transfer may also be used to classify experiments.
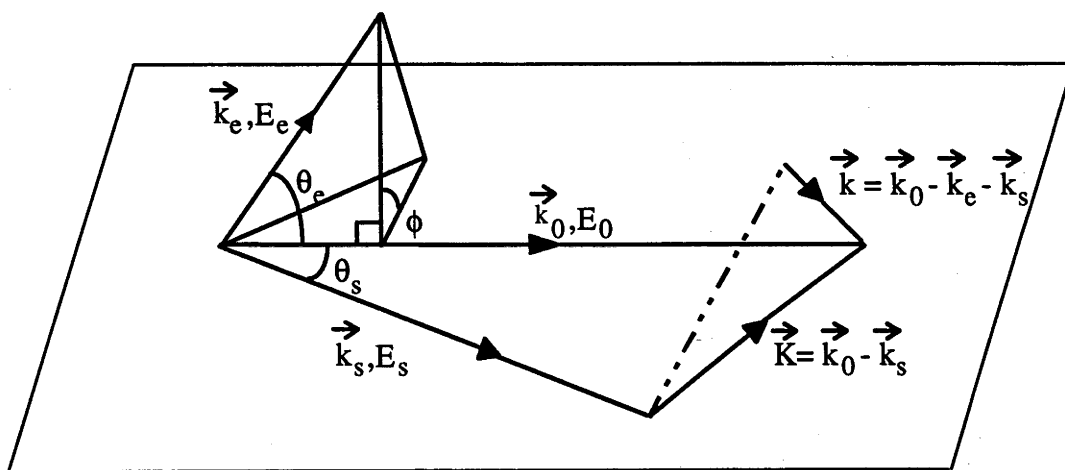
Figure 2.1: The kinematics of an (e,2e) reaction where the subscripts, 0, s, and e represent the incoming electron, scattered and ejected electron respectively.

There are two general categories of (e,2e) experiments, which reveal information on either the target and it's structure or the ionisation process. The former category involves high energy, high momentum transfer collisions and is known as electron momentum spectroscopy, (EMS) (McCarthy and Weigold, 1976, 1988). The study of ionisation processes generally utilises low energy asymmetric kinematics, which forms

the basis of this work. Typically, coplanar asymmetric experiments are performed with low or intermediate energies (*i.e.*, small **K**) so that the dynamics of the collision can be fully investigated. The present work is done at small momentum transfer with intermediate energies. In this case, intermediate energy means approximately ten times the ionisation energy. An abundance of experimental data exists for a vast range of kinematical regions and targets which are used to test the validity of the theoretical approximations. However, there is still little data available for spin resolved experiments, which is the topic of this work and will be discussed in chapter 3.

Section 2.2   Theoretical Approximations

There are many forms of approximations for theoretical calculations which have been developed parallel with the (e,2e) experimental techniques. For example, the binary encounter approximation (BEA), plane wave impulse approximation (PWIA), the target Hartree-Fock approximation (THFA), the distorted wave Born approximation (DWBA) and the Brauner, Briggs and Klar approximation (BBK) are but a few. Detailed descriptions of these can be found elsewhere, (*e.g.*, McCarthy and Weigold, 1976, 1991a, Bray and Stelbovics, 1995) however, a brief outline of some of these theories is warranted.

All of the calculations attempt to solve the same many-body problem, but they differ in the techniques used to approximate the solutions. For an (e,2e) reaction, the many body problem in the final state consists of an ion and two electrons. Generally, this is reduced to a two body problem so that it can be solved. However, as the governing potential is Coulombic and is of infinite range, this assumption is not strictly true. The complete three body problem has been tackled by Brauner, Briggs and Klar and will be discussed later.

The triple differential cross section (or (e,2e) cross section) for an uncharged system with an electron bound to the core in the state α, is (McCarthy, 1995):

$$\frac{d^5\sigma}{d\Omega_s d\Omega_e dE_s} = (2\pi)^4 \frac{k_s k_e}{k_0} \sum_{av} |\langle k_s k_e | T | \alpha k_0 \rangle|^2, \qquad \dots 2.5$$

where the subscripts, 0, s and e refer to the incident and the final state continuum electrons respectively. Atomic units are used in this description, $\hbar = m_e = e = 1$. The symbols Ω_s and Ω_e denote the solid angles of emission for both final state electrons and E_s is the energy of one of the final state electrons. $\sum$ indicates a sum over final states and an average over initial state magnetic and spin degeneracies. T is the unknown transition operator representing the transition amplitude for the ionization process from an initial state, α, and is defined as,

$$T_{f0}(k_e, k_s, k_0) = \langle k_s k_e | T | \alpha k_0 \rangle. \qquad \dots 2.6$$

The main approximation in these theories is in the T operator.

According to formal scattering theory,

$$\langle k_s k_e | T | \alpha k_0 \rangle = \langle \psi^{(-)} | V | \alpha k_0 \rangle = \langle k_s k_e | V | \psi^{(+)} \rangle \qquad \ldots 2.7$$

where V is the scattering potential, $\psi^{(-)}$ is the exact final state with final state boundary conditions and $\psi^{(+)}$ is the exact initial state with initial state boundary conditions. Of course these wave functions need to be approximated as they cannot be determined exactly. They must however, satisfy the following Schrödinger equations:

$$(H-E) | \psi^{(-)} \rangle = 0 , \qquad \ldots 2.8a$$

$$(H-E) | \psi^{(+)} \rangle = 0 \qquad \ldots 2.8b$$

where the Hamiltonian, H is,

$$H = K_1 + v_1 + K_2 + v_2 + v_3 , \qquad \ldots 2.9$$

where K_1 and K_2 are the kinetic energies of the electrons, v_1 and v_2 are the electron-ion potentials and v_3 ($= 1/r_{12}$) is the electron-electron potential. Equations 2.8 represent two different approaches to this problem, where the BBK considers equation 2.8a (see later this chapter) and for example, the convergent close coupling (CCC), which approximates for the infinite expansion of the target states, (Bray *et al.*, 1991) solves for equation 2.8b. The scattering amplitude is f(k′,k) and is represented by:

$$f(k', k) = \frac{-m}{2\pi\hbar^2} (2\pi)^3 T(k', k). \qquad \ldots 2.10$$

An example of an approximation of the T matrix can be seen in the binary encounter approximation. Here the T matrix is given by

$$T_{f0}(k_s, k_e, k_0) = \langle k_s k_e f | t | 0 k_0 \rangle , \qquad \ldots 2.11$$

where t is the operator for a two electron collision. This case is assumed to be valid if the momentum transfer, **K**, is large and the collision can be presumed to be between the incident electron and one target electron.

If the potential is much smaller than the kinetic energy then it may be treated as a perturbation, then in the Lipmann-Schwinger formulation the T operator may be perturbated in the following manner (in Dirac notation),

$$T(k, k') = \langle k' | U | k \rangle + \langle k' | UG_0 U | k \rangle + \langle k' | UG_0 UG_0 U | k \rangle + \ldots \qquad \ldots 2.12$$

where U is the general form of the potential and G represents the usual Greens functions (see *e.g.*, McCarthy and Weigold, 1976). This equation is known as the Born series. The first term gives the Born approximation to the transition amplitude.

As the first Born approximation (FBA) is a first order calculation which uses plane waves and a one electron wave function for the target, it is too simple to give satisfactory results except at very high energies. The FBA is most applicable in the high energy regimes. To improve this approximation it is then necessary to consider other factors arising from the electron-atom collisions. This means including the distortion of the incident electron due to the target potential, the free particles due to the ionic potential and the effects of electron-electron correlation in the final state. This leads to further approximations, such as the second Born approximation (SBA) which considers the second order of the iteration of the incident electron with the target electron.

An extension to the Born approximation is the distorted wave Born approximation (DWBA). This treats the potentials to all orders in the Born series (equation 2.12) although it omits an infinite set of different terms. The DWBA is generated by replacing the plane wave, $|k\rangle$ in equation 2.12, by a distorted wave for the incident state and similarly replacing the plane wave, $|k'\rangle$, with a time-reversed wave:

$$T(\mathbf{k}',\mathbf{k}) = \left\langle \chi^{(-)}(\mathbf{k}_s)\chi^{(-)}(\mathbf{k}_e)\Psi^{ion} \left| V \right| \Psi_i^f \chi^{(+)}(\mathbf{k}) \right\rangle. \qquad \dots 2.13$$

The DWBA does not work well in the kinematical region where the two-final state electrons remain close to each other for long enough that their long range repulsion is significant. That is, the DWBA does not have correct boundary conditions or account for electron-electron interactions.

Plane wave impulse approximation (PWIA) is one of the simplest of the approximations used to describe the (e,2e) reaction and is most commonly applied in EMS experiments. It's validity is limited to the region near where Bethe-Ridge conditions hold, that is, where $k_e^2 = K_e^2$ and the momentum transfer is high. The electron-atom collision becomes a two body electron-electron collision and is known as an impulse approximation. The PWIA transition amplitude factorises to give,

$$T_{f0}\left(\mathbf{k}_s,\mathbf{k}_e,\mathbf{k}_0\right)=\left\langle \mathbf{k}' \left| t_{sp} \right| \mathbf{k} \right\rangle \left\langle \mathbf{k}_s \mathbf{k}_e\, f \left| 0\mathbf{k}_0 \right. \right\rangle, \qquad \dots 2.14$$

where t_{sp} denotes the antisymmetric t-operator for two electrons with spin S at a relative collision energy corresponding to $\mathbf{k}'$ (McCarthy and Weigold, 1991a) and

$$\mathbf{k}'=\frac{1}{2}(\mathbf{k}_s - \mathbf{k}_e), \quad \mathbf{k}=\frac{1}{2}(\mathbf{k}_0 - \mathbf{q}) \quad \text{and} \quad \mathbf{q}=\mathbf{k}_0 - \mathbf{k}_s - \mathbf{k}_e = -\mathbf{p}.$$

The distorted wave impulse approximation (DWIA) is when incoming and outgoing waves can no longer be treated as plane waves. In this approximation, the plane wave, $|k\rangle$ is replaced by the distorted wave, $|\chi^{(\pm)}(\mathbf{k})\rangle$ which takes into account the distortion of the incident and outgoing waves by the potential of the remaining system. The T matrix becomes:

$$T_{f0}(\mathbf{k}_s,\mathbf{k}_e,\mathbf{k}_0)=\left\langle \mathbf{k}' \left| t_{sp} \right| \mathbf{k} \right\rangle \left\langle \chi^{(-)}(\mathbf{k}_s)\chi^{(-)}(\mathbf{k}_e)f \left| 0\chi^{(+)}(\mathbf{k}_0) \right. \right\rangle. \qquad \dots 2.15$$

In this approximation the target and ion structure appear only in the form of the ion-target overlap $\langle f | 0 \rangle$, which is a one electron function. It should be noted here that the DWIA gives correct results for (e,2e) experiments at high energy under Bethe-Ridge conditions, but is generally not expected to be valid far off the Bethe-Ridge.

Consider further the structure overlap. This may be studied using the one-electron model of the target, constructed from the well known Hartree-Fock orbitals and representing the ion by the same model with one hole in the ith orbital. The overlap can be expanded in the independent particle configurations, ϕ_α of the target (McCarthy and Weigold, 1988),

$$\Psi_0^N = \sum_\alpha a_\alpha^{(0)} \phi_\alpha , \qquad \qquad ... 2.16$$

$$\Psi_f^{N-1} = \sum_{j\alpha} t_{j\alpha}^{(f)} \left(C_{j\alpha} \psi_j^+ \phi_\alpha \right) , \qquad \qquad ... 2.17$$

where the preferred basis for the target in an (e,2e) experiment is the Hartree-Fock target basis. The linear expansion of the ion state, f, in equation 2.17, demonstrates the coupling of a hole in the orbital j, to a target configuration, ϕ_α by a Clebsch-Gordan coefficient, $C_{j\alpha}$. Then the overlap amplitude is

$$\left\langle q \, \Psi_f^{N-1} \middle| \Psi_0^N \right\rangle = \sum_{j\alpha} a_\alpha^{(0)} t_{j\alpha}^{(f)} C_{j\alpha} \left\langle q \middle| \psi_j \right\rangle . \qquad \qquad ... 2.18$$

The overlap amplitude is given by a sum of momentum space orbitals, ψ_j,

$$\psi_j(q) \equiv \left\langle q \middle| \psi_j \right\rangle . \qquad \qquad ... 2.19$$

Consider the target Hartree-Fock approximation (THFA) where to a good approximation, ϕ_0 is the target wave function, so for $\alpha \neq 0$, $a_0^{(0)} = 1$ and $a_\alpha^{(0)} \approx 1$. In this case only one characteristic orbital, ψ_i is usually needed, whereas in general a linear combination of these orbitals is used.

The feature of the THFA is that experimentally the momentum profile is usually well described by the target Hartree-Fock orbital, ψ_i. Hence the target Hartree-Fock basis is the optimum choice in the (e,2e) sense. The overlap then becomes;

$$\left\langle q \, f \middle| 0 \right\rangle = t_{j0}^{(f)} \psi_j(q) = t_{i0}^{(f)} \psi_i(q) . \qquad \qquad ... 2.20$$

Then the differential cross section can be expressed in the PWIA as:

$$\frac{d^5\sigma}{d\Omega_s d\Omega_e dE_s} = (2\pi)^4 \frac{k_s k_e}{k_0} f_{ee} S_{io}^{(f)} N_i \left| \left\langle k_s k_e \middle| \psi_i(q) k_0 \right\rangle \right|^2 , \qquad \qquad ... 2.21$$

where $S_{io}^{(f)}$ is the spectroscopic factor,

$$S_{i0}^{(f)} = \left[t_{i0}^{(f)} \right]^2 , \qquad \qquad \ldots 2.22$$

and f_{ee} is the electron-electron collision factor and N_i is the occupation number of the orbital ψ_i. The closure and normalisation relations leads to the spectroscopic sum rule,

$$\sum_f S_i^{(f)} = 1 . \qquad \qquad \ldots 2.23$$

In the PWIA and DWIA the outgoing electron wave functions are treated respectively as plane waves or waves distorted by the ion static potential. Brauner, Briggs and Klar (Brauner *et al.*, 1989) have developed a theory which is capable of solving approximately the three body Coulomb problem in the final state with correct asymptotic boundary conditions. The BBK approximation constructs the wave function, $\Psi^{(+)}$, as a product of the asymptotic forms for each of the three Coulomb two-body systems. This wave function solves the full three body Schrödinger equation (equation 2.8a):

$$\left(\frac{\Delta_R^2}{2\mu} + \frac{\Delta_r^2}{2\nu} + \frac{Z_p}{|r - \alpha R|} + \frac{Z_t}{|r + \beta R|} - \frac{Z_p Z_t}{R} + E_f \right) \Psi_f = 0 \qquad \ldots 2.24$$

where

$$\alpha = \frac{M_T}{M_T + M_P}, \quad \beta = \frac{M_P}{M_T + M_P} \quad \text{and} \quad E_f = \frac{k^2}{2\mu} + \frac{K^2}{2\nu}$$

and the subscripts, T and P represent the target and projectile electron respectively.

The wave function, $\Psi^{(-)}_f$, for the two electron continuum state which considers all three two-body Coulomb interactions is:

$$\Psi^{(-)} = (2\pi)^{-3/2} e^{i k_a \cdot r_a} C(-\alpha_a, k_a, r_a)(2\pi)^{-3/2} e^{i k_b \cdot r_b} C(-\alpha_b, k_b, r_b) C(+\alpha_{ab}, k_{ab}, r_{ab}) \quad \ldots 2.25$$

where the Coulomb factors are:

$$C(\alpha, k, r) = \Gamma(1 - i\alpha) e^{-\pi\alpha/2} {}_1F_1 \left[-i\alpha : -i(kr + k \cdot r) \right] \qquad \ldots 2.26$$

and

$$\alpha_a = \frac{z}{k_a}, \quad \alpha_b = \frac{z}{k_b}, \quad \alpha_{ab} = \frac{1}{2k_{ab}}, \quad \text{with} \quad k_{ab} = \frac{1}{2}(k_a - k_b) \quad \text{and} \quad r_{ab} = r_a - r_b .$$

The BBK approximation has been shown to be in good agreement with experiments having an incident energy above 150eV. Further work has been conducted at an energy of 50eV and these results are encouraging (Brauner *et al.*, 1991).

Section 2.3   **Background Discussion of Polarisation Effects**

A beam of electrons is said to be polarised if it has a preferred spin. The degree of polarisation of an electron beam is defined as:

$$P = \frac{N(\uparrow) - N(\downarrow)}{N(\uparrow) + N(\downarrow)}, \qquad \ldots 2.27$$

where $N(\uparrow)$ is the number of electrons with spin up and $N(\downarrow)$ is the number of electrons with spin down. As there is an array of polarised electron sources available, it is necessary to be able to compare the characteristics of the sources. One such characteristic is the figure of merit, P^2I, where P is the polarisation and I is the electron beam current. Other characteristics such as the ease of reversal of polarisation, brightness and longevity are also important. (Kessler, 1985).

Producing a reliable source of polarised electrons has been researched for some years and a comprehensive review is given in Kessler (1985) which gives the advantages and disadvantages of various polarised electron sources. In the present experiments, the polarised electron source is produced from non-magnetic material. This relies on the spin-orbit interaction which splits the energy bands, in this case, in a GaAs crystal. The energy bands for GaAs are shown in figure 2.2. At the center of the Brillioun zone (the Γ point), the P valence band is split into fourfold degenerate $P_{3/2}$ and twofold degenerate $P_{1/2}$ bands as a result of the spin-orbit interaction. The energy gap between these two bands is 0.34eV. The conduction band, $S_{1/2}$ is separated from the valence band by 1.52eV. If the transitions from the m_j sub-levels are considered then the production of spin polarised electrons can be explained. The selection rules for these sub-levels for circularly polarised light are: $\Delta m_j = +1$ for σ^+ (right hand circularly polarised) and $\Delta m_j = -1$ for σ^- (left hand circularly polarised) light (see figure 2.2).
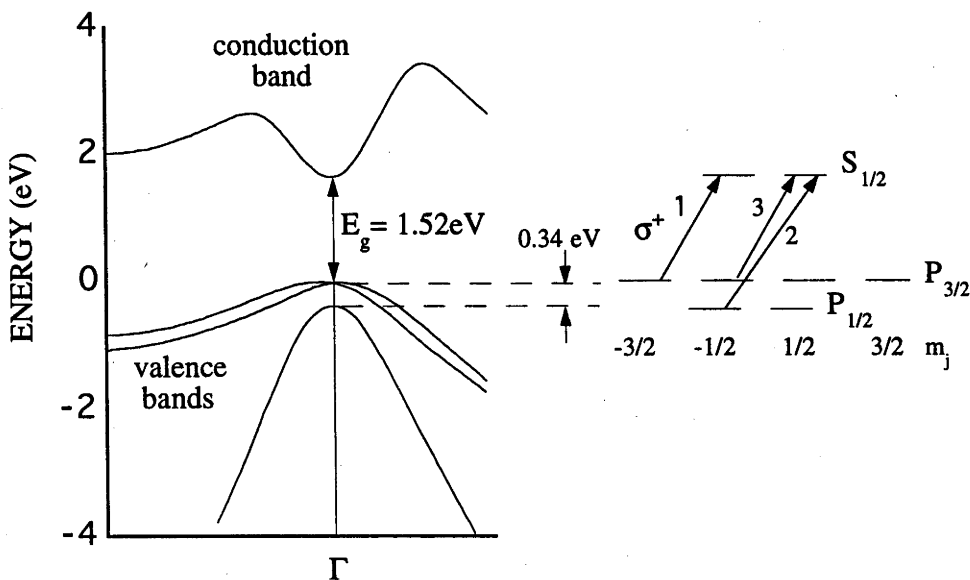

Figure 2.2: The band structure of GaAs, showing on the right side the relative transition probabilities.

The relative transition probabilities for these transitions, shows that for σ^+, three times as many electrons will be in the $m_j = -1/2$ state (spin down) than in the $m_j = +1/2$ state (spin up). That is, it is three times more likely for a transition from the $m_j = 3/2$ than from the $m_j = 1/2$. Similarly for σ^- there will be three times as many electrons in the $m_j = +1/2$ state than in the $m_j = -1/2$ state.

The next stage in generating a beam of polarised electrons from this source is to change the GaAs crystal from a positive electron affinity surface to a negative electron affinity surface to allow for emission of the electrons. Scheer and van Laar (1965) showed that that the vacuum level can be lowered below the bulk conduction band by applying ceasium to the surface forming a dipole layer. Therefore, a negative electron affinity surface can be created by layering ceasium and oxygen onto the surface of the crystal. In this way the electrons which are excited from the valence band to the conduction band by the circularly polarised light can be emitted. The experimental details of this process are given in section 4.2.

By definition of the spin polarisation the theoretical maximum for this source (assuming 100% circularly polarised light and 100% extraction from the source), must be $P = 50\%$. Experimentally the theoretical maximum of the spin polarisation of 50% is never reached. This is due to depolarisation effects, including possible spin exchange scattering in the layers of caesium and oxygen. In general these effects lower the polarisation to levels of about 30%. A new generation of GaAs crystals have been used to produce highly polarised electron beams. It has been shown that it is possible to grow a strained GaAs crystal in which the degeneracy of the valence band is removed (Nakanishi *et al.*, 1991). The splitting of the valence band makes it theoretically possible to achieve 100% polarisation. In practice polarisations as high as 90% have been measured, (Nakanishi *et al.*, 1991 and Maruyama *et al.*, 1992). However, in this experiment a strained crystal was not available.

Section 2.4   Mott Scattering as an Analysis Tool

Mott scattering is a result of the spin-orbit interaction and can be simply described in a classical sense (Gay and Dunning, 1992a). It has proven to be a simple, effective method for determining the polarisation of an electron beam. In most experiments the initial polarisation is a parameter which needs to be well defined.

Consider an electron with high energy being scattered from a nucleus with a charge Ze. Then the motion of an electron with velocity, $\mathbf{v}$, in an electric field, $\mathbf{E}$, of the nucleus, creates a magnetic field, $\mathbf{B}$, in the electron rest frame:

$$\mathbf{B} = -\frac{(\mathbf{v} \times \mathbf{E})}{c},$$

    ... 2.28

where, as usual, c is the velocity of light. Then if $\mathbf{E} = (Ze/r^3)\mathbf{r}$, where $\mathbf{r}$ is the position of the electron relative to the nucleus, the magnetic field becomes:

$$\mathbf{B} = \left(\frac{Ze}{cr^3}\right)\mathbf{r} \times \mathbf{v} = \left(\frac{Ze}{mcr^3}\right)\mathbf{L}, \qquad \ldots 2.29$$

where the electron orbital angular momentum is defined as $\mathbf{L} = m\,\mathbf{r} \times \mathbf{v}$. Then the interaction of this magnetic field with the electron magnetic moment, μ_s, assigns an additional term V_{so}, in the scattering potential. Knowing that the electron magnetic moment is related to the electron spin, $\mathbf{S}$, through

$$\mu_s = -\left(\frac{ge}{2mc}\right)\mathbf{S}, \qquad \ldots 2.30$$

where g is the spin g factor (g ~ 2) and that:

$$V_{so} = -\mu_s \bullet \mathbf{B}, \qquad \ldots 2.31$$

then the spin-orbit contribution to the scattering potential is given by,

$$V_{so} = \frac{Ze^2}{2m^2c^2r^3}\mathbf{L}\bullet\mathbf{S}, \qquad \ldots 2.32$$

where the Thomas precession, a relativistic effect, has been accounted for by including a factor of 1/2. This spin-orbit term then introduces a spin dependence into the scattering cross section which is defined as (*e.g.*, Kessler, 1985)

$$\sigma(\theta) = \sigma_{unpol}(\theta)\left[1 + S(\theta)\mathbf{P}\bullet\mathbf{n}\right]. \qquad \ldots 2.33$$

This is the Mott scattering equation, where $\sigma_{unpol}(\theta)$ is the cross section for spin-averaged scattering, $\mathbf{P}$ is the polarisation of the incident electron beam and $S(\theta)$ is the asymmetry function.
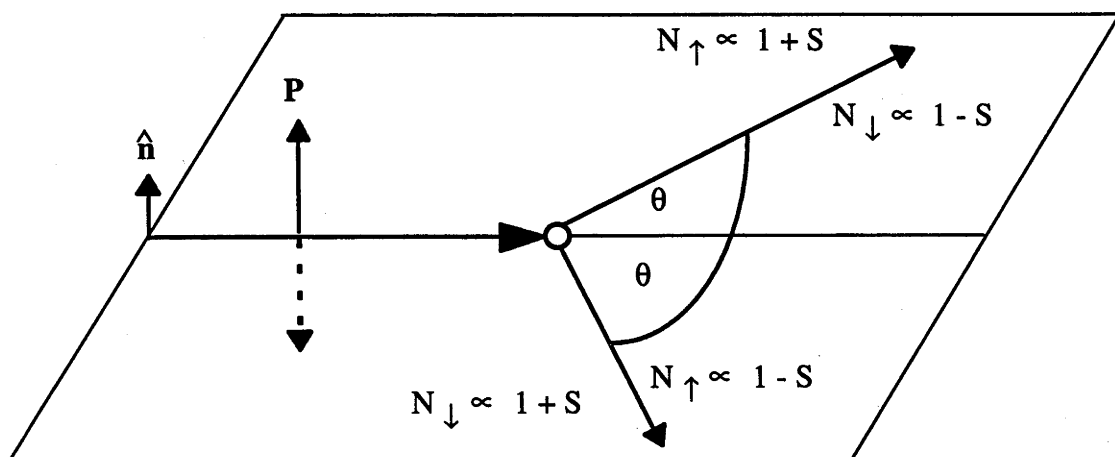
Figure 2.3: Scattering of an unpolarised electron beam.

This scattering process can be seen in figure 2.3. Here the unit vector, $\hat{n}$, is normal to the scattering plane and using **k** and **k'** is defined as:

$$\hat{n} = \frac{k \times k'}{|k \times k'|}. \qquad \ldots 2.34$$

Mott scattering can be described via a double scattering experiment. In such an experiment an initially unpolarised electron beam is scattered from a high Z target (*e.g.*, gold, Z = 79 or thallium, Z = 90). That is, an incident beam of electrons is assumed to have equal numbers of electrons with spin up ($m_s = +1/2$) as with spin down ($m_s = -1/2$). It follows equation 2.33 that the number of spin up and spin down electrons scattered, through angle θ_1, to the left is:

$$N(\uparrow) \propto 1 + S(\theta_1), \qquad \ldots 2.35a$$

$$N(\downarrow) \propto 1 - S(\theta_1). \qquad \ldots 2.35b$$

That means there are different numbers of $N(\uparrow)$ and $N(\downarrow)$ electrons in the beam scattered from a target (T_1) through an angle θ_1, *i.e.*, the scattered beam is polarised. Then the total polarisation for the electrons being scattered through the angle θ_1 to the left is:

$$P(\theta_1) = \frac{N(\uparrow) - N(\downarrow)}{N(\uparrow) + N(\downarrow)} = S(\theta_1). \qquad \ldots 2.36$$

Similarly equations can be written for scattering an unpolarised electron beam to the right through the angle θ_1.
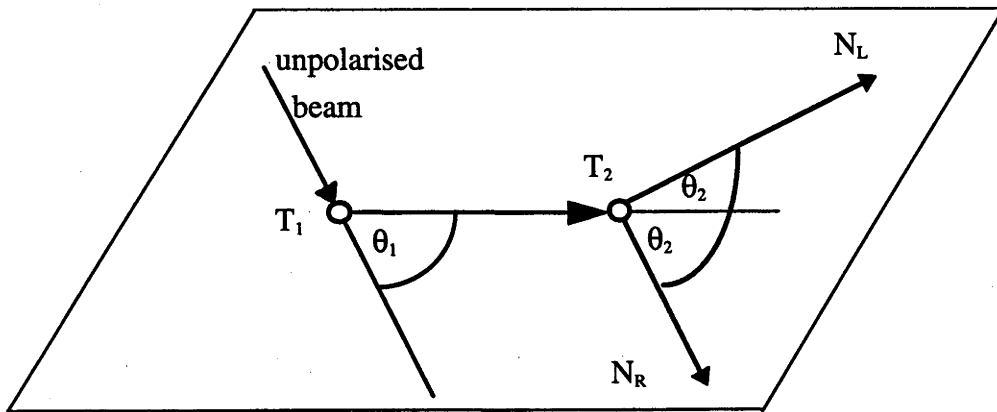
Figure 2.4: A double scattering experiment where T_1 and T_2 are the targets, θ_i are the scattering angles and N represents the number of counts detected either to the left, N_L, or right, N_R, of the incident electron beam.

So far an unpolarised beam of electrons has been scattered from a target and becomes polarised. Now consider the second part of the double scattering experiment. Now the polarised electron beam is scattered from a second target, (T_2) through an

angle θ_2 (see figure 2.4). It follows that scattering a polarised electron beam from a second target yields a left-right scattering asymmetry measurement, $A(\theta_2)$:

$$A(\theta_2) = \frac{N_L - N_R}{N_L + N_R}, \qquad \ldots 2.37$$

where N_L and N_R are the number of electrons scattered to the left and right, through angle, θ_2, respectively. If the scattering events from both targets are coplanar, then:

$$N_L \propto N(\uparrow)(1 + S(\theta_2)) + N(\downarrow)(1 + S(\theta_2))$$
$$\propto 1 + S(\theta_2)P(\theta_1) \qquad \ldots 2.38a$$

and

$$N_R \propto N(\uparrow)(1 - S(\theta_2)) + N(\downarrow)(1 + S(\theta_2))$$
$$\propto 1 - S(\theta_2)P(\theta_1) \qquad \ldots 2.38b$$

Thus, substitution into the equation 2.37 leads to:

$$A(\theta_2) = P(\theta_1)S(\theta_2) = S(\theta_1)S(\theta_2) \qquad \ldots 2.39$$

as equation 2.36 shows that $P(\theta_1) = S(\theta_1)$, where $S(\theta)$ is the analysing power, (or the Sherman function).

The double scattering experiment has shown two features, scattering as a polariser and scattering as an analyser (Kessler, 1985). It is the second feature which shows that the left-right asymmetry, A, observed with the scattering of a beam that is polarised perpendicular to the scattering plane is also determined by $S(\theta)$, *i.e.*, $A = P \, S(\theta)$. This is the principle on which Mott polarimeters operate.

The Sherman function is measured by either a double scattering experiment (figure 2.4), or by using a beam of electrons with known polarisation (equation 2.36). Sherman functions measured with an atomic beam give more accurate results than scattering from thin films, as the latter introduces multiple scattering effects. Furthermore, if a beam of polarised electrons with known spin direction is used, then the sign of the Sherman function can be determined (the sign can also be determined by double scattering of identical atoms).

These Sherman functions are calculated for ideal situations, where scattering is from a single atom. Therefore, it cannot be directly applied to an experiment such as in a Mott polarimeter, where in this case the target is a foil of some thickness, t. The measured Sherman function depends on the thickness of the foil, as well as the scattering angle and the atomic number of the target. Consequently, it is necessary to consider an effective Sherman function which depends on the thickness of the foil. It is best to measure the effective Sherman function for the Mott polarimeter used in a particular experiment, as there are large uncertainties in the theoretical treatment of multiple

scattering (Kessler, 1985). Since the effective Sherman function takes into account multiple scatterings from a foil, it will generally be a lower value than the real Sherman function, which is calculated for a single atom. This calibration of the Mott polarimeter can be done by scattering a beam of electrons of known polarisation from a target, such as a gold foil and measuring the asymmetry. From equation 2.36, the effective Sherman function for that Mott polarimeter can be determined.

An alternate method of calibration is to use a beam of electrons with a known polarisation and to measure the increase in scattering asymmetry for targets of decreasing foil thicknesses, t. Multiple scattering involves reactions with more than one deflection. If the multiple scattering contribution is assumed to be small, then it is possible to extrapolate to a thickness of zero (t = 0), where a thickness of zero represents scattering from a single atom. This can then be normalised to the well established Sherman function for t = 0, (Kessler, 1985). Then this effective Sherman function for the Mott polarimeter employed can be applied to foils of various thicknesses. This is discussed further in section 4.2, where the alternative method used in this experiment is explained.

There are many sources of errors which need to be considered for the measurement of the Sherman function. This includes the multiple scattering from the target which is discussed elsewhere (in section 4.2.2). Other scattering events, such as back scattering from the chamber walls also add to the background noise. This can be negated by coating the walls of the chamber with graphite. If electrons have reached the detectors by indirect means, *i.e.*, from being scattered from the chamber walls, then they would have suffered an energy loss. If a retarding potential Mott analyser is used, these electrons can be discriminated against by use of the energy loss window. This assumes that the resolution of the apparatus is high. Systematic errors also need to be considered especially in an experiment which depends upon asymmetry measurements. This is considered in section 4.2.

Chapter 3

Spin Polarisation Effects

In general the (e,2e) experiment has provided a wealth of information. However, these experiments have usually involved interactions between unpolarised targets and unpolarised projectiles, where the ionisation mechanism is dominated by the strong Coulomb force. Experimental developments in the last few years have made it possible to produce polarised collision partners, thus extending the (e,2e) experiment to provide more information. This additional information involves spin effects, which are generally weaker forces and therefore cannot be observed in ordinary experiments as they are masked by the Coulombic force. To observe these effects it is necessary to use polarised projectiles and/or polarised targets in collision experiments. It is now relatively easy to polarise targets, such as sodium, which have been used in experiments for some years (Baum et al., 1985 and McClelland et al., 1989a).

Of particular interest in this study is the use of spin polarised projectiles. Spin polarised electron sources are implicitly simple devices. Chapter 2 explained theoretically how these devices are possible and chapter 4 demonstrates the practicality of a polarised electron beam. In this work only one example of a polarised electron source is discussed, although a variety exist and a comprehensive review is given in Kessler (1985). Experiments involving polarised electron beams have been used to study concepts such as the spin-orbit interaction, exchange and the fine-structure effect (Hanne, 1992). The following sections describe these spin-dependent effects and how they can be measured.

Section 3.1   Spin-orbit Interaction

The principles of the spin-orbit interaction were discussed in chapter 2 (see section 2.4) in regard to Mott scattering. Recapping briefly, an electron in its rest frame sees a nucleus with velocity, v, and there is an electric field between them, E. A magnetic field due to the moving charged particle is produced, $B = - v \times E/c$. It is this magnetic field which interacts with the magnetic moment of the electron. The corresponding potential describing the scattering process, then has a spin-orbit part, which is proportional to $L \cdot S$ (equation 2.32).

If the incident electron beam is polarised perpendicular to the scattering plane, then the direction of polarisation will not change during the scattering event, although the magnitude may be altered. However, the component of polarisation that is not perpendicular to the scattering plane is subject to a torque caused by the magnetic field and will therefore precess. In this case the direction of polarisation may change. Spin-orbit scattering can clearly be seen, for example, when a beam of unpolarised electrons is elastically scattered from a spinless heavy target and the resulting polarisation is measured.

In the ideal experiment, the polarisation after scattering a polarised beam is (Kessler, 1985):

$$\mathbf{P'} = \frac{\left[P_n + S(\theta)\right]\hat{n} + T(\theta)\mathbf{P_p} + U(\theta)\left[\hat{n} \times \mathbf{P_p}\right]}{1 + P_n\,S(\theta)}, \qquad \ldots 3.1$$

where the directions are indicated in figure 3.1. The initial polarisation has two components, *i.e.*, in the scattering plane, $\mathbf{P_p}$ and perpendicular to the scattering plane, $\mathbf{P_n}$. The definitions of the generalised S, T, U parameters used are:

$$S(\theta) = i\,\frac{fg^* - f^*g}{|f|^2 + |g|^2}$$

$$T(\theta) = \frac{|f|^2 - |g|^2}{|f|^2 + |g|^2} \qquad \ldots 3.2$$

$$U(\theta) = \frac{fg^* + f^*g}{|f|^2 + |g|^2}$$

where f is the direct scattering amplitude, g is the exchange scattering amplitude and S, T, and U represent the Sherman, contraction and rotation functions of the polarisation, respectively. As these parameters are not independent, $S^2 + T^2 + U^2 = 1$.
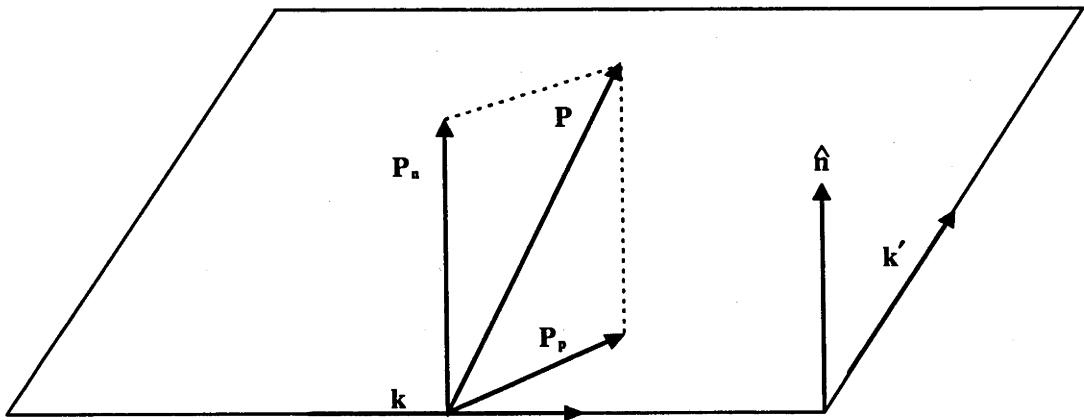

Figure 3.1: A schematic diagram showing the components of the polarisation with respect to the scattering plane, where **k** and **k′** are momenta before and after scattering.

Clearly, if the initial beam is unpolarised, then the resulting polarisation is:

$$\mathbf{P'} = S(\theta)\hat{\mathbf{n}}, \qquad\qquad ...\,3.3$$

where $S(\theta)$ is the Sherman function as discussed in section 2.4. This provides a method for determining the Sherman function and allows measurements of polarised electron beams, via asymmetry functions. The cross section in elastic scattering is dependent on the electron spin (Kessler, 1985):

$$\sigma(\theta,\varphi) = \sigma_u(\theta)\left[1 + S(\theta)\mathbf{P} \cdot \hat{\mathbf{n}}\right]. \qquad\qquad ...\,3.4$$

That is, the spin-orbit effect can give rise to spin polarisation in electron scattering.

Section 3.2   Exchange

An incident electron can be exchanged with the target electron during an electron-atom collision. The scattering amplitude for this exchange process is denoted by g. This event is most obvious when polarised electrons are scattered from a target of light polarised atoms, since the spin-orbit effect is negligible. If a beam of polarised electrons is scattered from a polarised target (say spin down), one possible reaction is:

$$e\uparrow + A\downarrow = e\downarrow + A\uparrow \qquad\qquad ...\,3.5$$

where the incident electron is exchanged with the target electron. This spin-flip is most likely a result of exchange as other spin effects are negligible.

Continuing with this example, presuming the target is spin down, then the other possible reactions are

$$e\uparrow + A\downarrow = e\uparrow + A\downarrow \qquad\qquad ...\,3.6$$

and

$$e\downarrow + A\downarrow = e\downarrow + A\downarrow. \qquad\qquad ...\,3.7$$

Equation 3.6 represents the direct scattering process and is described by the scattering amplitude, f. In these scattering reactions it is possible to distinguish between the direct and exchange scattering processes. The final possibility (equation 3.7) can be due to either direct or exchange scattering. These scattering amplitudes must be added coherently and only the phase difference, γ, is observable.

For completeness, consider a target with spin up, then the following reactions are possible:

$$e\downarrow + A\uparrow = e\uparrow + A\downarrow \qquad\qquad ...\,3.8$$

$$e\downarrow + A\uparrow = e\downarrow + A\uparrow \qquad\qquad ...\,3.9$$

21

$$e\uparrow + A\uparrow = e\uparrow + A\uparrow \qquad\qquad \dots 3.10$$

where equation 3.8 is due to exchange, equation 3.9 is direct scattering and equation 3.10 is either direct or exchange scattering. The scattering amplitudes are g, f, and f-g, respectively. The corresponding cross sections are $|g|^2$, $|f|^2$ and $|f$-$g|^2$. These cross sections would be measurable in an experiment where the spin states of the collision partners were well defined and the spin of the scattered electrons (or the final spin state of the atom) was observed and analysed.

The cross section for scattering a beam of polarised electrons, $(\mathbf{P_e})$ from a polarised target, $(\mathbf{P_a})$, (neglecting all other spin-dependent forces) is (Kessler, 1991):

$$\sigma = \sigma_u(\theta)\left[1 - A(\theta)\mathbf{P_e} \bullet \mathbf{P_a}\right] \qquad\qquad \dots 3.11$$

where $\sigma_u(\theta)$, the cross section for an unpolarised beam is:

$$\sigma_u = \frac{1}{2}|f|^2 + \frac{1}{2}|g|^2 + \frac{1}{2}|f-g|^2 = \frac{1}{4}|f+g|^2 + \frac{3}{4}|f-g|^2 \qquad \dots 3.12$$

with f+g, and f-g, the singlet and triplet amplitudes respectively. Kessler defines the scattering asymmetry as:

$$A(\theta) = \frac{fg^* + f^*g}{2\sigma_u} = \frac{|f||g|\cos(\gamma_1 - \gamma_2)}{\sigma_u} = \frac{|f+g|^2 - |f-g|^2}{|f+g|^2 + 3|f-g|^2}. \qquad \dots 3.13$$

The polarisation of the scattered electrons in a scattering event is:

$$\mathbf{P_e'} = \frac{\left(1 - \dfrac{|f|^2}{\sigma_u}\right)\mathbf{P_a} + \left(1 - \dfrac{|g|^2}{\sigma_u}\right)\mathbf{P_e} - i\dfrac{fg^* - f^*g}{2\sigma_u}\mathbf{P_e} \times \mathbf{P_a}}{1 - A\,\mathbf{P_e}\bullet\mathbf{P_a}}. \qquad \dots 3.14$$

It is obvious that if the target beam is unpolarised ($\mathbf{P_a} = 0$), then the polarisation of the scattered beam is:

$$\mathbf{P_e'} = \left(1 - \frac{|g|^2}{\sigma_u}\right)\mathbf{P_e}. \qquad\qquad \dots 3.15$$

This explains the possible partial depolarisation of the polarised incident electron beam as a result of exchange with the target.

To completely determine the characteristics of the experiment, that is, the scattering amplitudes, f and g, and their relative phase, γ, it is necessary to measure the absolute unpolarised cross section and three observables. The measurement of a

scattering asymmetry, in terms of cross sections for parallel and antiparallel polarisation vectors of the incident electron and the target atom, is defined as:

$$A(\theta) = \frac{\sigma_{\uparrow\downarrow} - \sigma_{\uparrow\uparrow}}{\sigma_{\uparrow\downarrow} + \sigma_{\uparrow\uparrow}} \qquad \ldots 3.16$$

yields $\cos\gamma$, from equation 3.13. If the polarisation of the scattered electrons is measured, then information on the scattering amplitudes may be obtained (equation 3.14). However, more information is needed to completely determine γ. This can be gathered by measuring the electron polarisation component normal to P_e and P_a, then re-arranging equation 3.14:

$$-i\frac{fg^* - f^*g}{2\sigma_u} = \frac{|f||g|\sin(\gamma_1 - \gamma_2)}{\sigma_u} \qquad \ldots 3.17$$

yielding $\sin\gamma$, completely fixing the relative phase. Thus, all characteristics of the experiment are measurable in this manner. As this type of experiment only yields unambiguous information about exchange processes from light atom targets, sodium is well suited to measuring exchange effects.

Section 3.3   Fine-Structure Effect

Reactions cannot simply be classified as either exchange or spin-orbit effects. There are many other factors to consider. Hanne (1983) proposed that if the fine-structure of an atom could be resolved in the final state, then there are significant polarisation effects due to the interplay of exchange and fine-structure splitting. These polarisation effects are evident even in the absence of spin-orbit interaction (*i.e.*, if light atoms are considered).

For the fine-structure effect to be noticeable, it is necessary for the fine-structure states to be resolved in either the initial or the final state. That is, the resolution of the entire experimental apparatus needs to be less than the energy difference separating the fine-structure states being investigated. The fine-structure effect depends on having a non-vanishing orbital angular momentum orientation of the target (*i.e.*, $\langle L \rangle \neq 0$) and electron exchange. If these three conditions are attainable in an experiment in the absence of any other explicit spin dependent forces, then the fine-structure effect is evident (Hanne, 1983).

To explain the fine-structure effect simply, a light atom, such as helium is considered. The physical mechanism can then be easily understood (Kessler, 1991 and McCarthy and Weigold, 1995). The experiment is arranged such that a polarised electron beam excites the 2^3P_j states of helium and only one of the fine-structure states is monitored. It is known that the excitation process may result in an orientation of the orbital angular momentum of the final state (Anderson, Gallagher and Hertel, 1988). In this example experiment this means that an excitation from the ground state, 1^1S_0 to the

2^3P_0 state, leaves the final state with an orbital angular momentum $\langle L_\perp \rangle$, perpendicular to the scattering plane.

Assuming that **LS** coupling holds for the target state and the scattering system, then in the 2^3P_0 state the spin and orbital angular momentum must be antiparallel, as quantum mechanics dictates that $\mathbf{J} = \mathbf{L} + \mathbf{S}$ (this particular excited state has $\mathbf{J} = 0$). That is, $\langle \mathbf{S}_\perp \rangle = - \langle \mathbf{L}_\perp \rangle$. If the orbital angular momentum is assumed to be positive, $\langle \mathbf{L}_\perp \rangle > 0$, then the spin of the final helium state must be negative (spin down). As the Pauli principle must apply, the only possible reaction from ground state (1^1S_0, which has zero spin) to the excited state (2^3P_0), is a result of exchange. Exchange implies that the incident electron is captured and an electron from the atom is ejected. Furthermore, the incident electron must have spin antiparallel to the electron ejected and parallel to the bound electron. Therefore, the probability of exciting the 2^3P_0 with spin up electrons is greater than with spin down electrons. Consequently, the scattering cross sections will be different depending on the orientation of the incident spin direction. An explanatory diagram can be found in *e.g.*, Hanne (1983).

This difference in scattering cross sections results in an asymmetry, A (Hanne, 1983), which is defined as:

$$A = \frac{\sigma(\uparrow) - \sigma(\downarrow)}{\sigma(\uparrow) + \sigma(\downarrow)} = \frac{\langle S_\perp \rangle}{\hbar} = \frac{-\langle L_\perp \rangle}{\hbar} \qquad \ldots 3.18$$

where $\sigma(\uparrow)$ and $\sigma(\downarrow)$ are the cross sections for an incident electron beam with spin $\uparrow$ and spin $\downarrow$, respectively.

However, if the fine-structure of the atom is not resolved, *i.e.*, the multiplet is averaged over, then the asymmetry vanishes. This proves to be a good, simple check for experimental data. Where the energy splitting between the fine-structure states is too small, a 'time reversed' experiment yields similar results. In a 'time reversed' experiment superelastic scattering is measured from a laser excited state as an electron-photon coincidence. This is the case for sodium where experiments have shown that this effect is observable (Hanne, 1983 and McClelland, Kelley and Celotta, 1987).

Section 3.4   **Density Matrix Formalism**

The neatest way to present the theory for polarisation mechanisms is via the density matrix formalism (Bartschat and Madison, 1988 and McCarthy and Weigold, 1995). Guo *et al.* (1995) applied this formalism to describe the asymmetry as produced by the fine-structure effect of a spinless target which includes both spin-orbit and exchange interactions. Here, only the relevant results of the density matrix formalism will be stated. However, the details for the theory can be found in the above references.

In applying this theory the kinematics of the experiment for this work is used. (The kinematics are shown in figure 5.2.) To begin with, the collision parameters need to

be defined in terms of the reduced density matrix in the collision frame. The electron beam is a mixture of pure spin states, with each electron having the same eigenvalues of momentum, k. The spin properties of the electron beam are characterised by the reduced density projector:

$$\rho_{el}^{spin} = \sum_{v_0, v_0'} \left\langle v_0 \left| \rho_{el}^{spin} \right| v_0' \right\rangle \left| v_0 \right\rangle \left\langle v_0' \right| \qquad \dots 3.19$$

where $(\rho_{el})_{v_0, v_0'} = \left\langle v_0 \left| \rho_{el}^{spin} \right| v_0' \right\rangle$ are the reduced density matrix elements. In the $\{ | \pm 1/2 \rangle \}$ representation the explicit form of the reduced density matrix is:

$$\rho_{el} = \frac{1}{2} \begin{pmatrix} 1 + P_3 & P_1 - iP_2 \\ P_1 + iP_2 & 1 - P_3 \end{pmatrix} \qquad \dots 3.20$$

where $(P_1, P_2, P_3) \equiv (P_x, P_y, P_z)$ define the components of the polarisation vector along the x, y, z axes.

Similarly, the atomic beam is described as a mixture of atoms in different pure states:

$$\rho_a = \sum_{\substack{J_0, J_0' \\ M_0, M_0'}} \left| \alpha_0', J_0', M_0' \right\rangle \left\langle \alpha_0, J_0, M_0 \right| (\rho_a)_{M_0 M_0'}^{J_0 J_0'} \qquad \dots 3.21$$

where a pure state of the atom is defined as $| \alpha_0' J_0 M_0 \rangle$ with J_0 and M_0 the total angular momentum of the atom and it's projection, respectively. α_0' is the set of all other quantum numbers required to completely define the atomic state.

The reduced density matrix for the final state can be written as (Guo *et al.*, 1995):

$$\left\langle v_s', v_e'; J_i', M_i' \left| \rho_{el}^{out} \right| v_s, v_e; J_i, M_i \right\rangle =$$

$$\frac{1}{2J_0 + 1} \sum_{\substack{M_0 \\ v_0, v_0'}} f\left(v_s', v_e', M_i', v_0' \right) f^*\left(v_s, v_e, M_i, v_0 \right) (\rho_{el})_{v_0, v_0'} \qquad \dots 3.22$$

where the scattering amplitudes, f (the superscript, *, denotes the complex conjugate) are defined as:

$$f\left(v_s, v_e, M_i, v_0 \right) = \left\langle v_s, v_e, J_i, M_i \left| T \right| J_0, M_0, v_0 \right\rangle. \qquad \dots 3.23$$

As this is a coincidence experiment, where the l•s interaction within the target gives rise to a fine-structure splitting in the ion, the reactions corresponding to the two different values of J_i, are differentiated. The preceding reduced density matrix is then diagonal with respect to J_i. Hence, equation 3.22 becomes:

$$\left\langle v'_s, v'_e, M'_i; v_s, v_e, M_i \right\rangle = \sum_{v_0, v'_0} f\left(v'_s, v'_e, M'_i, v'_0\right) f^*\left(v_s, v_e, M_i, v_0\right)\left(\rho_{el}\right)_{v_0, v'_0} \qquad \dots 3.24$$

where the normalisation coefficient and the summation over M_0 cancel for the case of a closed shell atom.

The (e,2e) differential cross section can be expressed in terms of the density matrix formalism as follows:

$$\frac{d^3\sigma}{d\Omega_s d\Omega_e dE_s} = (2\pi)^4 \frac{k_s k_e}{k_0} \sum_{\substack{M_i \\ v'_0, v_0 \\ v_s, v_e}} f\left(v_s, v_e, M_i, v_0\right) f^*\left(v_s, v_e, M_i, v'_0\right)\left(\rho_{el}\right)_{v'_0, v_0}. \qquad \dots 3.25$$

If the cross section for scattering of an unpolarised electron beam is defined to be:

$$\sigma_{unpol.} \equiv \left(\frac{d^3\sigma}{d\Omega_s d\Omega_e dE_s}\right)_{unpol.}$$

$$= (2\pi)^4 \frac{k_s k_e}{k_0} \sum_{\substack{M_i \\ v_s, v_e}} f\left(v_s, v_e, M_i, v_0\right) f^*\left(v_s, v_e, M_i, v_0\right) \quad , \qquad \dots 3.26$$

then the (e,2e) cross section (equation 3.25) can be written as:

$$\frac{d^3\sigma}{d\Omega_s d\Omega_e dE_s} = \left(\frac{d^3\sigma}{d\Omega_s d\Omega_e dE_s}\right)_{unpol.} \left[1 + P_y \cdot A\right] \quad . \qquad \dots 3.27$$

The parameter of primary interest in this work is the asymmetry, which in terms of the density matrix formalism is:

$$A = \frac{-2(2\pi)^4}{\sigma_{unpol.}} \frac{k_s k_e}{k_0} \left\{ \sum_{M_i} (-1)^{M_i - J_i} \text{Im} \left\{ f\left(\frac{1}{2}, \frac{1}{2}, M_i, \frac{1}{2}\right) f^*\left(-\frac{1}{2}, -\frac{1}{2}, -M_i, \frac{1}{2}\right) \right. \right.$$
$$\left. \left. - f\left(\frac{1}{2}, -\frac{1}{2}, M_i, \frac{1}{2}\right) f^*\left(-\frac{1}{2}, \frac{1}{2}, -M_i, \frac{1}{2}\right) \right\} \right\}. \qquad \dots 3.28$$

If the contribution of the **l•s** interaction is now neglected, the expression for the asymmetry for a pure fine-structure effect in the collision frame is obtained. It is important to note that there are no approximations in this theory as yet. The approximations eventuate in the scattering amplitudes. An intuitive explanation of the experiment for this work is given in chapter 5, where the results are presented in comparison to the calculations of Mazevet (1996) and those of Madison, Kravtsov, Jones and McEachran (1995, 1996). The theoretical calculations used for comparison are briefly discussed in chapter 5.

Chapter 4

Experimental Apparatus

This chapter describes the experimental apparatus used to obtain the results for this work. General descriptions of (e,2e) experiments can be found in Lower and Weigold (1989) and Ehrhardt *et al.* (1986). The particular apparatus used in these experiments has been developed over many years, by several co-workers. Some aspects were described in Zheng *et al.* (1990) and Granitza *et al.* (1993). Some components of the apparatus were changed midway through the course of this work, which coincided with a relocation from Flinders University to the Australian National University. A few of these changes were cosmetic, to comply with the new laboratory environment, while others were more substantial. Phase two of these changes are currently taking place and will also be described here. The majority of the experimental data was collected before phase two began.

There are three main sections of this apparatus, namely the polarised electron source, the Mott polarimeter and the scattering chamber (figure 4.1a and photograph in figure 4.1b). Initial modifications to the system included installing new Helmholtz coils, upgrading the wiring of most sections of the electronics, and most importantly, careful alignment of the entire system. These modifications have been described in detail by Shen (1995) and consequently, are only mentioned here. Phase two is essentially to improve the electron transport from the electron source to the scattering chamber and the differential pumping stage.

The polarised electron source, described in section 4.1, was used to generate a beam of electrons with preferred spin at a given energy. This involved irradiating a GaAs crystal with circularly polarised light of a predetermined wavelength. The electrons were then extracted from the crystal surface and transported through a series of electron optics to the scattering chamber.

To measure the polarisation of the electron beam a Mott polarimeter was used. In this apparatus the electron beam was accelerated to typically 60kV and fired at a gold foil target. By measuring the asymmetry of the outgoing electrons and using the Sherman function the polarisation of the beam can be extracted.

The experiments were performed in the scattering chamber. The scattering chamber houses many pieces of apparatus, including the retarding lens system for the
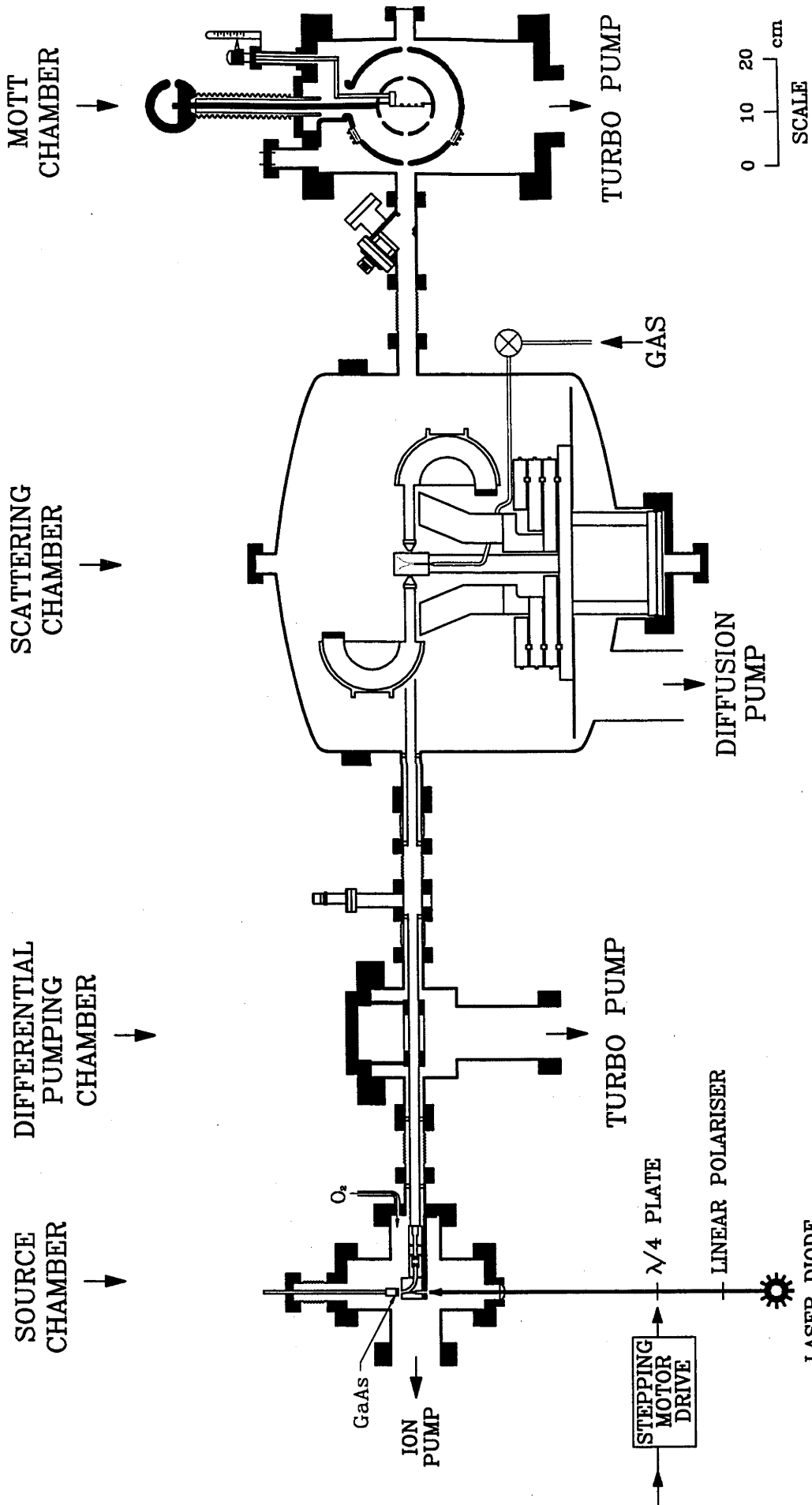
Figure 4.1a: A schematic diagram of the entire apparatus, including the source, differential pumping an scattering chambers and the Mott polarimeter. The polarised electron beam runs from the source chamber to the Mott polarimeter, *i.e.*, left to right.
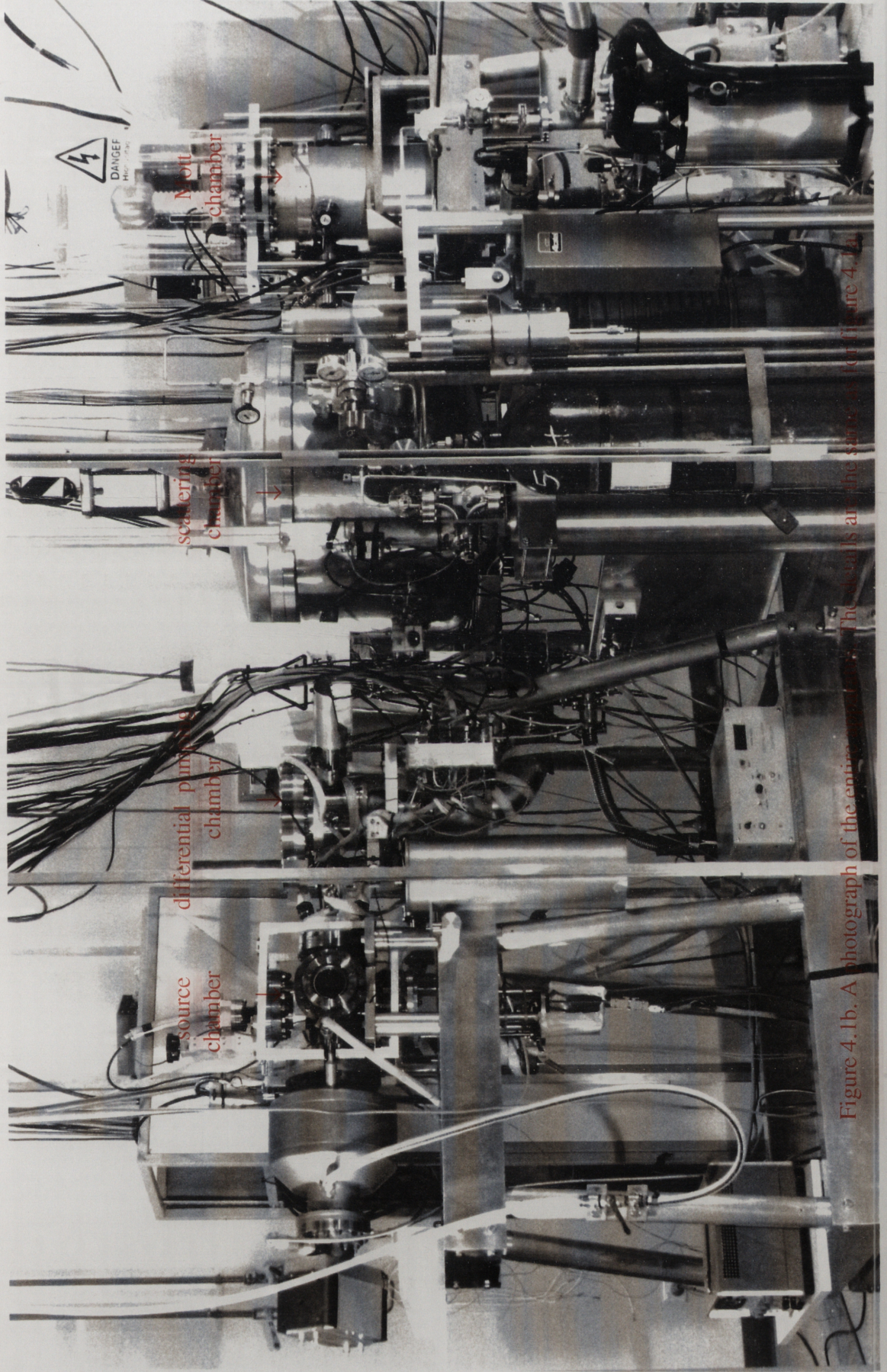
DANGER
High Voltage

Mott
chamber

scattering
chamber

differential pumping
chamber

source
chamber

Figure 4.1b. A photograph of the entire apparatus. The labels are the same as for figure 4.1a.

electron beam, a Faraday cup to measure the beam current, two hemispherical analysers to detect the outgoing electrons in coincidence and a Faraday cage where the interaction takes place. Associated with this scattering chamber was a series of electronic NIM units that were used to process the information gathered and to discriminate against any random coincidence events. This is called the coincidence circuit and is described here and some information can be found elsewhere, for example, in Lower and Weigold (1986).

Section 4.1   Polarised Electron Source

The system was modified to improve the differential pumping and to ensure that both the source and differential pumping chambers could be kept at UHV pressures (phase two of the modifications). Briefly, the original configuration had the source chamber separated by a gate valve from the differential pumping chamber leading to the scattering chamber. The modification entailed placing the gate valve between the differential pumping chamber and the scattering chamber. This modification also included situating an aperture before the differential pumping chamber. At the same time, to improve control over the polarised electron beam the size of the final set of quadrupoles after the extraction optics was increased. The following section gives a detailed description of the polarised electron source as it is today.

4.1.1 Vacuum System

The source region vacuum system was a six-way cross, each arm being 95mm in diameter, constructed of 310 grade stainless steel. The vacuum was sustained by an ion pump and a titanium sublimation pump. The best achievable base pressure was 4×10^{-11} Torr, however a typical pressure was 4×10^{-10} Torr.

A 'differential pumping chamber' separated the source chamber from the scattering chamber so that a good UHV condition could be held in the source chamber. The differential pumping chamber had a height and width of 162mm, was pumped by a 170 l/s turbo pump and a backing pump. The tube for the electron optics, which ran from the beginning of the extraction optics in the source chamber, to the retarding lens system in the scattering chamber, was 18mm in diameter. In the differential pumping chamber the tube was made of mesh to facilitate the general pumping procedure.

The source chamber was baked up to 220°C, while ensuring that the gate valve separating the source and the differential pumping chamber from the scattering chamber was kept below 100°C. The gate valve had a viton O-ring, prohibiting baking at a higher temperature. To enhance the pumping procedure, a bypass tube of 18mm diameter was connected to the source chamber from the turbo pump of the differential pumping chamber. This was utilised in the initial pump down of the source chamber. The bypass tube was shut off after a suitable pressure was reached in the source chamber, when the other pumps where operated. A 4mm aperture on the differential side of the gate valve

ensured there was differential pumping, that is, while the source chamber was at 1×10^{-10} Torr, the differential pumping chamber was at 3×10^{-8} Torr.

4.1.2 Producing Polarised Electrons

This section describes the experimental basics of producing the polarised electrons. To produce the electrons a GaAs crystal, which was carefully selected and handled, was illuminated with circularly polarised light. The polarised electron beam, after extraction from the GaAs crystal surface, was then transported to the scattering chamber to be used in the experiment.

4.1.2.1 The GaAs Crystal

A commercial GaAs crystal with a [100] face was used. Prior to being mounted in the UHV chamber, the crystal was chemically cleaned. The long and involved etching procedures as described by Pierce *et al.* (1980) were not used as it was recognised that the structure of the crystal surface was of greater importance than the chemical treatment of the crystal (Kolac *et al.*, 1988). To this end, the crystal was carefully washed in ammonia, ensuring the shiny side was kept facing upwards. The crystal was then blow dried with nitrogen before being quickly placed in the vacuum chamber. The baking and heating process for the source chamber and the crystal respectively, was then performed to maintain the cleanliness of the system.

The GaAs crystal was mounted to a manipulator which was attached to the top flange of the source chamber. The manipulator allowed for moving the crystal up and down, as well as slight lateral and tilt movements, allowing for further alignment with the laser diode. A commercial heater block was clamped to the crystal to accommodate for uniform heating of the crystal. The block was heated slowly to a maximum of 690°C. Then the temperature was held at this maximum for about five minutes before the crystal was cooled to room temperature. Measurement of the temperature was via a thermocouple which was spot-welded to the heating block. This implies that the thermocouple did not measure the temperature of the crystal directly, however, experience with the activation process has shown that this block temperature was appropriate for correct processing of the crystal. Once the crystal was cleaned and baked it was then lowered into position, 0.8cm above the extraction optics.

4.1.2.2 Laser Diode

A GaAlAs laser diode in CW mode was used as the light source for the production of the polarised electron beam. The laser diode and the associated optics were mounted separately below the source chamber, as per figure 4.2. The wavelength of the laser diode was 780nm. Circularly polarised light was generated by using a linear polariser and a $\lambda/4$ plate, in the usual manner (Pierce *et al.*, 1980). The circular polarisation of the laser diode was measured to be better than 99%. The helicity of the laser diode can be easily reversed by rotating the $\lambda/4$ plate 90°. The $\lambda/4$ plate was carefully calibrated prior to the experiments being performed. This reversal of the

circular polarisation does not move the beam of light, that is, the laser hits the same spot on the crystal for all positions of the $\lambda/4$ plate. The rotation of the $\lambda/4$ plate was controlled by a stepping motor which can either be manually or computer controlled.
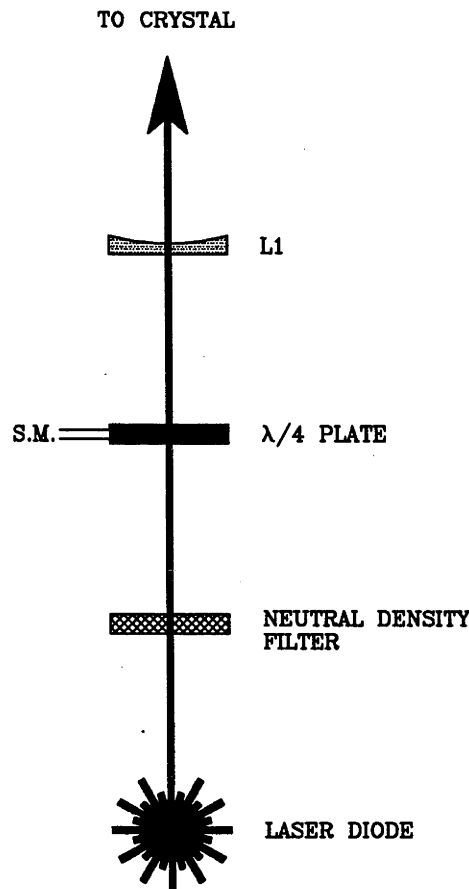
TO CRYSTAL

L1

S.M. $\lambda/4$ PLATE

NEUTRAL DENSITY
FILTER

LASER DIODE

Figure 4.2: The laser diode and associated optics assembly.

4.1.2.3 Activation

After the crystal was cleaned 'in-house' to remove the contaminants from the crystal surface and was cooled to less than 50°C, it was then ready for the next step in the activation process. The crystal surface was then layered with caesium and oxygen, thus creating a negative electron affinity surface (as described in section 2.3). The light impinging upon the crystal emanating from the GaAlAs diode had a power of ~0.8mW.

Caesium was expelled in vapour form from a commercial ampoule (SAES Getters) by applying ohmic heating. Firstly the ampoule must be degassed, which was done with a current of 6 Amps. The current for controlling the caesium was then reduced and the emission current and chamber pressure were monitored. When the emission current rapidly increased, the oxygen layer was required.

Oxygen of high purity was introduced into the chamber via a needle valve from a glass flask which was attached to the source chamber platform. The amount of oxygen in the source chamber was monitored by the chamber pressure. (The pressure in the source

31

chamber was always kept below 5 x 10^{-9} Torr.) As the emission current dropped off, the oxygen was shut off and the caesium vapour was re-emitted. This was the so called 'yo-yo' technique (Tang *et al.*, 1986). The process was completed when no further obvious increase in emission current was gained. The final layer applied to the crystal surface was a layer of caesium.

Typically a maximum emission current of 30-40µA was obtained. The modifications to the source chamber allowed two ampoules to be placed into the source chamber, hence increasing the running time of the source. The wires carrying the heating current were run side by side so as to negate any magnetic field effects.

Once the emission current had been established, it was then passed through the electron optics into the scattering chamber. Initially the emission current was kept at the maximum. This allowed the characteristics of the polarised electron beam from the source to the Faraday cup in the scattering chamber to be investigated. As the beam stabilised and settled, the emission current was decreased so that ~100nA was measured after the interaction region. It was found that the best operating conditions required the caesium dispenser to be kept on 'stand-by' at a current of ~ 2.5A (which was increased as the amount of available caesium decreased).

4.1.2.4 Transport of the Polarised Electron Beam

The experiment which utilised the polarised electron beam was performed in the scattering chamber, 1.2m from the origin of the polarised electrons. It was therefore important to have an efficient method of transporting the polarised electron beam to the scattering chamber. Efficient transportation in this case means maintaining the polarisation of the electron beam, ensuring the beam was parallel and that a high percentage of the beam reaches the interaction region. This was done by a series of lenses and apertures that carry the beam at 1000eV, as shown in figure 4.3.

As stray magnetic fields can affect the trajectory and polarisation of electrons, great care was taken to reduce these fields in the region of the electron beam. It was impossible to maintain a zero magnetic field over the entire path of the electron beam, as well as in the scattering chamber. The electron energies were lowest in the interaction region and would therefore be the most affected by magnetic fields. Hence, the magnetic field was minimised in this region first. This was done by varying the currents in the three sets of Helmholtz Coils (see section 4.3.1). To further reduce the magnetic fields along the 'beam line', µ-metal shielding was used and all internal materials were de-magnetised.

The electrons were extracted from the crystal and accelerated by a uniform field to the anode aperture at 250eV. A photograph of the source chamber and the extraction optics is shown in figure 4.4. Initially the electron beam was polarised longitudinally. To transform this into a transversely polarised electron beam, a 90° electrostatic spherical deflector was used, which does not affect the degree of polarisation. A pass energy of 250eV was chosen for the 90° electrostatic spherical deflector, so as to minimise dispersion and to maximise transmission. The beam then passed through a series of

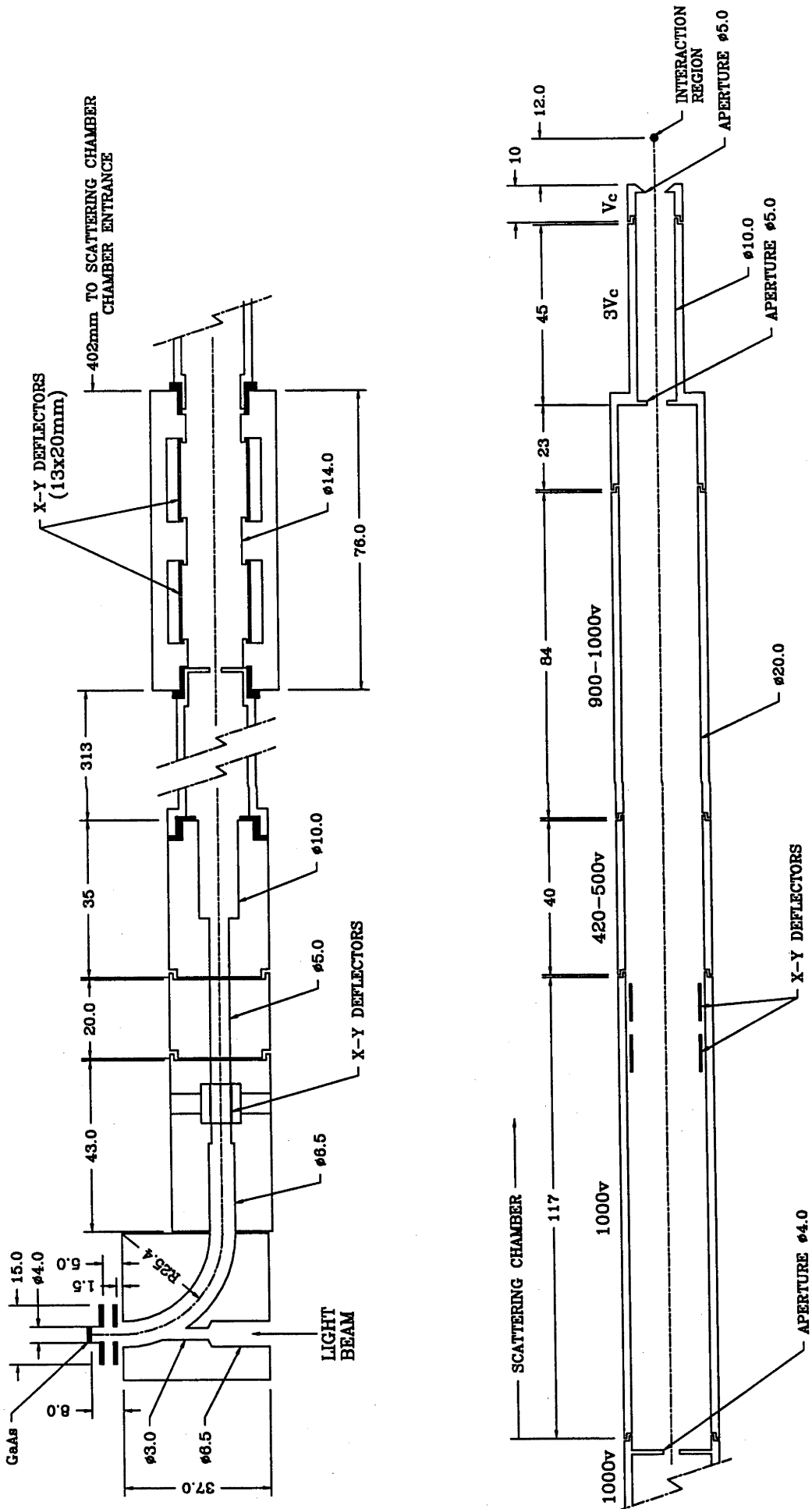Figure 4.3: This diagram shows some of the details of transport tubes which run from the source chamber to the retarding lens system in the scattering chamber.

33

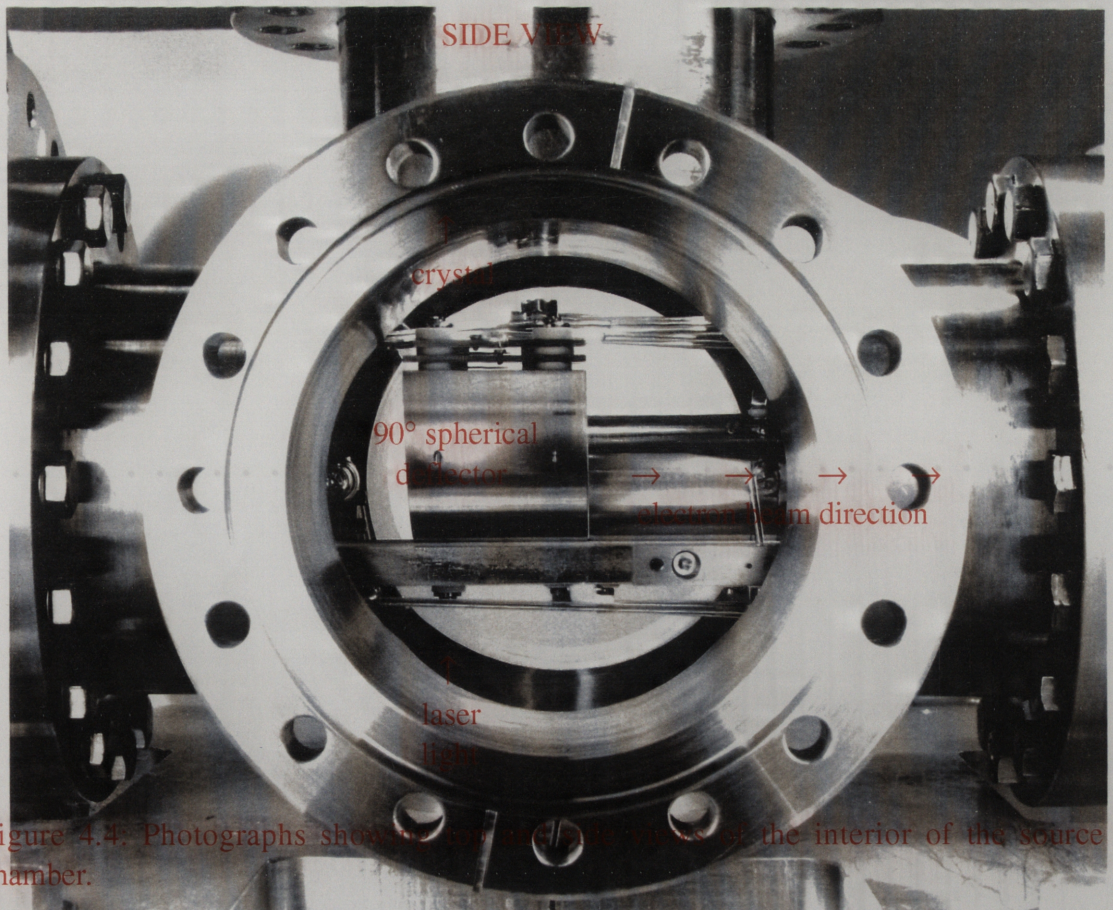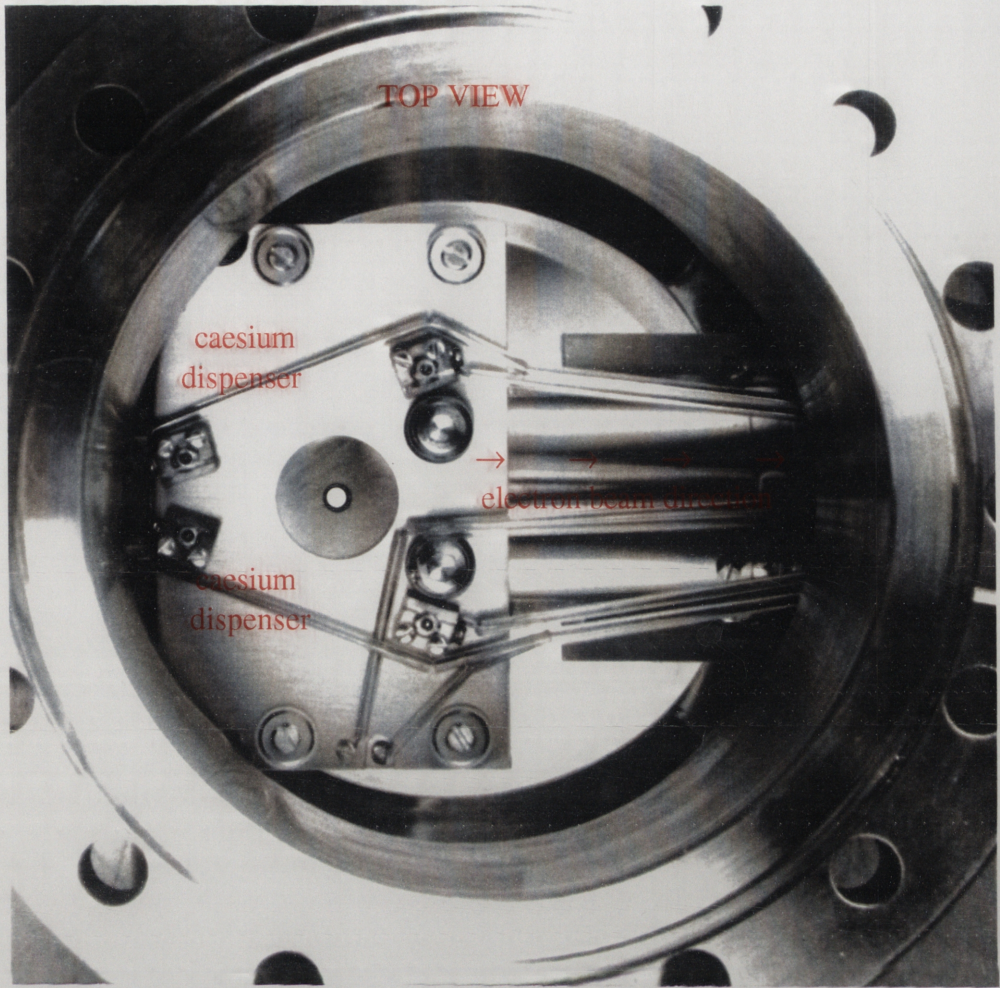TOP VIEW

caesium dispenser

caesium dispenser

electron beam direction

SIDE VIEW

crystal

90° spherical deflector

photon beam direction

laser light

Figure 4.4: Photographs showing a top view and side view of the interior of the source chamber.

lenses at 1000eV. This style of transport system was similar to that used by Pierce *et al.* (1980) and the principles will not be expanded on here, as they have been well described in the reference paper.

Typically, for a cathode voltage of V_c = 147eV, and an emission current of I_{em} = 15.5μA, the total current reaching the Faraday cup was I_{tot} = 5.5μA, with an inner cup measurement of I_{in} = 4.1μA. The transmission of the beam line was typically 30%. This resulted in a current which was satisfactory for the experiment. This beam remained stable for up to a week of continuous operation. The crystal then sometimes required cleaning and re-activation.

Section 4.2   Mott Polarimeter

The Mott polarimeter was used to determine the polarisation of the electron beam using the principles explained in chapter 2. The Mott polarimeter used in this analysis was a compact spherical 'Mini-Mott' polarimeter. It consisted of retarding potential detectors and spherical anodes.

4.2.1 The Apparatus

The Mott polarimeter requires a good UHV system. A suitable vacuum was obtained using a turbo pump, ensuring a base pressure of 1 x 10^{-8} Torr. The Mott polarimeter, which was connected to the scattering chamber, was the last component in the entire system. It could be isolated from the scattering chamber by a manually controlled metal gate value, after determining the polarisation of the electron beam. This allowed for the scattering experiments to be conducted without affecting the vacuum in the Mott chamber. The lid of the Mott polarimeter could be raised hydraulically.

The Mott chamber had two coaxial spherical electrodes mounted in the UHV chamber. The inner sphere had a diameter of 100mm and the outer sphere had a diameter of 200mm. The inner sphere operated at high voltage and was therefore mounted on a high voltage insulator. The voltage was limited by the size of the electrodes and in this case breakdown was at 85kV (the ideal maximum was 100kV). Usual operation was in the 20-60kV range. The outer sphere was held at ground potential providing a relatively safe situation for the operators. Entrance apertures on the inner and outer spheres were 5mm and 10mm respectively.

A manipulator which held three gold foils of different thicknesses and a phosphorous screen was mounted in the centre of the inner sphere via a linear feedthrough. The linear feedthrough was mounted on the top flange and held the foils via an insulating rod. A scale on the exterior of the feedthrough was used to set the foils and the screen in place correctly. The gold foils were commercial products mounted on substrates and were 100nm, 50nm and 10nm thick. For the measurement of the polarisation in these experiments a gold foil of 100nm thickness was used.
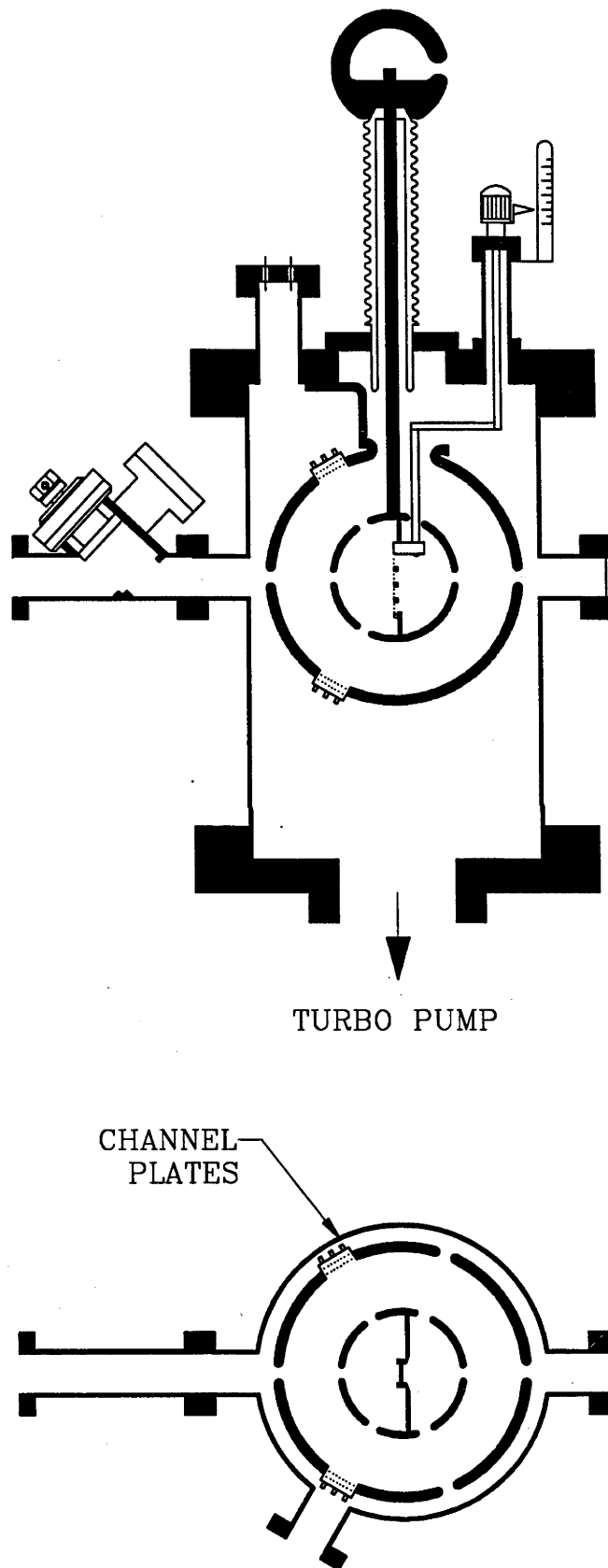
TURBO PUMP

CHANNEL
PLATES

Figure 4.5: The Mott polarimeter, showing the MCPs and the linear feedthrough.

Retarding analysers were used to detect the electrons. These were a combination of retarding meshes and multichannel plates. A grounded entrance mesh shielded the retarding field from the inner and outer spherical electrodes. A retarding mesh, with a voltage V_R, was placed in front of the multichannel plates. This allowed discrimination for electrons that have suffered a certain energy loss during the scattering process. The voltage, V_R was variable and controlled the energy loss window, $\Delta E = E_o - V_R$, where E_o was the incoming electron beam energy. Two pairs of retarding analysers were in the Mott polarimeter. They were located symmetrically at a backward scattering angle of 120° in both the vertical and horizontal planes. A schematic of this apparatus is shown in figure 4.5

4.2.2 Operating the Mott Polarimeter

The electron beam was transported from the polarised electron source through the scattering chamber and into the Mott polarimeter at 1000eV. However, as the normal experimental current was too high for the retarding potential analysers, a neutral density filter was placed between the GaAlAs laser diode and the GaAs crystal, thereby reducing the beam current to acceptable levels. In the Mott polarimeter the spherical electrodes create a symmetrical radial field distribution between the inner and outer spheres. Incident electrons were accelerated to energies between 20 and 60kV towards the inner sphere. The back scattered electrons were decelerated by the ground potential on the outer sphere and were detected if they were within the energy loss window by the retarding analysers. In this analysis the set of retarding analysers in the horizontal plane was used as the electron beam was vertically polarised. In the first instance, the phosphorous screen was positioned in the centre of the inner sphere so that the electron beam was visible. This showed clearly as a bright blue spot and demonstrated that the beam was focused.

4.2.2.1 Calibration

As explained in chapter 2, the effective Sherman function, S_{eff}, is used to determine the polarisation of the incident electron beam. Usually an extrapolation method is used, where the Mott scattering asymmetry is measured for various target thicknesses and extrapolated to a thickness of zero (*i.e.*, scattering from a single atom). This can then be normalised to the well known Sherman function, S, for a given energy and angular setting. However, the maximum of only three measurements of varying thicknesses possible in this case, yields an insufficient data base to use the extrapolation method reliably. Therefore a different extrapolation method was necessary.

The alternate calibration method used in this case was to extrapolate to a zero energy loss (ΔE). In the retarding potential analyser, the degree to which the effective Sherman function, S_{eff}, depended on foil thickness was a function of the size of the inelastic energy window used in detecting the scattered electrons (McClelland *et al.*, 1989b). If the energy loss window was small, then it was presumed that the scattering took place primarily close to the surface. That is, if electrons travel large distances into the foil, then they lose larger amounts of energy. Therefore, the observed scattering events can be limited to the surface region of the foil by reducing the energy loss

window. Hence, reducing the energy loss window effectively reduces the thickness of the scattering region (Gay and Dunning, 1992a). Therefore, by extrapolating the energy loss window to zero, which could then be normalised to the calculation of the Sherman function for a single atom, the polarisation could be determined. It should be noted however, that there may still be multiple scattering events that will contribute to the asymmetry as well as the background. see facing page.

Once it had been established that the beam had reached the manipulator holding the gold foil, the polarimeter was calibrated by performing an extrapolation of scattering asymmetries obtained at 60kV for various energy loss windows to an energy loss of zero. At a zero energy loss the analysing power of the polarimeter can be normalised to the Sherman function for 60kV as reliable theoretical values were available (Ross and Fink, 1988).

4.2.2.2 Calculating the Polarisation

It is well known that Mott scattering from a high Z atom can be used to measure the polarisation of an electron beam, (*e.g.*, Kessler, 1985). The asymmetry, A was a function of the polarisation, P and the Sherman function, S. $A = PS$, where $A = (N_L - N_R) / (N_L + N_R)$. If the effective Sherman function is considered, then from the principles of Mott scattering:

$$N_L = 1 + S_{eff} \quad \text{and} \quad N_R = 1 - S_{eff} \ , \qquad \qquad ...\ 4.1$$

where N is the number of electrons scattered to either the left (N_L) or right (N_R) detector. The measured asymmetry is a combination of Mott scattering asymmetry and instrumental asymmetry (from unequal detector responses). Then if the ratios of these counts is considered:

$$\frac{N_L}{N_R} = \frac{(1 + PS_{eff})}{(1 - PS_{eff})} \delta \ , \qquad \qquad ...\ 4.2$$

where δ is the instrumental response. It is necessary to account for this instrumental response function. This can easily be done if the source of polarised electrons allows a simple, quick reversal of the spin direction, which is the case for a GaAs crystal source.

Then the ratio for the reverse polarisation becomes:

$$\frac{N_L'}{N_R'} = \frac{(1 + PS_{eff})}{(1 - PS_{eff})} \delta \ . \qquad \qquad ...\ 4.3$$

Re-arranging equations 4.2 and 4.3 to eliminate δ:

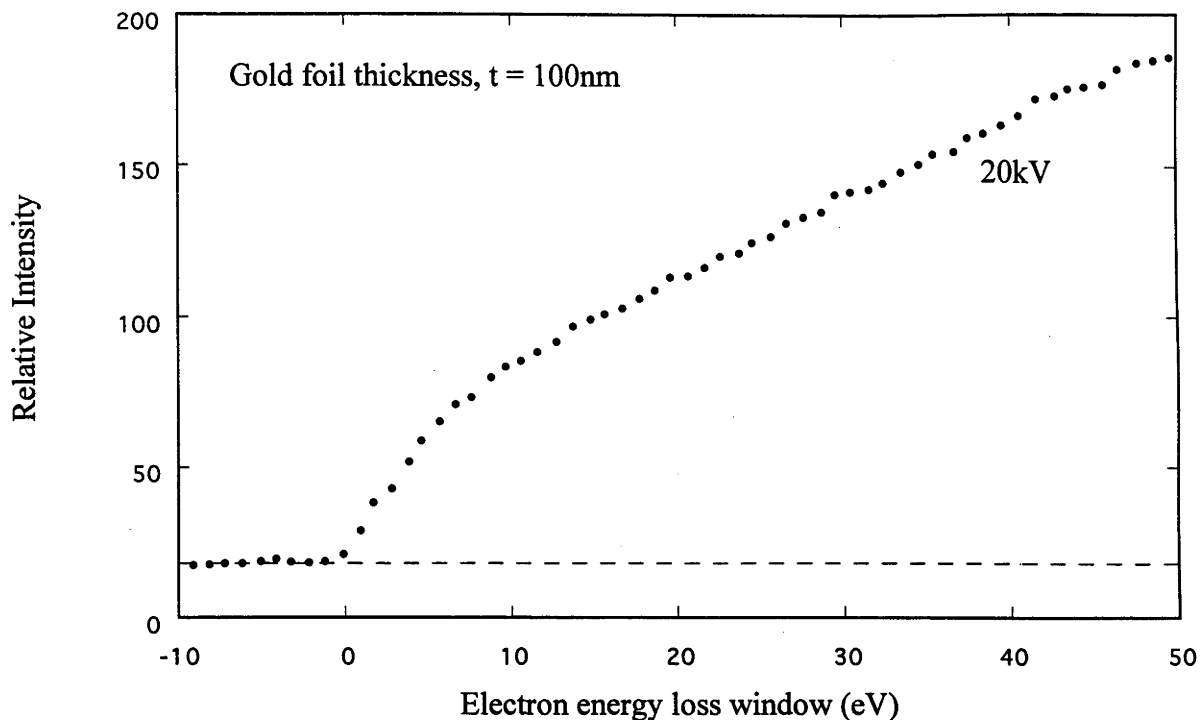$$P = \frac{1}{S_{eff}} \frac{(X - 1)}{(X + 1)} , \qquad \qquad ...\ 4.4$$

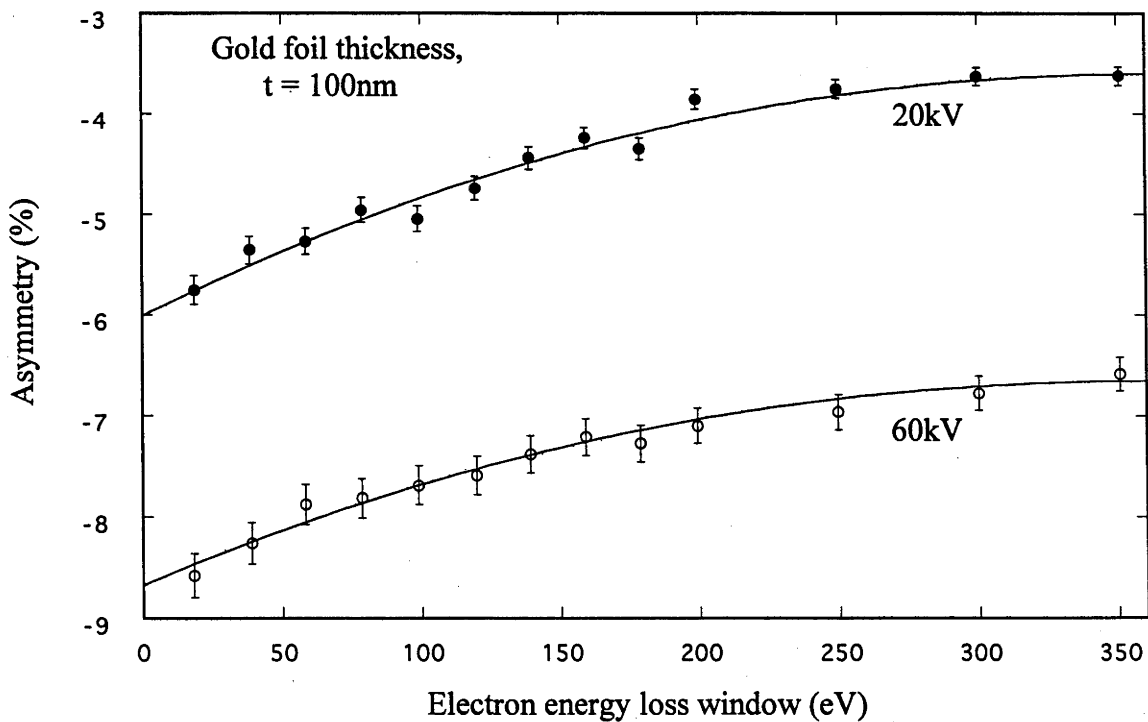Figure 4.6: This graph shows the extrapolation to zero energy loss.

Figure 4.7: The Mott scattering asymmetry as a function of the electron energy loss window.

where X = $(N_L N'_R / N_R N'_L)$. Hence, the polarisation can be measured effectively regardless of the instrumental response function.

4.2.2.3 Measuring the Polarisation

The incident electron beam was accelerated to either 20 or 60kV. An integral electron energy loss spectrum at 20kV is shown in figure 4.6. This was a good spectrum in that it clearly shows the zero energy loss cutoff. The energy resolution is determined by the retarding potential method, which is the width of the steep rise near cutoff in a graph of intensity verses retarding potential. For this device the energy resolution, $\Delta E/E$, was 2.5 x 10^{-4}, which is comparable to similar Mott detectors (Uhrig *et al.*, 1989 and Gay *et al.*, 1992b). This resolution is sufficient to ensure that elastic scattering events can be differentiated from inelastic scattering events.

The asymmetry measurements are shown in figure 4.7 for 20kV and 60kV. Here a least squares fitting procedure is used to fit the data with a quadratic function. The extrapolation to zero yields A = -0.087 ± 0.004 at 60kV. The theoretical value of the Sherman function for 60kV is S = -0.362 (Ross and Fink, 1988). From equation 2.33, the polarisation for the incident electron beam given by P = A/S is 0.24 ± 0.01 (or 24 ± 1%). This measurement took no longer than an hour. Once the calibration and the initial measurement have been completed for 60kV, S_{eff}, is known for all energy loss windows, ΔE, at both 60 and 20kV. Therefore, subsequent measurements of the polarisation under similar experimental conditions could be performed at the lower energy, where the Mott polarimeter operates more effectively.

The error analysis for the measurement warrants further discussion. The previously cited polarisation value of 0.24 ± 0.01 includes only the counting statistics. It would be expected that if the number of measurements were increased that this error would be reduced. However as this error fails to include systematic errors, simply increasing the number of measurements does not significantly decrease the total error. Systematic errors can arise from asymmetric response functions of the detectors, but the main source of these errors is the extrapolation procedure. The unequal detector responses were accounted for as discussed above in the calculation of the asymmetry and the derivation of the polarisation value. A 10% uncertainty was assumed for the extrapolation error and combining this with the statistical error, a more appropriate value for the error is 0.24 ± 0.03.

Section 4.3   Scattering Chamber and Associated Electronics

The following section describes the housing in which the actual experiments were performed. It is divided into two parts, namely a description of the scattering chamber and secondly, the electronics required to accumulate and process the data.

4.3.1 Vacuum System

The scattering chamber was a cylinder, 74cm in diameter and 73cm high. It was pumped by a diffusion stack which was pumped by a rotary backing pump. The base pressure in this chamber was typically 6×10^{-8} Torr, but was generally operated at 6×10^{-6} Torr when using a gaseous target. A photograph of the inside of the scattering chamber is shown in figure 4.8. The laboratory where this experiment was conducted had a residual magnetic field of 1.1Gauss which was compensated for by using sets of orthogonal "Helmholtz" coils. Three sets were necessary with the dominant set being in the vertical direction. The vertical coils were octagonal and had an internal diameter of 6m, with 100 turns and a current of approximately 3Amps. The north-south and east-west coils were less substantial, square in shape with sides of 1m length, having 20 turns with a current of approximately 1 Amp. To assist the coils the scattering chamber was lined with μ-metal shielding. The resultant magnetic field was less than 5mG in the vicinity of the interaction region.

4.3.2 Electron Detection System

The electrons pass through a cylindrical electrostatic lens system into the hemispherical analyser and impinge upon a detection unit. This detection unit was the combination of multichannel plates and a resistive anode. From the position that the electron arrives at the resistive anode the energy information of the electron can be deduced. The analysers were mounted on rotatable turntables allowing external positioning with respect to the electron beam. The following subsections describe these units.

4.3.2.1. Interaction Region

The interaction region was defined by the overlap of the incident electron beam and the target gas beam. This region was enclosed in a Faraday cage to minimise electric field interference. The Faraday cage was a solid tube made of stainless steel, with viewing slits to allow the analysers access to the interaction region so that the electrons may be detected. The top of the cage was constructed of mesh for pumping efficiency.

A Faraday cup measured the beam current behind the interaction region. The cup was designed to be lifted out of the line of sight of the beam by an external control, so that the electron beam could pass through to the Mott polarimeter. This also allowed the analysers to operate at small forward angles. To have an indication of the focusing of the electron beam the Faraday cup consisted of two cups, an inner and outer cup with diameters of 3mm and 6mm respectively. Typical measurements in the inner cup were about 110nA with about 25nA measured in the outer cup, under normal experimental conditions.
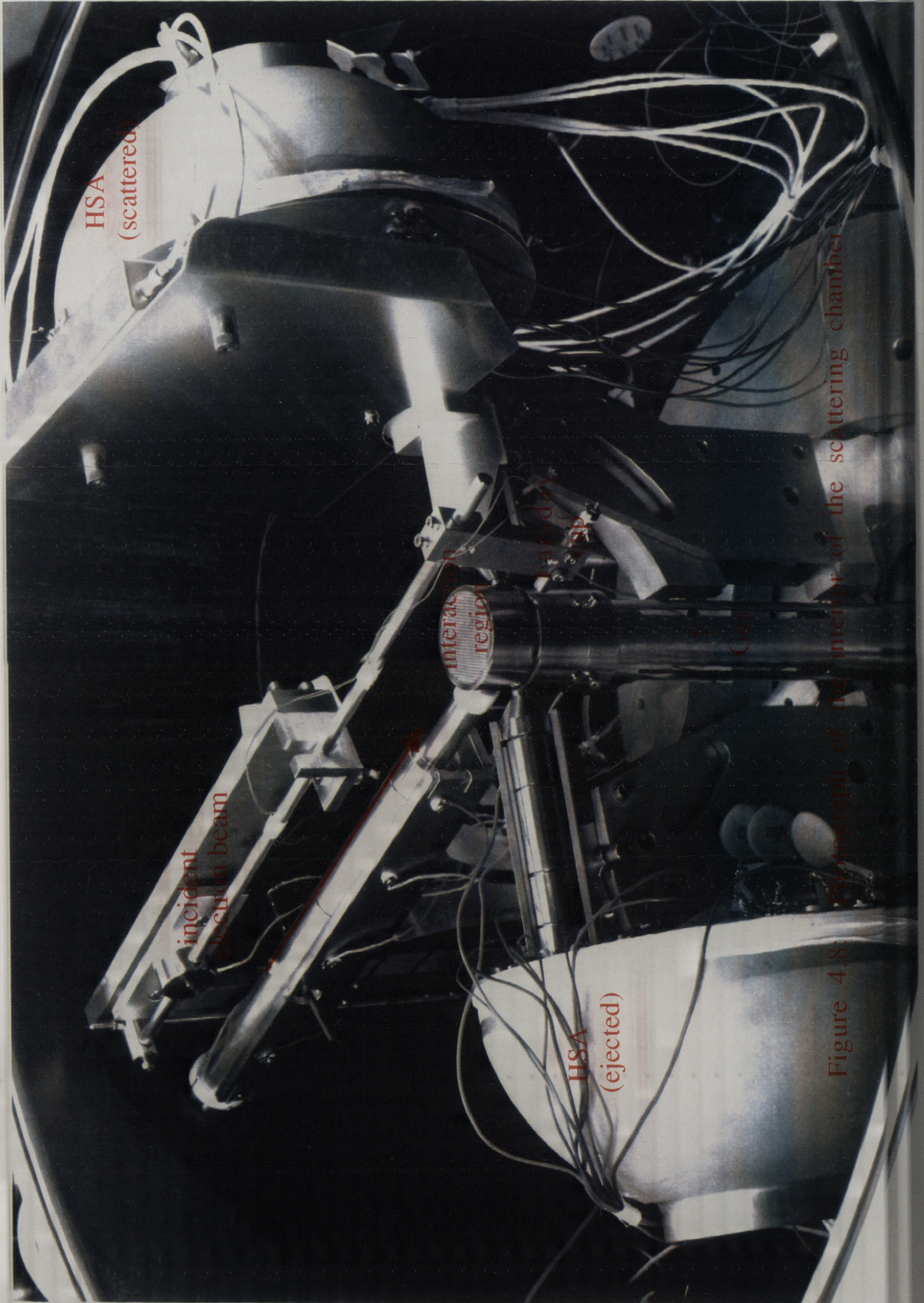
Figure 4.8: Photograph of the interior of the scattering chamber.

HSA (scattered)

interaction region

incident electron beam

HSA (ejected)

4.3.2.2 Hemispherical Analysers

Two hemispherical electrostatic analysers were used for the energy and momentum analysis of the outgoing electrons. Hemispherical electrostatic analysers have been used in many experiments and are based on the design of Kuyatt and Simpson (1967). This type of analyser detects in one dimension and is suitable for an (e,2e) experiment. This is due to its point to point focusing properties and its almost linear dispersion of energy with respect to the particle position at the exit plane. The analyser consists of two parts, an electrostatic lens system and a 180° hemispherical analyser. A schematic of the lens system and the analyser is shown in figure 4.9.
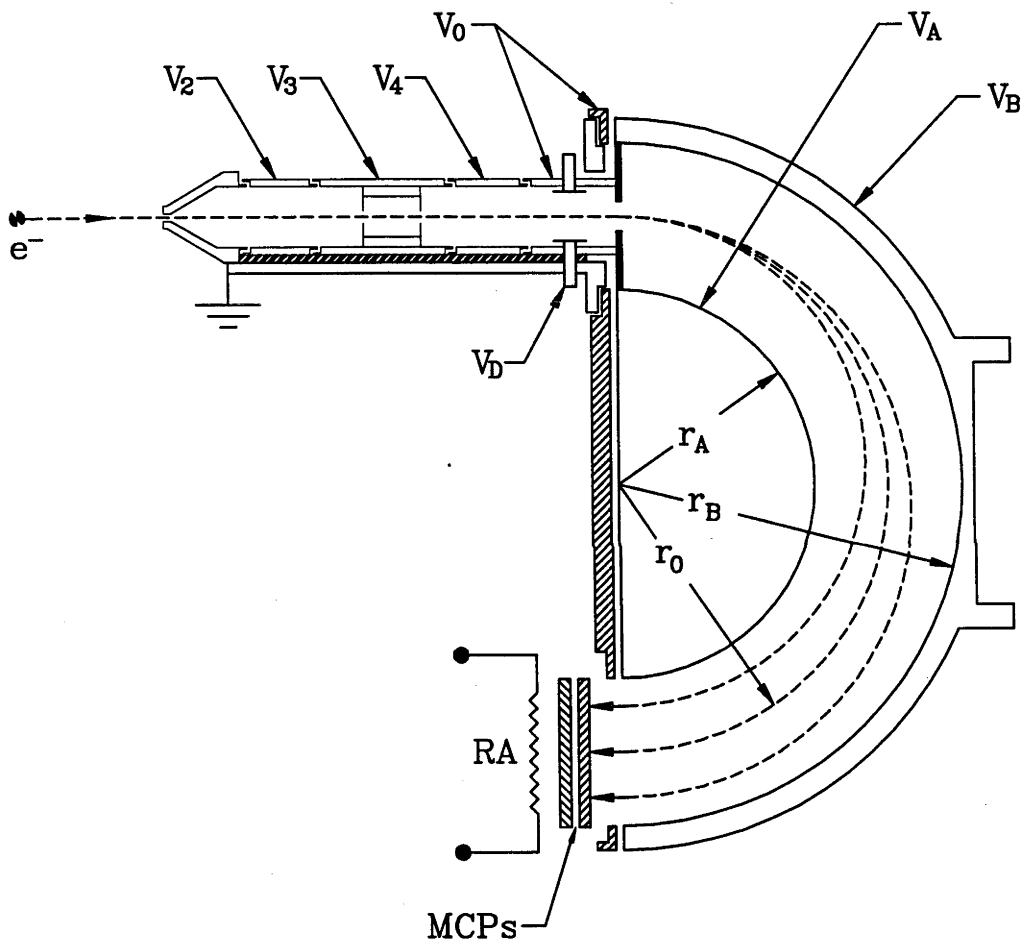

Figure 4.9: Cross section of the electron lens system and 180° hemispherical analyser.

The feature of the five-element lens system is that it can independently vary the angular and energy resolution. The first of the five elements, which is closest to the interaction region, must be grounded and has an entrance aperture of 2mm. The two zoom lenses are formed by elements one, two and three and three, four and five with voltages of ground, V_2, V_3 and V_3, V_4 and V_0 respectively. The first zoom lens controls the angular resolution, while the second controls the energy resolution. The electron beam is collimated by two 1.5mm slits in the third element and hence determined the acceptance angle of the analysers. V_0 on the last (fifth) element determined the electron mean pass energy, E_p of the hemisphere. A quad X-Y deflector set, with voltage V_D, symmetric about V_0, was incorporated in the final lens element in front of a 5mm circular aperture, which is the lens system exit and analyser entrance.

The hemispheres of the analysers are concentric, with an inner diameter of $r_A =$ 51mm and an outer diameter of $r_B =$ 89mm. Six stainless steel rings were inserted between the two hemispheres in order to produce a uniform potential distribution so that the energy resolution of the analyser could be improved. The central energy for the electrons entering the 180° hemispherical analyser is E_p. The analyser functions as an energy dispersing device by detecting electron with energies of $E_p \pm \Delta E/2$. The energy dispersing range, ΔE, is defined at the exit of the analyser by a slit which is 25mm long and 5mm wide. In this case ΔE is 6eV.

4.3.2.3 Position Sensitive Detectors

Position sensitive detectors were placed at the exit of each of the hemispherical analysers to determine the spatial co-ordinates of detected electrons. Position sensitive detectors consisted of multichannel plates (MCPs) and a resistive anode (RA) as shown in figure 4.10. This arrangement allowed for information to be simultaneously collected over the range of the MCPs. By using this arrangement the quality of the data was improved, as more data can be collated in a shorter time frame (Zheng, 1989). This was important as (e,2e) coincidence countrates were generally low.
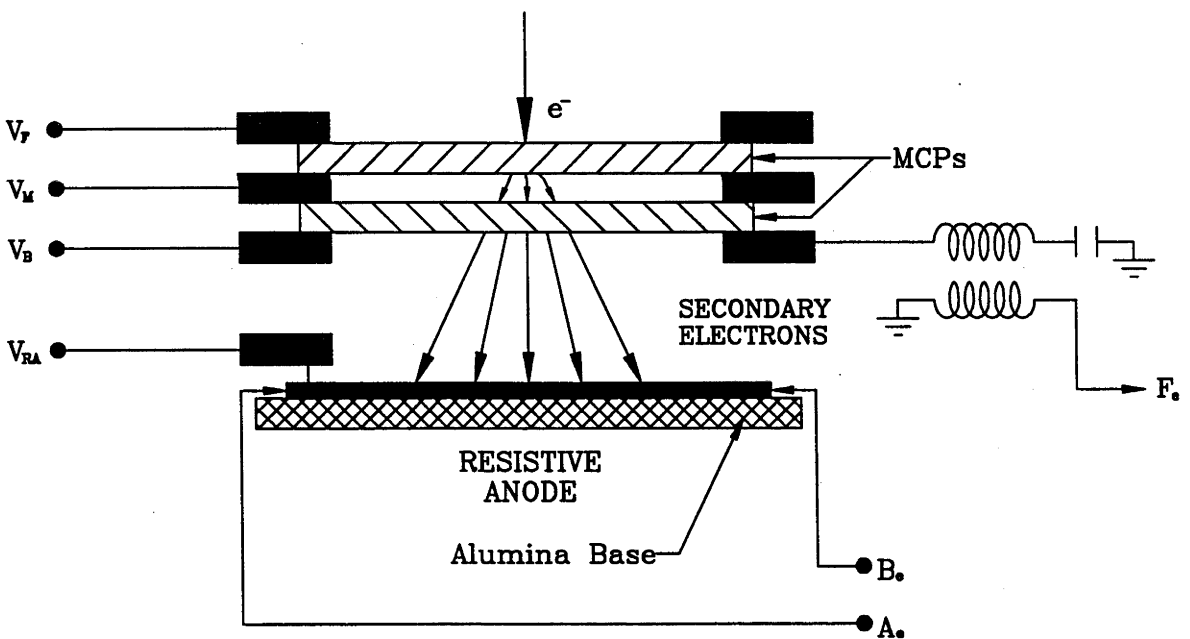
Figure 4.10: The MCPs and resistive anode arrangement, which shows the fast, timing pulse, F_e, and the slow pulses, A_e and B_e.

The MCPs and RAs were from Surface Science Laboratory and were secured in a specially designed mount. The MCPs were arranged in a chevron configuration that provided the necessarily high gain (10^6- 10^7) for detecting single electrons and reduced spurious signals from ion-feedback. An incident electron hitting the front MCP produced an electron cascade, resulting in an electron cloud that leaves the MCPs and impinged on the resistive anode.

In this experiment a Gear type resistive anode was used, as it was important for the detector to have a good linear response function. The spatial information required was derived from the 'charge division' method. The charge cloud impinging upon the RA produced two pulses from either end of the RA. These two pulses were fed into the electronic circuit and the positional information was deduced. The way in which this was done is described in detail in the following section.

Associated Electronics

4.3.3 Coincidence Circuit

The electronic circuitry used to process the electronic pulses and that which stored this data has been described many times before. However, as this process was pivotal to the experimental procedure a description is warranted. There are essentially two branches of the coincidence electronics, the energy, or information branch and the timing branch. Simply, the energy branch contained the energy and angular information which was the essence of the experiment, while the timing branch ensured a coincident event had taken place and also accounted for accidental coincidences. The complete coincidence circuit is shown in figure 4.11.

4.3.3.1 Timing Branch

The detection of each electron generated three pulses, the origin of these pulses can be seen from the diagram of the position sensitive detectors (figure 4.9). The fast pick off pulse from the back of the second plate of the MCP was the timing pulse, F_e (also referred to as the fast pulse). This denoted the arrival time of an electron at the detector.

A fast inverting pulse transformer was used to decouple the high voltage circuitry and to couple the back plate of the MCP to the fast amplifier. The pulses from the preamplifiers were further amplified by a fast amplifier. The fast timing pulses from the fast amplifiers enter constant fraction discriminators (CFDs), which set threshold levels to remove noise from the signal lines and produce an output correlated in time to the input signal. The discriminator output from one detector was used to start a time-to-amplitude converter (TAC) and the delayed pulse from the other detector provided the stop pulse. The pulse height distribution of the TAC output was proportional to the time difference between the start and the stop pulses. The TAC outputs were either due to real coincidence events or from random coincident events. The pulse height distribution from the TAC therefore has a uniform background caused by the arrival of uncorrelated electrons in the detectors with a peak superimposed on this background due to real coincidence events. This peak was the coincidence peak.

The timing signal needed to be corrected for the variations of the flight times through the analysers. The flight time for an electron passing through a hemispherical analyser increased with increasing entrance energy. Explicitly, an electron having a high energy has a greater radius and therefore a longer pass flight through the analyser.
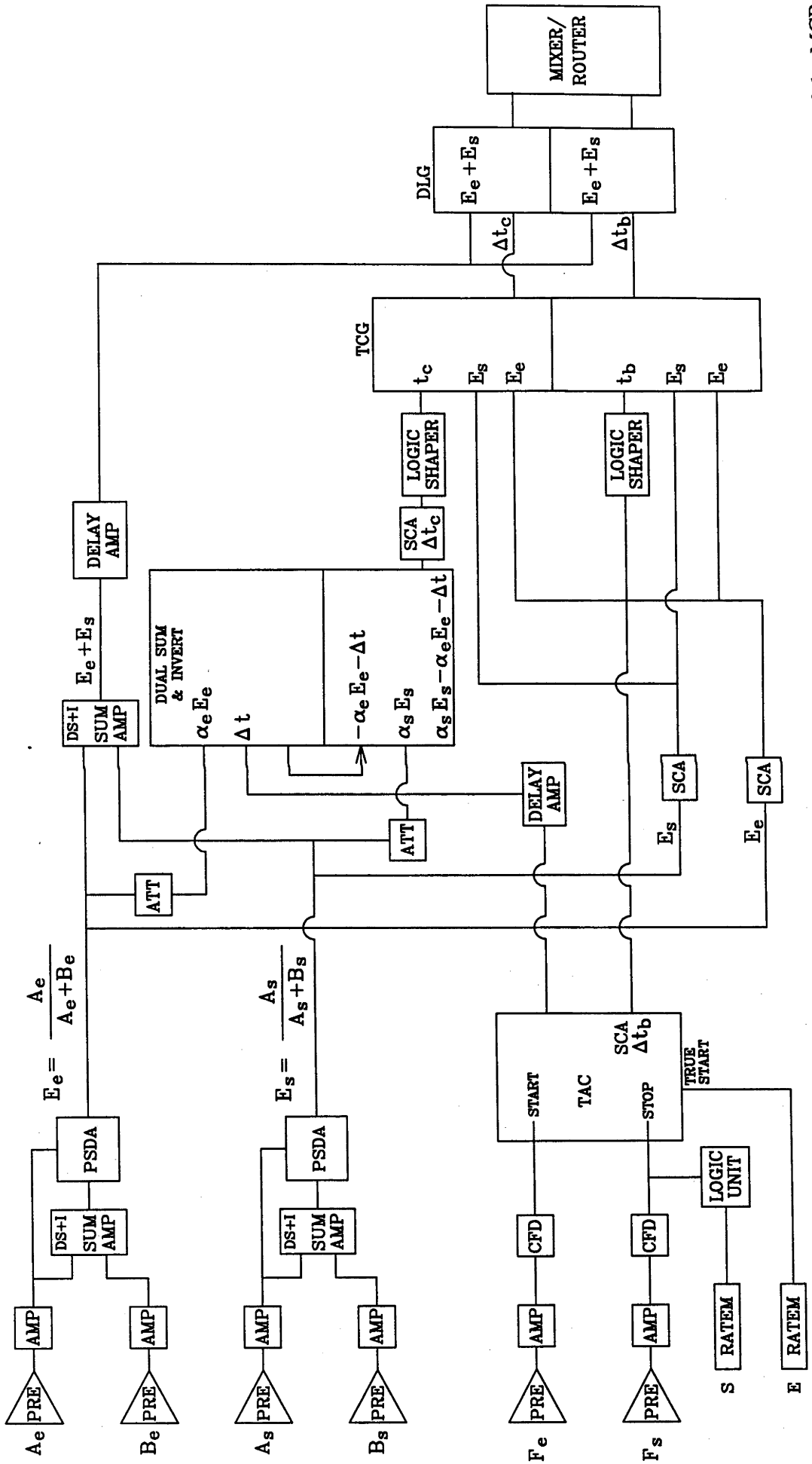
Figure 4.11: The coincidence circuit which shows both the timing and energy branches. The incoming pulses are from the back of the MCPs (see figure 4.10) and the final information is stored in the computer which controls the experiment. See text for more details.

Similarly an electron with low energy has a shorter pass flight (Lower and Weigold, 1989).

If the flight time for the electrons through both analysers was T, (T_s for the scattered electrons and T_e for the ejected electrons), then:

$$T_e = T_e^0 + t_e(E_e),$$ ... 4.5a

$$T_s = T_s^0 + t_s(E_s),$$ ... 4.5b

where T_e^0 is the time for an electron with mean pass energy E_0, to pass through the analyser and

$$t_e(E_e) = t_e(E_e - E_0),$$ ... 4.6a

$$t_s(E_s) = t_s(E_s - E_0).$$ ... 4.6b

The pulse from the TAC, Δt, is given by

$$\Delta t = T_e + T_d - T_s,$$ ... 4.7

where T_d is the delay time in the TAC, T_e is the start pulse and T_s is the stop pulse (ignoring the small time differences through the entrance lenses). Then substituting equations 4.5 into equation 4.7 gives;

$$\Delta t = (T_e^0 - T_s^0 + T_d) + t_e(E_e) - t_s(E_s),$$ ... 4.8

$$\Delta t = T_c + t_e(E_e) - t_s(E_s),$$ ... 4.9

where T_c is a constant. Assuming the analysers are linear with respect to energy, then:

$$t_e = \alpha_e(E_e - E_e^0),$$ ... 4.10a

$$t_s = \alpha_s(E_s - E_s^0),$$ ... 4.10b

For $E_0 = E_s^0 = E_e^0$ and since the analysers are identical, *i.e.*, $\alpha_s = \alpha_e = \alpha$, substituting equations 4.10 into equation 4.9 gives

$$\Delta t = T_c + (\alpha E_e - \alpha E_0) - (\alpha E_s - \alpha E_0),$$ ... 4.11

and rearranging becomes,

$$T_c = \Delta t - \alpha E_e + \alpha E_s.$$ ... 4.12

Hence, the timing spectrum may be corrected in the following manner; the two energy pulses E_e, E_s were attenuated by a factor of α and combined with the pulse from the TAC in a dual sum and invert amplifier, yielding a corrected timing spectrum. A typical timing spectrum is shown in figure 4.12. The angular divergence of the electrons in the hemispherical analyser cannot be corrected for therefore, the timing spectrum has a finite width.

A single channel analyser (SCA) then selected the coincidence signal from the corrected output from the TAC. The background timing window was selected directly from the TAC output (see figure 4.11). Here the timing branch met with the energy branch.

4.3.3.2 Coincidence Calculations

The coincidence peak was collected in a window Δt_c, which was experimentally set and the random background events were collected in a set window Δt_b. True coincidence counts N_t, accumulated in time T can be derived:

$$N_t = N_c - \frac{N_b}{R} \, , \qquad \qquad \dots 4.13$$

where N_c, N_b are respectively the number of counts in the windows Δt_c, Δt_b, and R is the ratio of the window widths, ($R = \Delta t_b / \Delta t_c$).

The standard deviation of N_t is:

$$\Delta N_t = \left[N_c + N_a \left(1 + \frac{1}{R} \right) \right]^{1/2} \, , \qquad \qquad \dots 4.14$$

where $N_a = N_b/R$ is the number of accidental counts in the coincidence window. If R is known accurately then it can be seen that the larger R, the smaller is the error in determining the number of coincidence counts. The number of true and accidental counts can be expressed as:

$$N_t = C_1 n I T \, , \qquad \qquad \dots 4.15$$

$$N_a = C_2 \Delta t_c (nI)^2 T \, , \qquad \qquad \dots 4.16$$

where T is the time for the measurement, n the target gas density, I the incident electron beam current and C_1 and C_2 are constants fully determined by the physics of the process and the overall efficiency of the instrumental arrangement.

Then the signal to background ratio is:

$$r = \frac{N_t}{N_a} = \frac{C_1}{(C_2 n I \Delta t_c)} \, . \qquad \qquad \dots 4.17$$

The quality of the experiment is determined by the relative statistical uncertainty δ, of the true counts:

$$\delta = \frac{\Delta N_t}{N_t} = \frac{1}{C_1}\left[\frac{1}{T}\left(\frac{C_1}{nI} + C_2\left(1 + 1/R\right)\Delta t_c\right)\right]^{1/2}. \qquad \ldots 4.18$$

Therefore a small Δt_c and large R improve the quality of the experiment, as does a long accumulation time T. Obviously increasing nI also improves the experiment, but it reduces the signal to background ratio. Compromising between the accumulation time and the signal to background ratio is important. From equation 4.18 the time T required for a statistical accuracy of δ is:

$$T = \frac{1}{\delta^2}\left[\frac{1}{C_1 nI} + \frac{C_2}{C_1^2}\left(1 + 1/R\right)\Delta t_c\right]. \qquad \ldots 4.19$$

Alternatively the time T required for a statistical accuracy of δ as a function of the true count rate is:

$$T = \frac{1}{\delta^2 N_t}\left[1 + \frac{\left(1 + 1/R\right)}{r}\right]. \qquad \ldots 4.20$$

If the limits for signal to background ratios are considered then there are two cases, for large r (r >> 1+1/R) and for small r (r << 1+1/R).

For r >> 1+1/R

$$T = \frac{1}{\delta^2 C_1 nI}. \qquad \ldots 4.21$$

Here if nI is increased then T can be decreased, but this leads to a smaller signal to background ratio.

For r << 1+1/R

$$T = \frac{C_2 I}{C_1^2 \delta^2}\left(1 + 1/R\right)\Delta t_c. \qquad \ldots 4.22$$

In this case further increases in nI yield no additional reduction in accumulation time (McCarthy and Weigold, 1991b). The experimental apparatus for these experiments was optimised to measure coincidence events with minimum accumulation time and a satisfactory signal to background ratio.

4.3.3.3 Energy Branch

Four slow pulses were generated by the two sets of MCPs, each pair of pulses containing the required position and hence energy information. Each pair of slow pulses
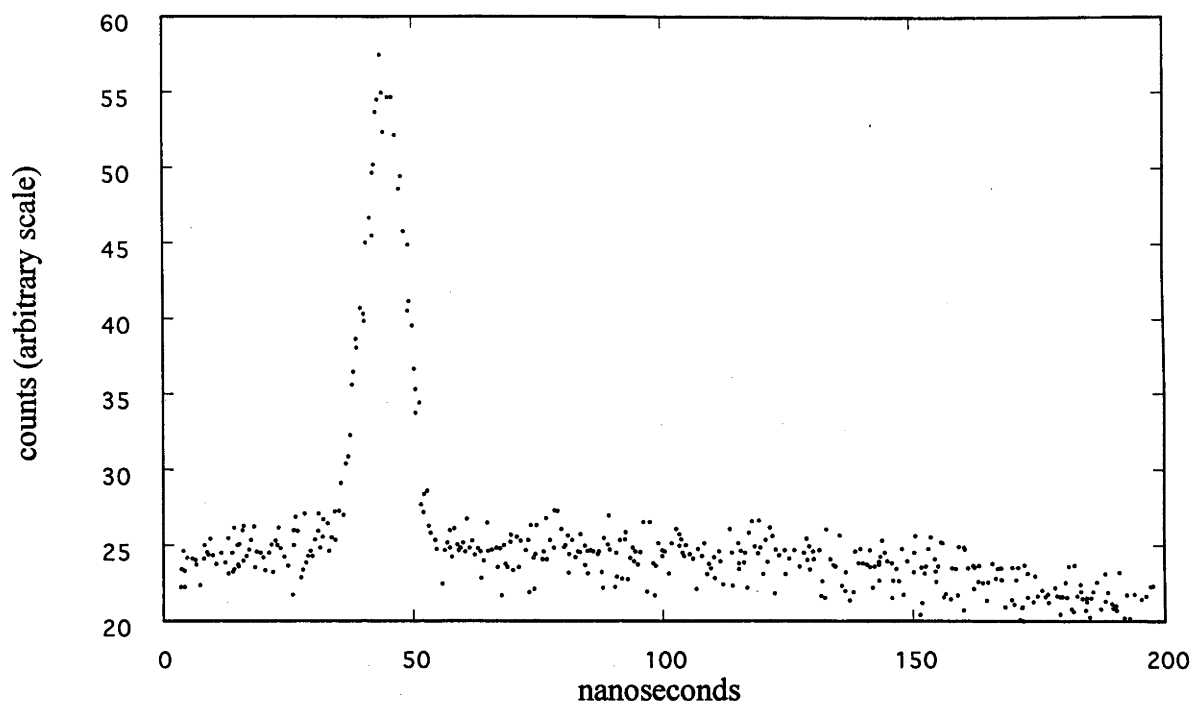
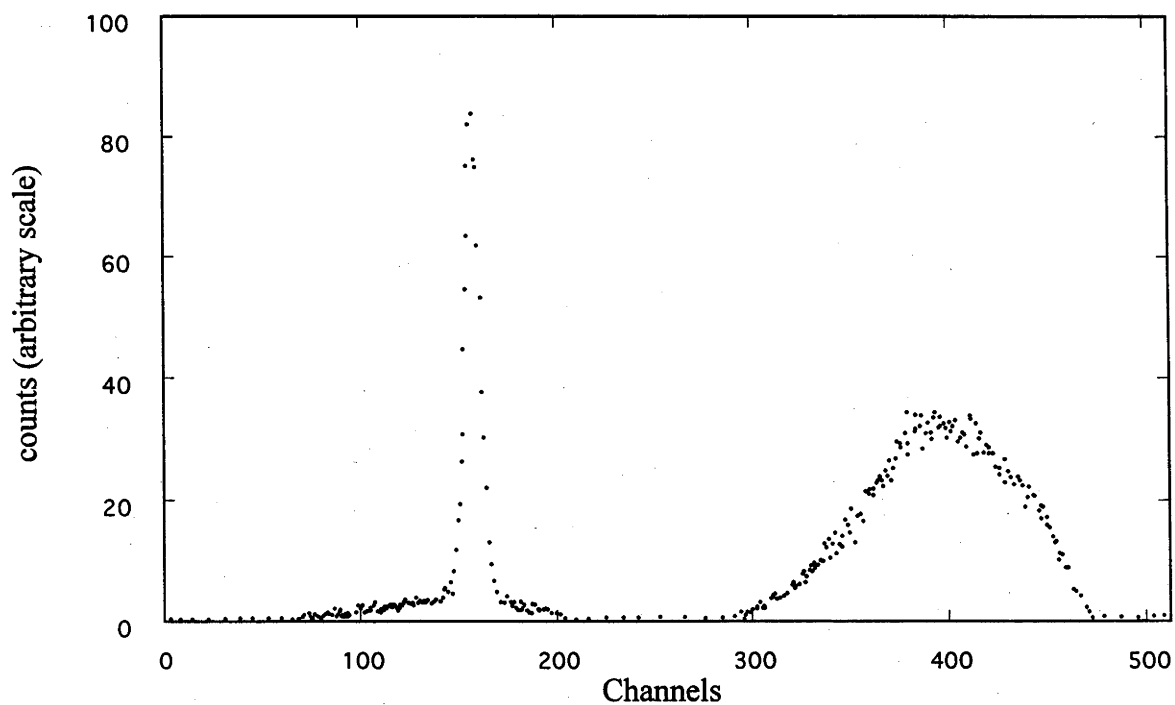Figure 4.12: The timing spectrum after flight time corrections.

Figure 4.13: A typical energy spectrum from the helium $^1S_{1/2}$ state, showing the signal (on the left) and the background (on the right), the background to signal window ratio being 10.

were amplified by a pre-amplifier and an amplifier and then summed in a dual sum and invert amplifier (DS&I). This summed pulse along with one of the pulses from the original pair was combined in a position sensitive detector analyser (PSDA) which produced an output of $A/(A+B)$, proportional to the energy E_e and E_l where E_l is the fixed lowest energy transmitted by the analysers. For simplicity E_l will be ignored in the following discussions.

The energy pulse from each pair was then sent to three paths. One path attenuated the pulse and was combined with the timing pulse to correct for the flight time variations as described above. Another path summed both energy pulses, $E_e + E_s$. The final path takes the pulse to SCAs where the energy pulses were suitably delayed to coincide with the timing pulses at the triple coincidence gate (TCG). Two TCGs were used, one for the coincidence signal and one for the random signal. The TCG only produced an output if the three pulses, that is, E_s, E_e, t_c or t_b arrived within a set time of each other. This pulse was then used to gate the dual linear gate (DLG) where the pulse being gated was the summed energy pulse.

The two linear gates provided input pulses to the multiplexer/router. One linear gate which was gated by the coincidence pulse, transmitted the summed energy pulse when a coincidence event was observed. The other gate transmitted summed energy pulses only for random or accidental coincidences (background events). The analogue input pulses from the multiplexer were received by a PCA card which produced digital signals which were stored and displayed on the computer. A typical energy spectrum is shown in figure 4.13 for the helium $^1S_{1/2}$ state. The first 0-255 channels stored the coincidence spectrum, while the next 256-512 channels stored the background spectrum. The subtraction of one from the other (using the background to coincidence window ratio, R) yielded the spectrum of true coincidence events, $N_t = N_c - N_b/R$. (Here R = 10, *i.e.*, the background is amplified 10 times, as shown in figure 4.13.)

The energy spectrum (or summed energy spectrum) has a triangular background as it is the convolution of both analysers. Each analyser has an electron energy distribution which is almost flat for the 6eV dispersion range. The energy spectrum therefore, has a dispersion range of 12eV, with a triangular background. As two peaks are being considered, the $^2P_{1/2}$ and $^2P_{3/2}$ ionisation peaks of xenon and one of the parameters being considered in this experiment is the ratio of the cross sections, this uneven efficiency function must be corrected for. This is discussed further in the data analysis in section 5.4.

The experiment was controlled by a PC 386 computer. A Master Board in the computer executed the programmes which controlled the experiment, including initialising (and stopping) the data collection, moving the ejected analyser and rotating the $\lambda/4$ plate (and hence controlling the spin direction of the incident electron beam).

4.3.4 Energy Resolution

The energy resolution of the entire system needed to be good enough to be able to resolve the two xenon states ($^2P_{1/2}$ and $^2P_{3/2}$) being considered in this experiment. That

is, it must be less than the energy gap of 1.31eV. The energy resolution was a convolution of the energy spread of the polarised electron beam and the energy resolutions of the two detectors. The energy resolution for the polarised electron beam was measured using the elastic peak of helium. It was measured to be ~0.5eV for a current of the order of ~150nA and included the analyser resolution. The experiment was operated with a current of about 100nA, where the resolution was constant.

The energy resolution in the hemispherical analysers depended on the voltages for the hemispheres, the gain on the multichannel plates and the electron optics used to focus the incoming electrons. The procedure for optimising the resolution in this part of the experiment was to set the voltages for the hemispheres, for a mean pass energy of 35eV and then to modify the MCP settings for a flat background response and suitable resolution. The final stage was to adjust the lens settings so as to compromise between a high signal (and therefore coincidence count rate) and a sufficiently good energy resolution. A helium autoionising peak was chosen to measure the energy resolution of the hemispheres. The autoionising states chosen were: $(2s^2)^1S$, $(2s2p)^3P$, $(2p^2)^1D$ and $(2s2p)^1P$ as they have been studied before (van den Brink *et al.*, 1989). At the same time the analysers could be calibrated, with either the autoionising states or an elastic helium peak. The energy resolution of each analyser was approximately 230meV. The total coincidence energy resolution achieved in these experiments was ~0.6eV. This was sufficient to resolve the peaks being investigated.

Chapter 5

The Xenon Experiment

As shown in chapter 3, spin polarisation effects are possible as the result of the interplay of exchange and the fine-structure effect. This spin effect results in spin asymmetries for excitation in xenon (Hanne, 1983). Preliminary results in Granitza et al. (1993) showed that an analogue to this effect was also possible for ionisation events, where a bound electron is excited to the continuum. To investigate the possibilities of spin polarisation effects, xenon was chosen as the target atom, due to the large energy separation between $^2P_{1/2}$ and $^2P_{3/2}$ ion ground states with ionisation energies of 13.44 and 12.13eV, respectively. Thus, ensuring that the fine-structure states are resolvable in the present experimental arrangement. After beginning these measurements, Jones, Madison and Hanne (1994) produced calculations for the (e,2e) reaction on xenon which showed that large spin effects may be expected at low energies for ionisation of the outer filled $5p$ valence shell. It is the aim of this experiment to further verify this.

Section 5.1   **Fine-structure Effect in the Ionisation of Xenon**

An intuitive explanation of the analogue of the fine-structure effect in ionisation of say, xenon is given in Hanne (1992), Shen (1995) and Granitza et al. (1996). The fine-structure effect for excitation was explained in section 3.3, however, as it is the basis for this experiment it is repeated here for ionisation. Figure 5.1 gives a simple picture of what happens in the ionisation of a noble gas. It is assumed that the incident electron beam is totally polarised, with the polarisation perpendicular to the scattering plane. The noble gas considered here is xenon, however, the following explanation applies to any noble gas (with the exception of helium).

Ionisation of xenon means that the closed $5p^6$ shell is broken, the transition being from $5p^6 \rightarrow 5p^5$. Spin-orbit interaction within the atom will split this $5p^5$ open shell into either a $^2P_{1/2}$ or a $^2P_{3/2}$ ionic core. Consider the event where the ionic core is in the $^2P_{1/2}$ state, where the approximation is made that the final state can be described as an **LS** coupled state and the spin-orbit interaction of the continuum electrons is negligible. Under such conditions, spin will be conserved in the reaction.
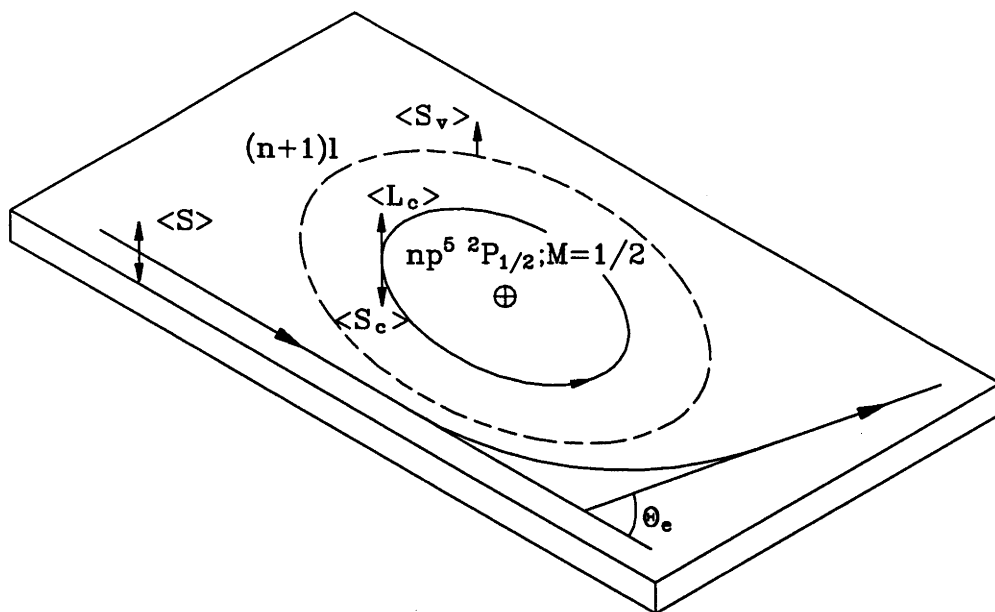
Figure 5.1: A picture showing the spin effects of the $5p^6 \to 5p^5$ transition.

This illustration is considered in the natural frame, *i.e.*, the quantization axis is perpendicular to the scattering plane, where there is only the possibility of exchange between the two final state continuum electrons (for the purposes of this discussion, the capture amplitudes are ignored). The possible reactions which lead to this ionisation process are listed in table 5.1, along with the partial TDCS.

Initial State	Final State					TDCS
	Ion			Electron (E_s)	Electron (E_e)	
	$Xe^+\,^2P_{1/2}$	m_s	m_l			
$e(\uparrow)+Xe\;(^1S_0)$	$Xe^+(\downarrow)$	-1/2	+1	$e(\uparrow)$	$e(\uparrow)$	$\lvert f_{+1} - g_{+1} \rvert^2$
	$Xe^+(\uparrow)$	+1/2	-1	$e(\uparrow)$	$e(\downarrow)$	$\lvert f_{-1} \rvert^2$
	$Xe^+(\uparrow)$	+1/2	-1	$e(\downarrow)$	$e(\uparrow)$	$\lvert g_{-1} \rvert^2$

Table 5.1: The possible reactions leading to the $^2P_{1/2}$ state with their corresponding partial cross sections and $\uparrow$, $\downarrow$ denote the spin projections for either the continuum electrons or the residual ion along the quantization axis (Granitza *et al.*, 1996).

If excitation of the $m_l = +1$ state is considered, then the orientation of the orbital angular momentum is positive and the spin orientation is negative ($m_J = m_l + m_s$). As the excitation is from a closed shell and the Pauli principle must hold, then the excited electron must have positive spin orientation. This process can not be classified as either direct or exchange scattering due to the indistinguishability of the two outgoing continuum electrons. Therefore, the amplitudes for both direct and exchange scattering must be added coherently as indicated in table 5.1.

The second two reactions listed in table 5.1, indicate that both direct and exchange scattering is possible in this illustration (which correspond to equations 3.6 and 3.5, respectively). In these cases the residual ion is left with a positive spin orientation. These processes are distinguishable, as the two final state continuum electrons have opposing spin orientations. Thus, for the $m_l = -1$ state, an incoherent sum of the direct and exchange scattering amplitudes is required.

Then the differential cross section, σ, for ionisation to the $J = 1/2$ final ion state with "spin up" incident electrons can be expressed in the following manner (Granitza *et al.*, 1996),

$$\sigma_{1/2}(\uparrow) = K\frac{2}{3}\left(|f_{-1}|^2 + |g_{-1}|^2 + |f_{+1} - g_{+1}|^2\right), \qquad \dots 5.1$$

where K is a kinematic factor and the subscript m_l, denotes the projection of the ion. Similarly an equation for "spin down" incident electrons can be expressed as,

$$\sigma_{1/2}(\downarrow) = K\frac{2}{3}\left(|f_{+1}|^2 + |g_{+1}|^2 + |f_{-1} - g_{-1}|^2\right). \qquad \dots 5.2$$

After a collision an atom may be oriented due to the Coulomb interaction (Anderson *et al.*, 1988), $\langle L_\perp \rangle \neq 0$. That is, the direct scattering amplitudes are not the same for different magnetic sub-levels of the atom, $f_{-1} \neq f_{+1}$, (nor are the exchange scattering amplitudes the same, $g_{-1} \neq g_{+1}$). Then from equations 5.1 and 5.2 it can be seen that the cross section for ionisation of the $\sigma_{1/2}$ will be different for incident spin up electrons from that for incident spin down electrons. This difference will show as a spin up-down asymmetry, which is expected to be measurable in this experiment.

5.1.1 Calculations of Xe (e,2e) Xe⁺ with Polarised Electrons

The experimental results presented here are compared with two theoretical calculations. One theory, described in part in section 3.4 (Guo *et al.*, 1995), is based on the density matrix formulation and is discussed in detail later. The other theory is that of Madison *et al.* (1996). This theory is also explained in Jones *et al.* (1994) and Madison *et al.* (1995, 1996) which presents the cross sections for the $J = 1/2$ state for incident spin up electrons as:

$$\sigma_{1/2}(\uparrow) = \frac{(2\pi)^4}{E_0}\frac{2}{3}\left(|f_{+1}|^2 + |g_{+1}|^2 + |f_{-1} - g_{-1}|^2\right). \qquad \dots 5.3a$$

where f_{m_n} and g_{m_n} are the direct and exchange scattering amplitudes respectively. Note here that the subscript m_n refers to the projection of the orbital angular momentum of the active electron removed from the atom (the ejected electron), which is simply the negative of the corresponding projection for the residual ionic core, m_l, which is the subscript used in section 5.1 and in Granitza *et al.* (1996). Similarly for incident spin down electrons:

$$\sigma_{1/2}(\downarrow) = \frac{(2\pi)^4}{E_0}\frac{2}{3}\left(|f_{-1}|^2 + |g_{-1}|^2 + |f_{+1} - g_{+1}|^2\right), \qquad \dots 5.3b$$

Then for the $J = 3/2$ state the cross sections are:

$$\sigma_{3/2}(\uparrow) = \frac{(2\pi)^4}{E_0}\left(|f_{-1}|^2 + |g_{-1}|^2 + \frac{1}{3}|f_{-1} - g_{-1}|^2\right.$$
$$\left. + \frac{1}{3}|f_{+1}|^2 + \frac{1}{3}|g_{+1}|^2 + |f_{+1} - g_{+1}|^2\right), \qquad \dots 5.4a$$

$$\sigma_{3/2}(\downarrow) = \frac{(2\pi)^4}{E_0}\left(|f_{+1}|^2 + |g_{+1}|^2 + \frac{1}{3}|f_{+1} - g_{+1}|^2\right.$$
$$\left. + \frac{1}{3}|f_{-1}|^2 + \frac{1}{3}|g_{-1}|^2 + |f_{-1} - g_{-1}|^2\right). \qquad \dots 5.4b$$

The origin of the asymmetry, A_J, (see equation 3.18) can then be seen to be in agreement with that derived using the simple physical argument as above. The formalism of Jones *et al.* (1994) is in the natural frame where the quantization axis is perpendicular to the scattering plane, hence there are no $m_l = 0$ terms.

The scattering amplitudes are calculated by the DWBA method (Jones *et al.*, 1994 and references therein). The direct and exchange amplitudes are given by Madison *et al.* (1996):

$$f_{m_n} = \left\langle \chi_a^-(0)\chi_b^-(1)\left|\frac{1}{r_{01}}\right| \alpha_n l_n m_n(1)\chi_i^+(0)\right\rangle, \qquad \dots 5.5$$

$$g_{m_n} = \left\langle \chi_a^-(1)\chi_b^-(0)\left|\frac{1}{r_{01}}\right| \alpha_n l_n m_n(1)\chi_i^+(0)\right\rangle \qquad \dots 5.6$$

where $\chi^{(\pm)}$ are the free electron distorted waves. The distorted incident electron wave used in the above calculation is derived as a solution of the following equation

$$\left(-\frac{1}{2}\nabla^2 + U_{atom}\right)\chi_i^+ = E_i\chi_i^+. \qquad \dots 5.7$$

As a non-relativistic Hamiltonian is used, the potential for the static interaction of the incoming electron with the ground state of the atom, U_{atom}, contains no spin dependent forces. Similarly, the outgoing distorted waves are solutions of

$$\left(-\frac{1}{2}\nabla^2 + U_f\right)\chi_j^- = E_j\chi_j^-, \qquad \dots 5.8$$

where $j = a$, b and $U_f = U_a + U_b$ (Madison *et al.*, 1996). The distorted waves are orthogonalised to the bound-state orbital of the active electron and the final state potential is,

$$U_f = z U_{ion} + (1-z) U_{atom} \ , \qquad \qquad ... 5.9$$

where a static-exchange potential for the ion, U_f, is used and the effective charge, z, is:

$$z = 1 - \frac{1}{2 \sin\left(\frac{\theta_{ab}}{2}\right)} \ . \qquad \qquad ... 5.10$$

This implies that the contribution to the asymmetry in this calculation is only due to exchange.

Jones *et al.* (1994) show that if a non-relativistic Hartree-Fock orbital is used, the agreement with the experimental data in terms of the branching ratios and the cross sections is poor. This suggests that some relativistic effects may be needed for the calculation of the asymmetry. Indeed Guo *et al.* (1995), show that a calculation of Madison *et al.* (1996), which uses a relativistic Dirac-Fock wave function improves the agreement with the experimental data. For this work, only the calculations based on Dirac-Fock orbital wave functions which still neglect the l•s interaction for both the continuum electron and the bound electron, will be used for comparisons. However, an example of a Hartree-Fock calculation is given in figure 5.13b to demonstrate this point.

Guo *et al.* (1996) express the asymmetry using the density matrix formalism and account for some relativistic interactions, see equation 3.28. The scattering amplitude is $f(v_s, v_e, m_i, v_0)$, where v_0, corresponds to a spin projection for the incoming electron and v_s, v_e, correspond to a spin projection for the scattered and ejected electron respectively. The ion is in the final state, $|J_i \, m_i \rangle$. This amplitude

$$f = \left\langle \chi_{v_s}^{(-)}(1) \chi_{v_e}^{(-)}(2) \left| \frac{1}{r_{12}} \right| \phi_{jlm} \, \chi_{v_0}^{(+)}(1) \right\rangle , \qquad \qquad ... 5.11$$

with $J_i = j$, and $m_i = -m$, is evaluated in a semi relativistic DWBA method with Dirac-Fock wave functions. It has no electron correlation in the final state or in the bound states, while the theory of Madison *et al.* (1996), includes some electron-electron correlation in the final state, via the effective charge. The relativistic interactions for the continuum electrons are included by solving the Schrödinger form of the Dirac equation.

The Dirac equation can be transformed into a Schrödinger type equation under certain approximations for the exchange term. The approximation involves neglecting the small component of the bound state orbital in the exchange term. This is justified, as the small component of the outer orbitals for an atom, such as xenon, contribute only a few percent (Sin Fai Lam, 1980). Through this transformation, relativistic corrections are added to the static potential. Further, the exchange term is approximated by the Furness-McCarthy local exchange potential (McCarthy *et al.*, 1977). The asymmetry is evaluated in the collision frame, where the quantization axis is along the direction of the incident electron beam. The inclusion of the l•s interaction in the potential does not have much effect at the kinematics considered in this work, in terms of the calculated asymmetry (Mazevet, 1996). An example of the negligible effect of the l•s interaction is shown in section 5.5.2 (figure 5.8b).

Section 5.2   **Kinematics**

The kinematics used are shown in figure 5.2. In this experiment, three different kinematic settings are considered. Each setting scans the 'ejected' electron (lower energy) angle, while three fixed angles are selected for the 'scattered' (higher energy) electron. The scattered electron is detected at an energy of $100 \pm 3eV$, while the ejected electron is detected at $35 \pm 3eV$. The polarised electron beam current as measured in the inner Faraday cup is 105nA, for an incident electron energy of 147eV. The fixed, scattered angles are $\theta_s = 28°$, $\theta_s = 15°$ and $\theta_s = 40°$. They were selected on the basis of expected reasonably large cross sections, to be on the Bethe-Ridge ($\theta_s = 28°$) and on either side of the Bethe-Ridge, with reasonably large momentum transfers.
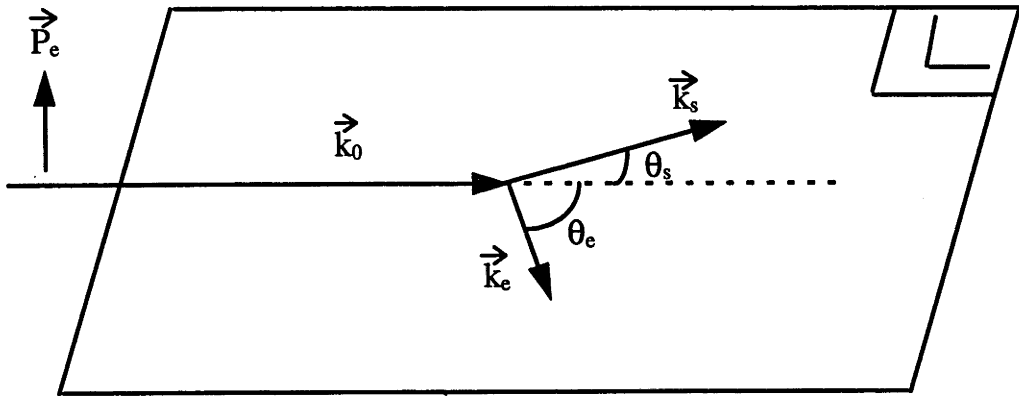

Figure 5.2: The kinematics for the experiment for this work, where $\vec{P}_e$ is the polarisation of the incident electron beam.

The fine-structure energy splitting between the ground states of xenon is 1.31eV, which is easily resolvable in the experiment, where the energy resolution of the experiment is 0.6eV (see section 4.3.4). The angular resolution of the experiment is better than 3°. A pressure of 6×10^{-6} Torr is maintained in the scattering chamber during the experiment. The minimum possible angle between the two hemispherical analysers is 56°. However, to thoroughly ensure that the hemispherical analysers could not make any contact with each other, the safety limits are set for a minimum angle of 60°. Thus, defining the minimum angles at which the measurements could be taken (see table 5.2). A polarisation of 0.24 ± 0.03 is measured with the Mott polarimeter and is constant throughout the experiment.

An example of an energy spectrum is shown in figure 5.3, for both incident electron spin up and spin down, at $\theta_s = 40°$ and $\theta_e = 40°$. Typically, the (e,2e) count rates are in the range of one to 10 counts per minute.

An elastic scattering experiment is conducted to ensure that the direction of the polarisation, *i.e.*, spin up and spin down, is correct and consistent. This experiment is performed at an incident energy of 50eV, on xenon. The Sherman function is measured (equation 3.4) and compared to the results of Müller and Kessler (1994) and are used as a consistency check for the measured polarisation. The data are reported in Shen (1995) and shows that the magnitude and direction of the polarisation are indeed correct.
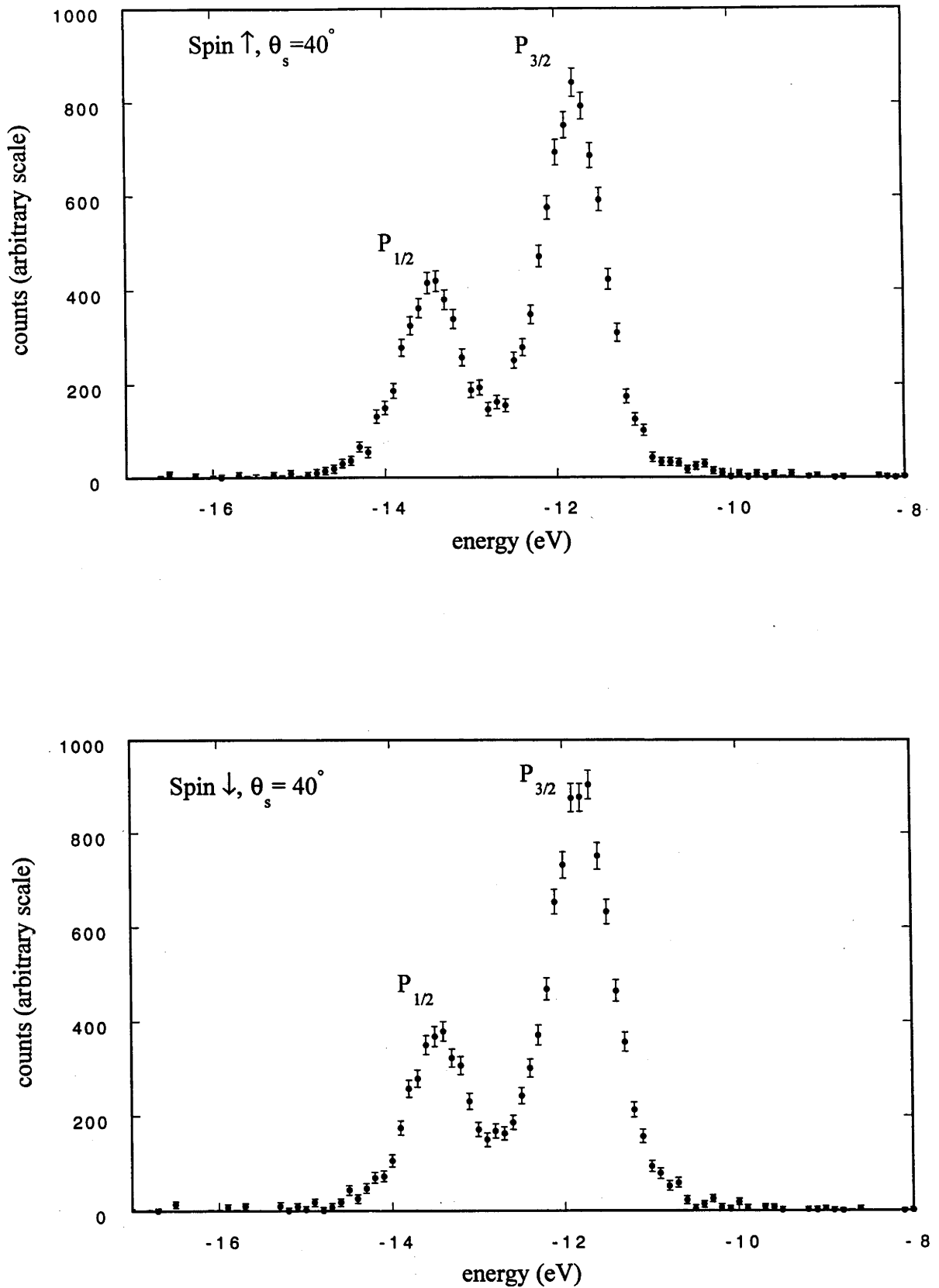
Figure 5.3: A typical energy spectrum for spin up and spin down incident electrons, where the incident energy is 147eV, the scattered electron is detected at 100eV at $\theta_s =$ 40° and the ejected electron is detected at 35eV at $\theta_e =$ 40°. Clearly the $^2P_{1/2}$ state is larger for spin up than for spin down incident electrons.

Section 5.3   **Measured Parameters and Quantities**

The experimental data may be expressed in a number of ways, (see appendix A for the tabulated values of the derived quantities). Of primary importance is the asymmetry parameter, which is:

$$A_J = \frac{1}{P_e} \frac{N_J(\uparrow) - N_J(\downarrow)}{N_J(\uparrow) + N_J(\downarrow)} \qquad \ldots 5.11$$

where $N(\uparrow)$ represents the counts measured for an incident electron beam with spin up and $N(\downarrow)$ represents the counts measured for an incident electron beam with spin down under identical conditions, with a polarisation of 24%. These numbers, $N(\uparrow)$ and $N(\downarrow)$ are converted to relative cross sections, $\sigma_J(\text{spin})$, for an incident electron beam with 100% polarisation in the following manner:

$$\sigma_J(\uparrow) = \frac{1}{2P_e}\left[(1+P_e)N_J(\uparrow) - (1-P_e)N_J(\downarrow)\right] \qquad \ldots 5.12$$

and

$$\sigma_J(\downarrow) = \frac{1}{2P_e}\left[(1+P_e)N_J(\downarrow) - (1-P_e)N_J(\uparrow)\right] \qquad \ldots 5.13$$

where P_e is the polarisation of the incident electron beam. The asymmetry calculation in equation 5.11 can be cross checked immediately, as it can also be expressed as:

$$A_J = \frac{\sigma_J(\uparrow) - \sigma_J(\downarrow)}{\sigma_J(\uparrow) + \sigma_J(\downarrow)}. \qquad \ldots 5.14$$

If the small kinematical difference due to the different energies of the fine-structure states is ignored, *e.g.*, the ionisation energies are the same for both $^2P_{1/2}$ and $^2P_{3/2}$ states, then it can be seen that $\sigma_{3/2} = 2\sigma_{1/2}$ (Madison *et al.*, 1996). And in the limit of the non-relativistic fine-structure effect, the asymmetries for each J_i state are related by,

$$A_{1/2} = -2A_{3/2}, \qquad \ldots 5.15$$

due to the statistical weighting of the states. However, it is more interesting to consider the case where the fine-structure states are summed over and averaged, according to the relative statistical weights,

$$A(\text{avg}) = \frac{A_{1/2} + 2A_{3/2}}{3}. \qquad \ldots 5.16$$

In the pure fine-structure effect the asymmetry would be zero if the fine-structure states were degenerate (and hence not resolved).

Further to the asymmetries, the branching ratios for the fine-structure states can be considered. This is done for spin up and spin down incident electrons:

$$R(\uparrow,\downarrow) = \frac{\sigma_{3/2}(\uparrow,\downarrow)}{\sigma_{1/2}(\uparrow,\downarrow)}. \qquad\qquad ...5.17$$

It is then a simple step to consider the spin averaged branching ratio:

$$R(avg) = R(\uparrow+\downarrow) = \frac{\sigma_{3/2}(\uparrow)+\sigma_{3/2}(\downarrow)}{\sigma_{1/2}(\uparrow)+\sigma_{1/2}(\downarrow)}. \qquad\qquad ...5.18$$

The total cross section, σ_{total}, is obtained from an angular correlation experiment for each scattered angle setting (as defined in section 5.4). More information about the cross sections is obtained in the asymmetry experiments. Therefore, to use all available information about the cross sections, the asymmetry and branching ratio information is folded into the original total cross section data. This is simply done using the following set of equations. The unpolarised cross sections are:

$$\sigma_{1/2} = \frac{\sigma_{total}}{1+R(avg)} \quad ; \quad \sigma_{3/2} = \frac{\sigma_{total}}{1+1/R(avg)}. \qquad\qquad ...5.19$$

where $\sigma_{total} = \sigma_{1/2} + \sigma_{3/2}$. The spin polarised cross sections for $J = 1/2$, $3/2$ are (for incident spin up and spin down electrons, respectively):

$$\sigma_J(\uparrow) = \sigma_J[1+A_J] \quad ; \quad \sigma_J(\downarrow) = \sigma_J[1-A_J], \qquad\qquad ...5.20$$

where $\sigma_J = [\sigma_J(\uparrow) + \sigma_J(\downarrow)]/2$. For completeness, the equations used for the error analysis are included in the final part of appendix A.

Section 5.4   Data Analysis

The experimental data is collected and stored in the computer, as discussed in section 4.3. As the data is collected over several weeks, each experiment is broken into manageable sections, call a run. During a run, the program is setup to measure a certain angular range for each fixed, scattered angle setting. Usually, only one or two runs are performed scanning the entire angular range of the ejected angle for each scattered angle setting. These are the angular correlation runs. Most of the data is collected in runs which are arranged to collect data at one ejected angle, for one of the scattered angle settings. This is for many reasons for example, the files are easier to manage and it is easier to maintain constant conditions for the experiment.

Furthermore, each run is divided into scans. These scans can be individually examined after the experiment. The scans are again segmented so as to collect data for both incident spin up and incident spin down electrons. A scan can include up to 20 different angular settings (each collecting data for incident spin up and incident spin down electrons). Each run is collected over approximately the same time frame, usually 24 hours (except the angular correlation runs which are kept running as long as possible,

up to 3 days). A scan for a one angular setting, usually runs for between 20-40 minutes, which varies according to the cross sections, *i.e.*, the larger the cross sections, the smaller the scans.

The raw data is extracted using analysis programs that have been developed for (e,2e) experiments. The extracted data is the signal minus background, as per equation 4.13. Each run is then carefully checked, scan by scan, for any anomalies which may have occurred, for example, as the result of a power glitch. At the same time the spectrum can be checked for any energy drifts during a particular run, which manifest themselves as a shift in the position of the energy peaks. However, there is essentially no evidence of energy drifting over the course of these experiments.

During the collection of data, the energy peaks are monitored. These peaks, the $^2P_{1/2}$ and $^2P_{3/2}$ ionisation peaks, have different energies and are therefore located at different positions on the energy spectrum. Since these measurements are dependent upon the distribution of counts in two adjacent peaks, it is important to compensate for the efficiency function, as discussed in section 4.3.3.

This compensation of the energy spectrum is done by correcting the energy spectrum for the background function. A program, called, 'transfit' was designed to do this. The first step is to approximate the shape of the background. Ideally, the background is triangular in shape, which can simply be fitted with two straight lines. However, as this is a real experiment, the background 'curve' is divided into straight line segments, each of which are fitted with a straight line, using the least squares method. The number and position of straight line segments are initially judged by eye. To ensure that these are the best approximations for the background, the background function is corrected for using the same background function. If the approximation is good, the result should be a continuous straight line. An iteration process ensures that the best result is achieved. Once the best background fit has been established, the energy spectrum containing the data are corrected for the detection efficiency function. That is, a transmission function file is produced which has had the background approximation removed from the energy spectrum. This spectrum is then analysed further to yield the numbers required, *i.e.*, the relative cross sections.

A program called 'globe fit' (in which the algorithms are constructed from Bevington, 1969) is employed to extract the relative cross sections from the energy spectrum. Globe fit has been used for analysing (e,2e) data at Flinders University for many years. The object of this program is to fit a number of gaussians to each peak and calculate the area under the peaks. In this instance three gaussians are assigned to each peak. These gaussians are assigned by height, position and width. For each gaussian, the position is kept the same and the distance between the two peaks is fixed (as it is known that the peaks are 1.31eV apart, which from the energy calibration is known to be 16.6 channels). An example of the fitting is shown in figure 5.4. To check that this method of peak fitting gave a good result, the data was analysed by an alternate method.

This second method simply sums the number of counts in each peak. As the two peaks are partially superimposed, *i.e.*, not completely separated, it is necessary to establish a sensible way to determine the range to be summed for each peak. The range is

labelled in channel numbers as in figure 5.4, (energy spectra are conventionally shown as an energy scale as in figure 5.3). The start channel for the $^2P_{1/2}$ peak and the end channel for the $^2P_{3/2}$ peak are arbitrarily chosen. These channels are not significant as the first and last sections of the energy spectrum contain essentially zero counts. The difficult part is to determine the best place to end the $^2P_{1/2}$ peak and to start the $^2P_{3/2}$ peak. The most satisfactory method is to simply define the position of the overlap as the channel to end the $^2P_{1/2}$ peak and one channel further as the start of the $^2P_{3/2}$ peak. This overlap position is defined by the globe fit curves. The sums are then performed for the chosen channel ranges yielding areas for each peak. These areas are similar to those calculated with globe fit.
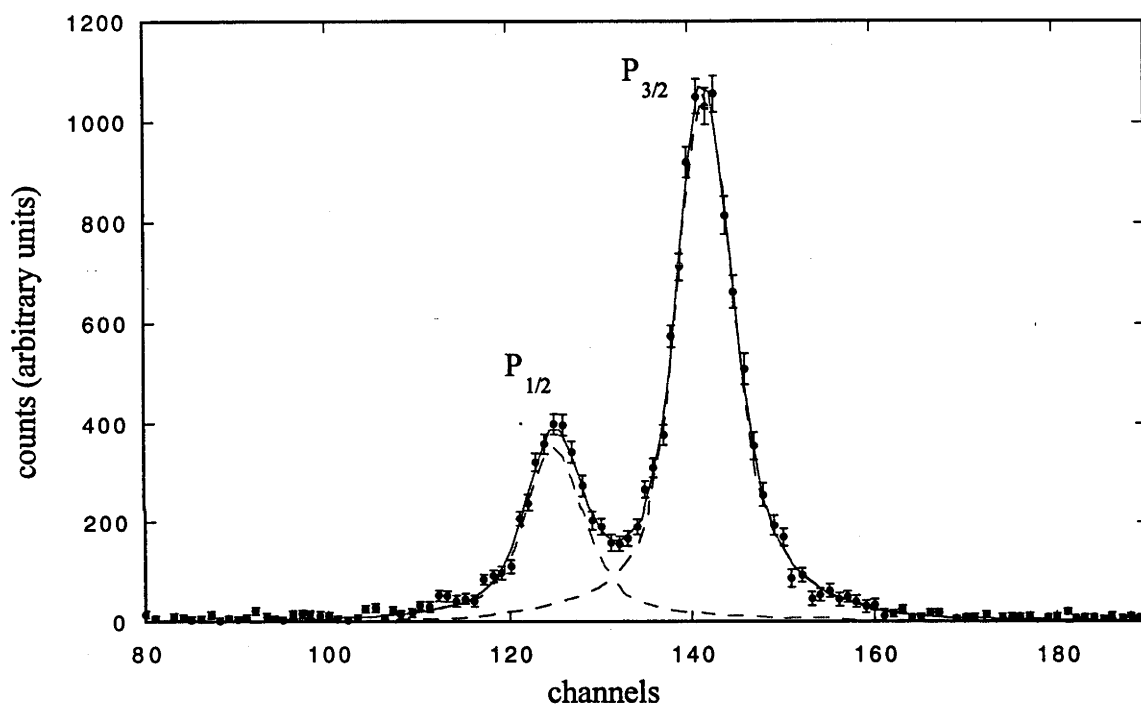

Figure 5.4: A binding energy spectrum for Xe (e,2e) Xe$^+$ ground state transitions, with curve fitting from the globe fit program, $\theta_s = 28°$ and $\theta_e = 35°$ for spin down incident electrons.

Eventually, it is the results from globe fit which are used, as the method of curve fitting is more rigorous and therefore more reliable. However, the associated error counts are taken from the summing method, as it is not clear that the errors produced in the globe fit program are correct. The summing method gives a larger error count and is therefore presumed to be a more appropriate estimate of the errors.

The final stage of the analysis is to calculate the parameters as discussed in section 5.3. These calculations are done in an MS Excel spreadsheet. Lastly, the errors for each parameter are calculated. These are calculated from the original numbers, using the standard derivative method (*e.g.*, Bevington, 1969). The raw data derived from the globe fit method and the parameters for all three kinematics are documented in appendix A.

Section 5.5   **Results and Discussion**

The experimental results are compared with the DWBA theoretical calculations of Mazevet (1996) and Madison *et al.* (1996). Recall that the essential difference in the theories is that the former includes a further exchange interaction between the continuum electrons and the ion. For comparison between the theories and the experimental data, the cross sections are normalised to the theory of Mazevet (1996), which is discussed in section 5.5.1. However, the measured asymmetry and branching ratios are compared directly to the theoretical calculations, that is, no normalisation is required for these parameters. The error analysis is restricted to statistical error calculations, which are shown on each graph.

So that the results can be seen clearly, the parameters are presented separately, that is, the asymmetry parameters for $^2P_{1/2}$ and for $^2P_{3/2}$ are on individual graphs. Similarly, the branching ratios are separated according to the direction of incident electron spin polarisation. Each set of parameters is presented in order of the scattering angle, first $\theta_s = 15°$ then $\theta_s = 28°$, followed by $\theta_s = 40°$ and are plotted as a function of θ_e, the ejected electron angle. The quantities, K, the momentum transfer and it's direction, θ_K, are presented in table 5.2.

θ_s	K (a.u.)	θ_K	θ_e (minimum)	θ_e (maximum)
15°	0.97	46.4°	45°	90°
28°	1.56	54.9°	32°	95°
40°	2.12	55.2°	20°	100°

Table 5.2: The corresponding kinematic conditions, the momentum transfer, K, the direction of momentum transfer, θ_K, and the angular range of the ejected electron, θ_e, for the three scattered angles, θ_s, considered in this work.

The range of the ejected electron angle is primarily restricted by the physical size of the analysers, the position of the incident electron beam optics and the Faraday cup. However, the small cross sections at larger backward angles made data collection impractical as the collection times would need to be very long to be able to obtain reasonable statistics.

5.5.1 Cross Sections

The measured cross sections are relative and therefore need to be normalised. The normalisation point was chosen to be at $\theta_e = 45°$, the binary peak, on the $^2P_{1/2}$ state as it is close to the maximum of the cross section and has good statistics. The experimental data and the theory of Madison *et al.* (1996) is normalised to the theory of Mazevet (1996) by a normalisation factor, *N*, for each scattered angle. The normalisation factors for theory of Madison *et al.* (1996) are listed in table 5.3.

θ_s	N (Madison theory)
15°	0.94
28°	1.30
40°	0.90

Table 5.3: The normalisation values for the experimental data and the theory of Madison *et al.* (1996) where N is the normalisation factor, *i.e.*, for comparison at $\theta_s = 15°$, the theory of Madison *et al.* (1996) is multiplied by 0.94 for $\theta_s = 15°$, to be compared to the theory of Mazevet (1996).

The state resolved cross sections, are shown in figures 5.5. These clearly show that ionisation to the $^2P_{3/2}$ state is about twice as likely as ionisation to the $^2P_{1/2}$ state, in all three settings. Note that each graph has a different y-axis maximum, which directly reflects the cross sections, *i.e.*, for the state resolved cross sections, the maximum on the scale is, 1.2, 0.4, and 0.12 for $\theta_s = 15°$, 28° and 40°, respectively.

It is obvious at $\theta_s = 15°$, that both of the theories underestimate the $^2P_{3/2}$ state cross section, although the theory of Mazevet (1996) is quite close to the experimental data. This has implications for the branching ratios which is discussed later. The agreement for the $^2P_{1/2}$ state cross sections is excellent for both theories. At $\theta_s = 28°$ the cross section is dominated by two lobes, located at about $\theta_e = 45°$ and 75°, as would be expected for ionisation of a p electron in the binary region under Bethe-Ridge conditions. The experimental data at $\theta_s = 28°$, clearly shows an angular shift, of about 5°, relative to both theoretical calculations for both $^2P_{1/2}$ and $^2P_{3/2}$ state cross sections. The theories at this setting differ slightly in the prediction of the magnitude of the second (sometimes called backward) lobe, where the semi-relativistic calculation of Mazevet (1996) is closer in magnitude to the experimental data. However, both theories underestimate the first (or forward) lobe (located about $\theta_e = 45°$), while overestimating the second lobe (located about $\theta_e = 75°$).

For $\theta_s = 40°$, the large error bars are due to the small cross section and indicate that a longer counting time may be needed to improve the statistics. The agreement between theories and the experimental data is good, although again the theory of Mazevet (1996) predicts the magnitude of the $^2P_{3/2}$ cross section better than the theory of Madison *et al.* (1996).

Of course, the comparisons between theory and experiment are similar for the total cross sections in all cases. These are presented in figures 5.6 to confirm the trends set for the state resolved cross sections. At $\theta_s = 15°$, the theory of Mazevet (1996) is in good agreement with the experimental data, however, the calculation of Madison *et al.* (1996) slightly underestimates the magnitude of the cross section. There is a marked difference between the theories and the experimental data at $\theta_s = 28°$. Here, the calculation of Madison *et al.* (1996) using Dirac-Fock wave functions overestimates both lobes, while the theory of Mazevet (1996) underestimates the first lobe located at $\theta_e = 45°$, while slightly overestimating the second lobe, relative to the experimental data. The agreement with the theory is good at $\theta_s = 40°$, although this may be deceptive due to

the poor statistics. The theory of Madison *et al.* (1996) is smaller in magnitude at the peak of the cross section, at $\theta_e = 50°$.

The final cross sections presented are the spin resolved cross sections. That is, for each fine-structure state there are two cross sections, either for incident spin up (denoted spin ↑) or spin down (denoted spin ↓) electrons. Again, these results follow the trend determined for the state resolved cross sections. For completeness, the entire set of these cross section data are shown in figures 5.7. It is notable that the statistics decrease the more the data is separated, *i.e.*, the error bars increase for the spin resolved cross sections and that the scatter of the experimental results is more prominent. These results are outlined here.

The agreement between the theoretical calculations and the experimental data at $\theta_s = 15°$ is quite good. It is noticeable that the spin down $^2P_{1/2}$ cross section has a slightly higher magnitude than the spin up cross section. The DWBA calculations of Madison *et al.* (1996) overestimates the spin up $^2P_{1/2}$ cross section and underestimates the spin down $^2P_{1/2}$ cross section. For the $^2P_{3/2}$ ionisation state, the spin up cross section is higher in magnitude than the spin down $^2P_{3/2}$ cross section. Both theories underestimate the spin up $^2P_{3/2}$ cross section, but closely approximate the $^2P_{3/2}$ spin down cross section.

At $\theta_s = 28°$ there is an immediately obvious difference between the spin up and spin down relative cross sections for both fine-structure states. Firstly for the $^2P_{1/2}$ state, the theoretical predictions agree well for the spin up cross section and the 5° angular shift relative to the experimental data is again evident. It is clear that the first lobe is much larger in magnitude for spin up incident electrons than for spin down incident electrons. Conversely, the second lobe (located about $\theta_e = 75°$), has a larger magnitude for spin down incident electrons. For the $^2P_{3/2}$ fine-structure state, the theories agree, with an exception at the second lobe in the spin up cross section, where the DWBA calculation of Madison *et al.* (1996) overestimates the magnitude, compared to the experimental data. The difference between spin up and spin down is seen mainly in the first lobe, where the spin down cross section is greater in magnitude, while the second lobe is slightly larger for the spin up cross section.

An interesting aspect of the $\theta_s = 40°$ spin resolved cross sections is the differences in shape between the two theories. For the $^2P_{1/2}$ fine-structure state cross section with spin up electrons, the semi-relativistic theory of Mazevet (1996) predicts a peak about $\theta_e = 50°$ and a shoulder about $\theta_e = 75°$. At the same time, the theory of Madison *et al.* (1996) predicts one broad peak about $\theta_e = 60°$. It is however, the opposite for incident spin down electrons, where Madison *et al.* (1996) predicts a peak about $\theta_e = 45°$ and a shoulder at $\theta_e = 75°$ while Mazevet (1996) predicts an asymmetric peak. In both cases the experimental data is better represented by the semi-relativistic calculation of Mazevet (1996). The difference between the theories is not as pronounced for the $^2P_{3/2}$ state spin resolved cross sections. There are however, hints of a shoulder in the theory of Madison *et al.* (1996) for spin up incident electrons and conversely, in the theory of Mazevet (1996) for spin down incident electrons. Again the experimental data appears to be in better agreement with the semi-relativistic calculation of Mazevet (1996), but it is not clear that it is the best calculation in this case.
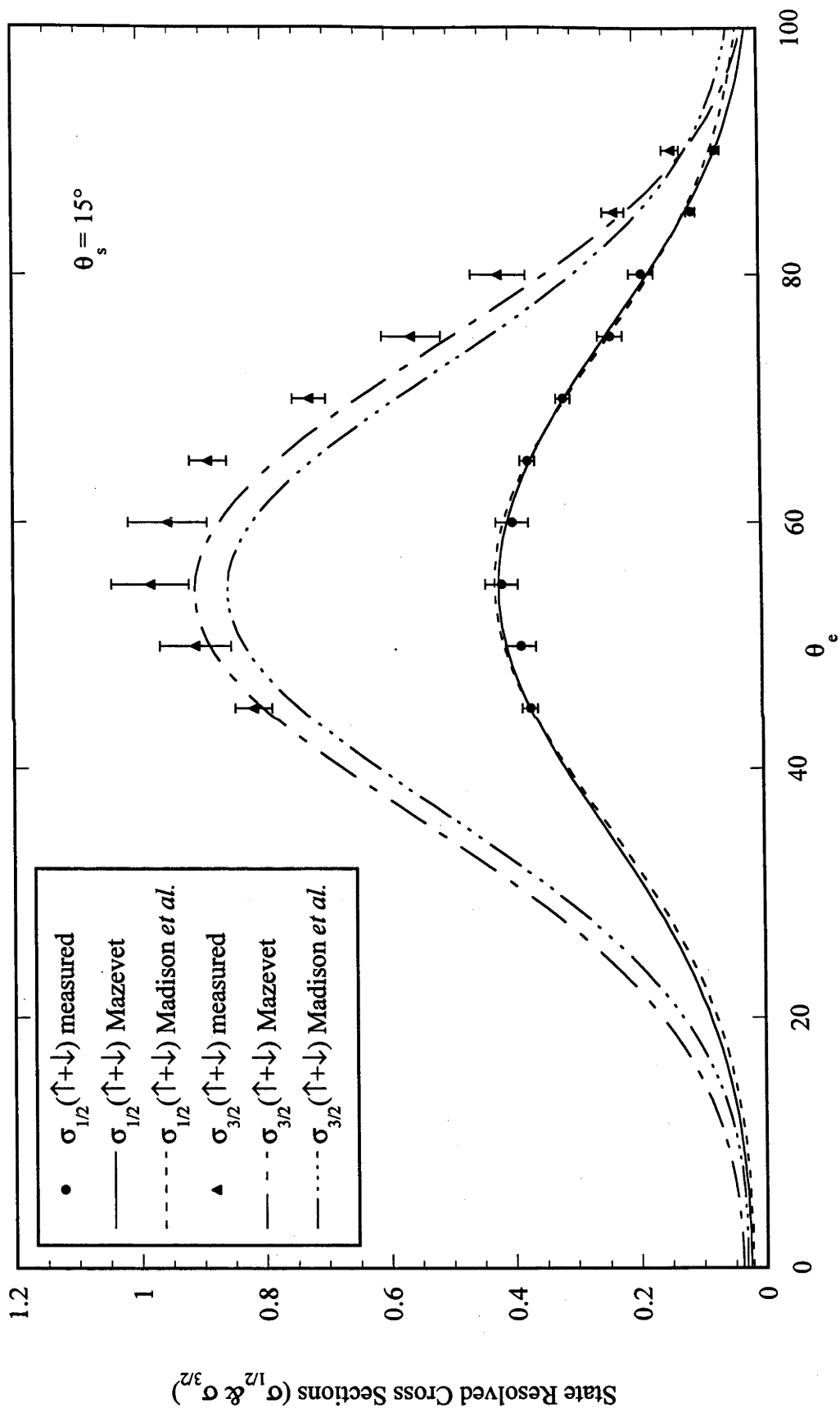
Figure 5.5a: The $^2P_{1/2}$ and $^2P_{3/2}$ state cross sections compared to the theories of Mazevet (1996) and Madison *et al.* (1996) at $\theta_s = 15°$.
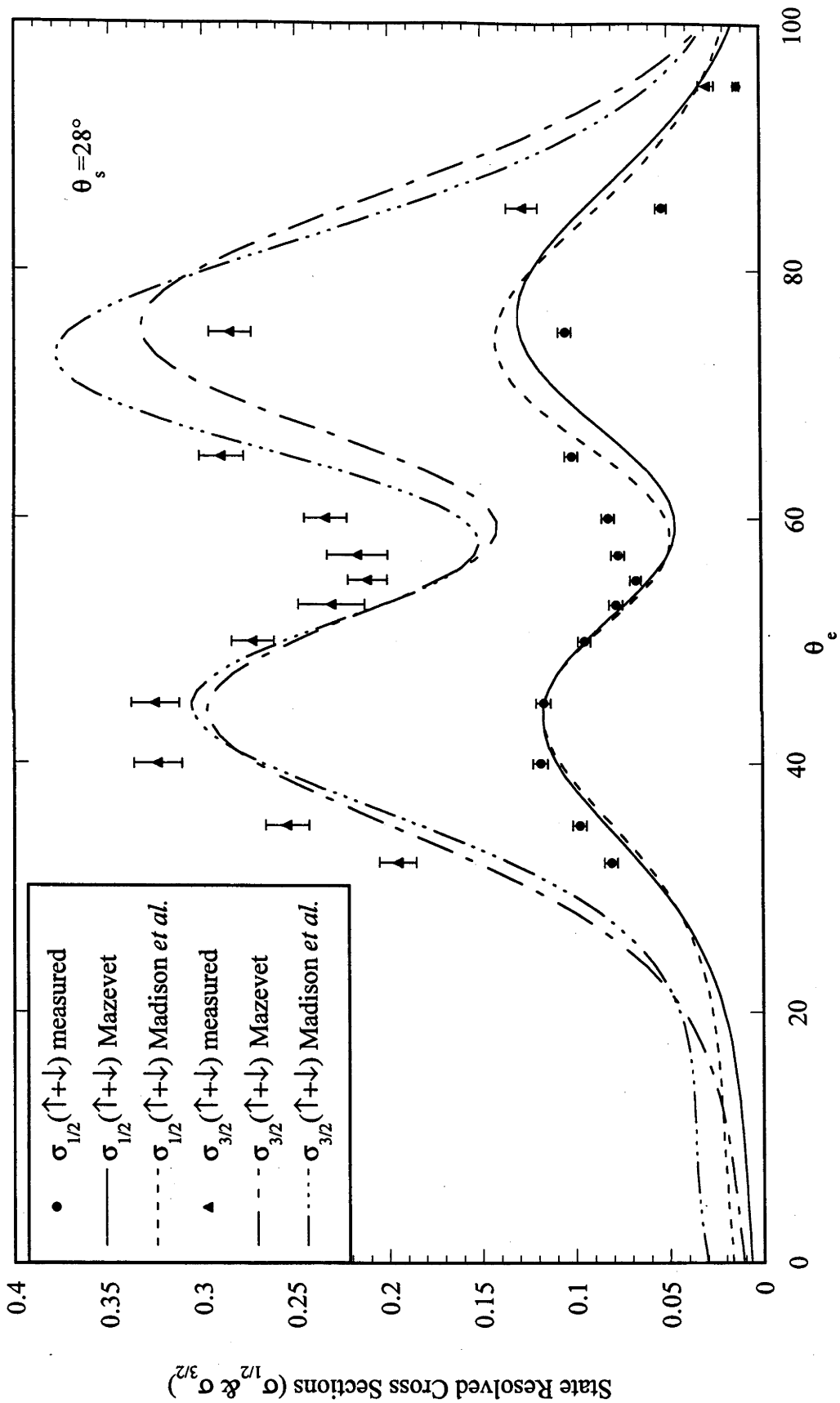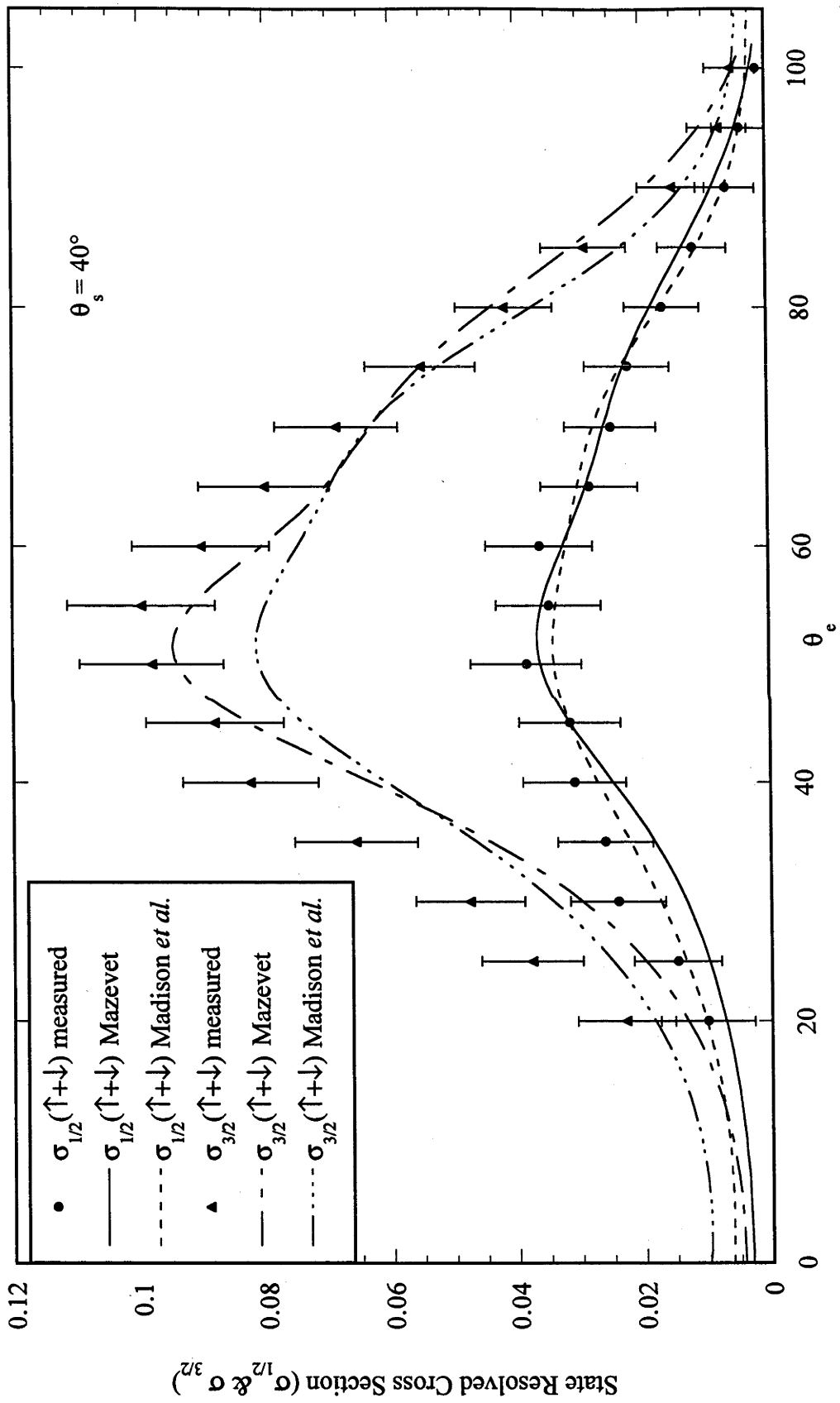
Figure 5.5b: The $^2P_{1/2}$ and $^2P_{3/2}$ state cross sections compared to the theories of Mazevet (1996) and Madison *et al.* (1996) at $\theta_s = 28°$.

Figure 5.5c: The $^2P_{1/2}$ and $^2P_{3/2}$ state cross sections compared to the theories of Mazevet (1996) and Madison *et al.* (1996) at $\theta_s = 40°$.
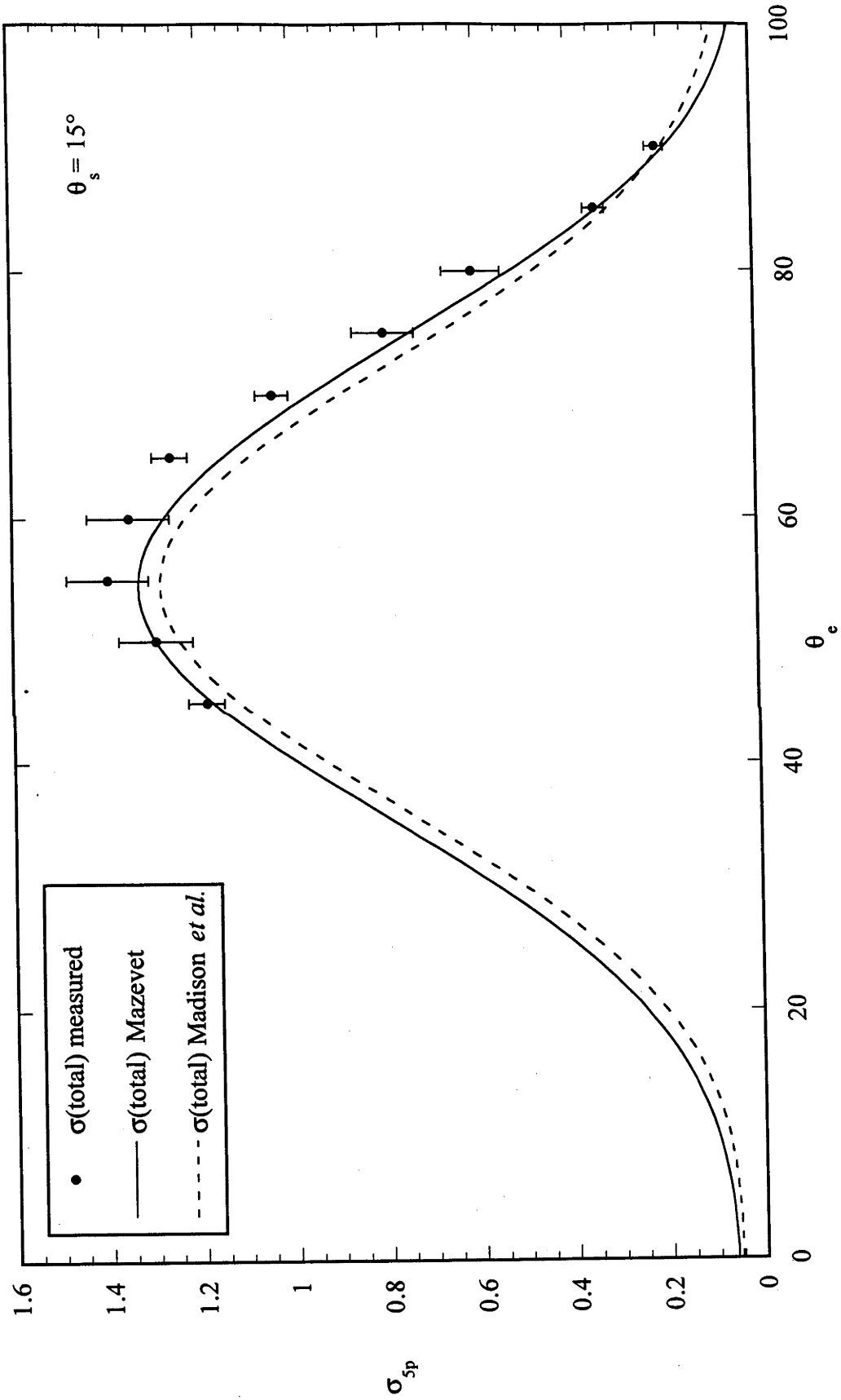
Figure 5.6a: Total cross section at $\theta_s = 15°$ compared to the theories of Mazevet (1996) and Madison *et al.* (1996).
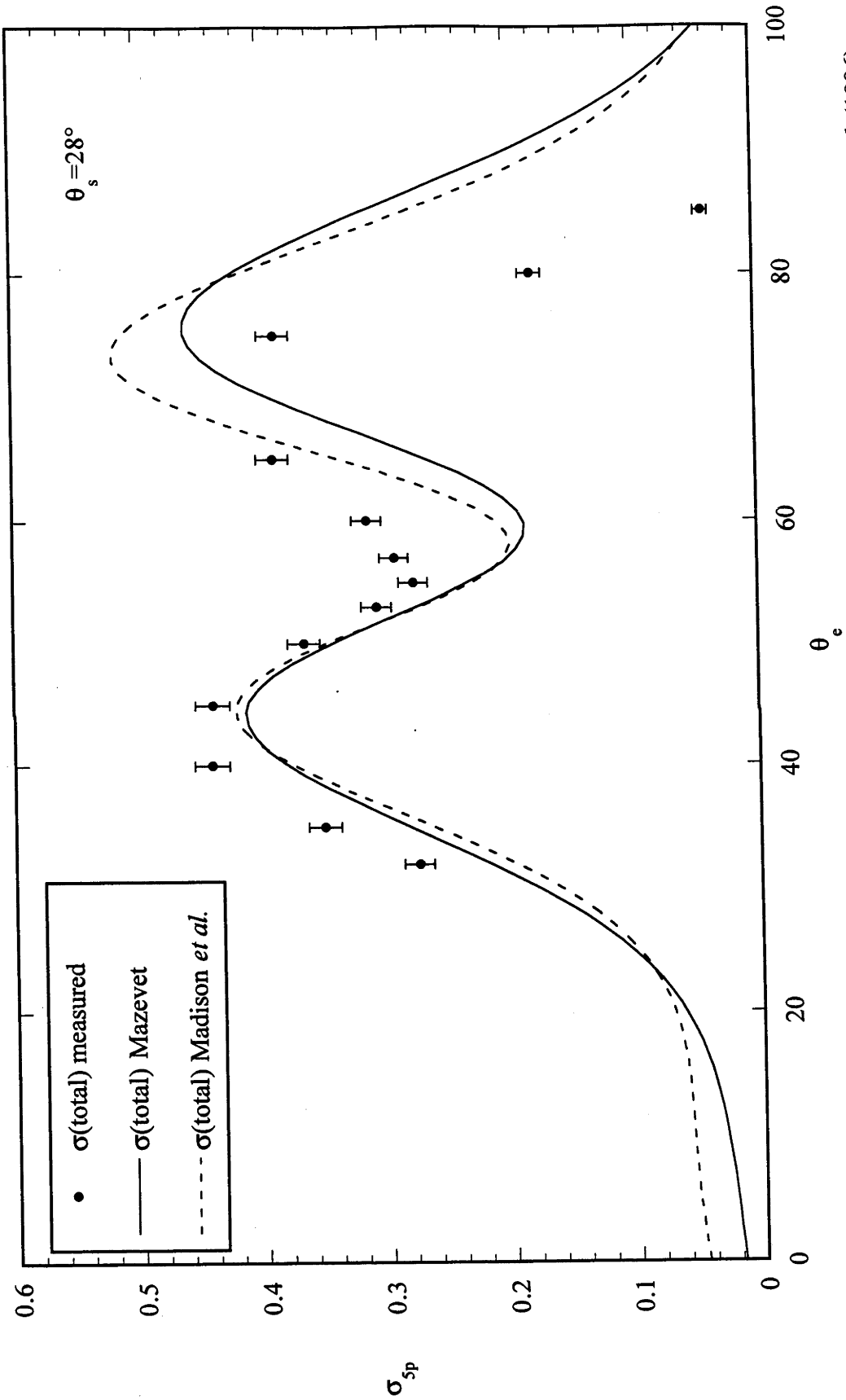
Figure 5.6b: Total cross section at $\theta_s = 28°$ compared to the theories of Mazevet (1996) and Madison *et al.* (1996).
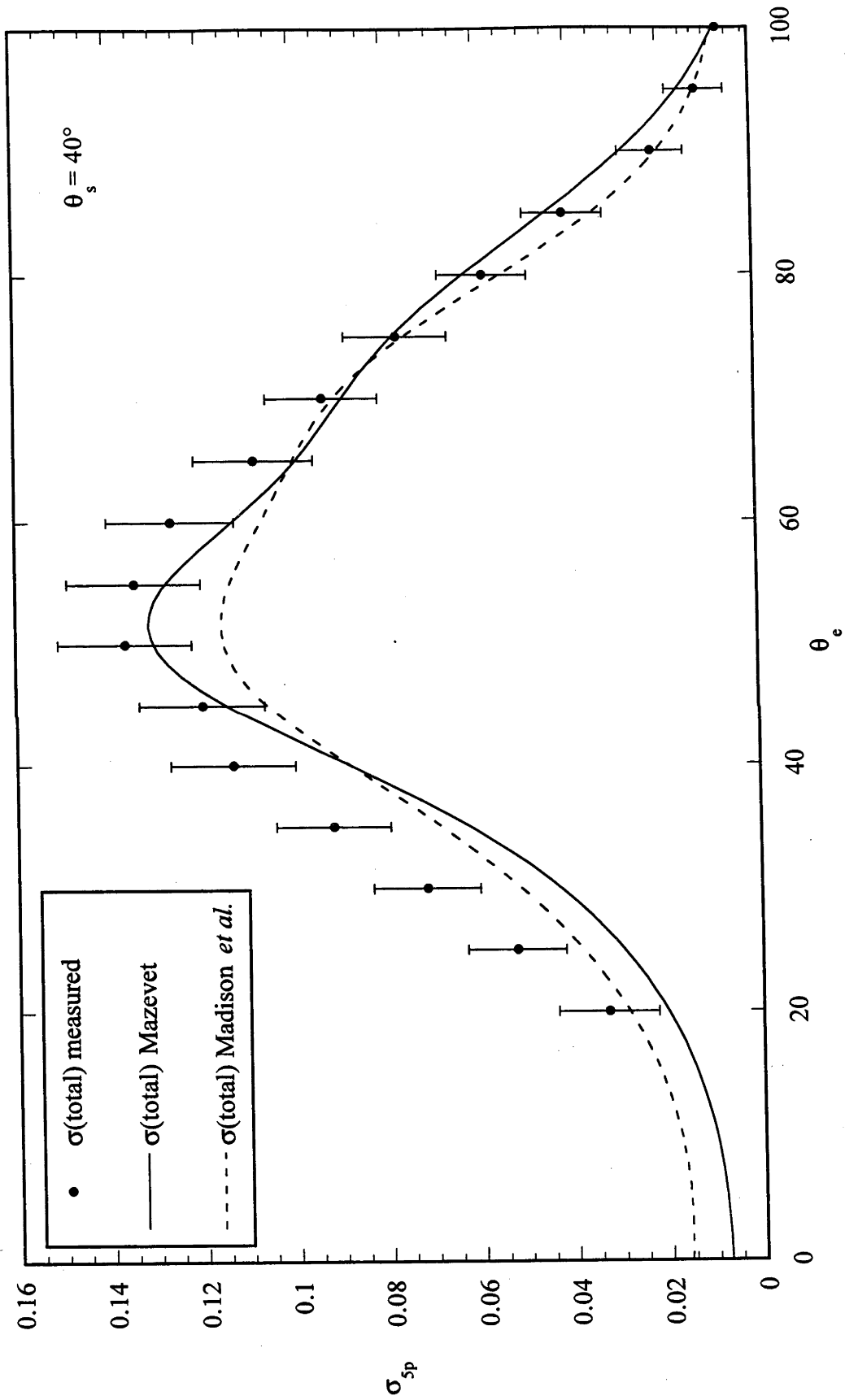
Figure 5.6c: Total cross section at $\theta_s = 40°$ compared to the theories of Mazevet (1996) and Madison *et al.* (1996).

Figure 5.7a: Spin resolved cross sections for the $^2P_{1/2}$ state, compared to the theories of Mazevet (1996) and Madison *et al.* (1996) at $\theta_s = 15°$.
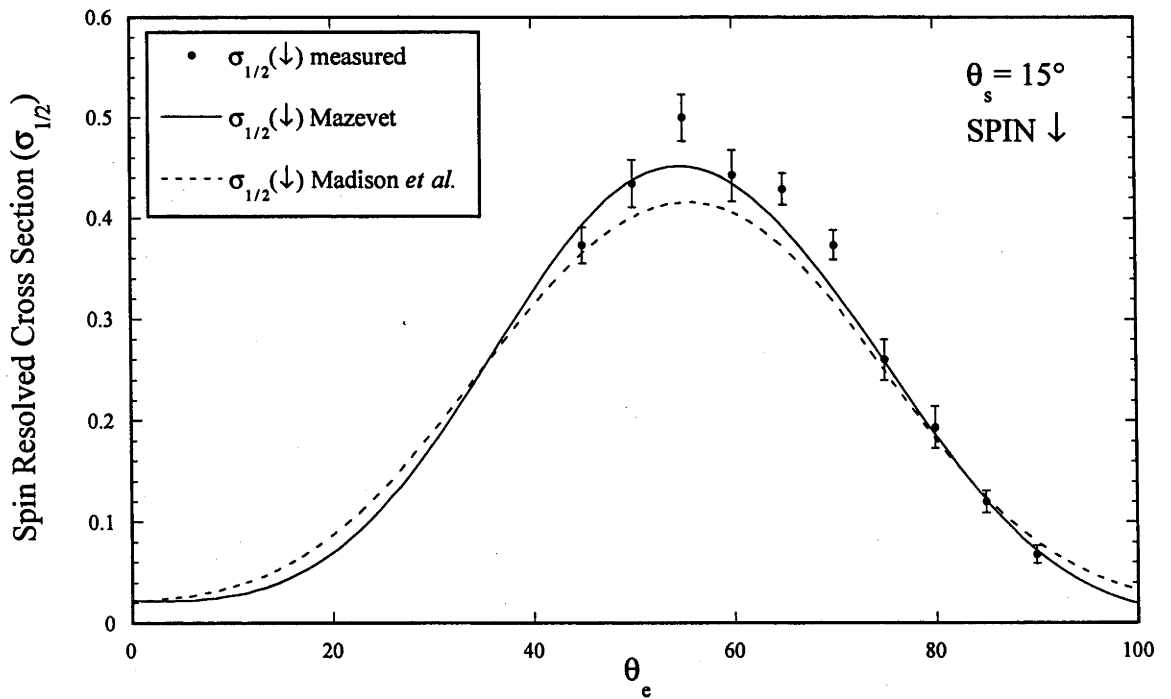
Figure 5.7b: Spin resolved cross sections for the $^2P_{3/2}$ state, compared to the theories of Mazevet (1996) and Madison *et al.* (1996) at $\theta_s = 15°$.

Figure 5.7c: Spin resolved cross sections for the ${}^{2}P_{1/2}$ state, compared to the theories of Mazevet (1996) and Madison *et al.* (1996) at $\theta_s = 28°$.

Figure 5.7d: Spin resolved cross sections for the $^2P_{3/2}$ state, compared to the theories of Mazevet (1996) and Madison *et al.* (1996) at $\theta_s = 28°$.
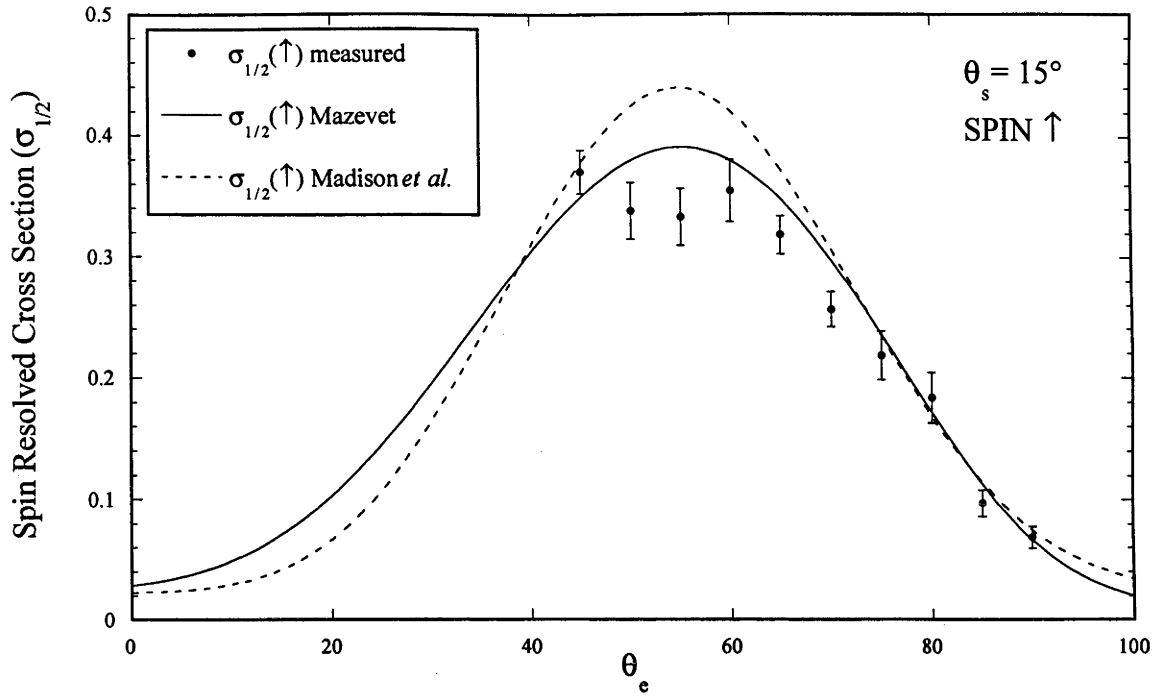
Figure 5.7e: Spin resolved cross sections for the $^2P_{1/2}$ state, compared to the theories of Mazevet (1996) and Madison *et al.* (1996) at $\theta_s = 40°$.
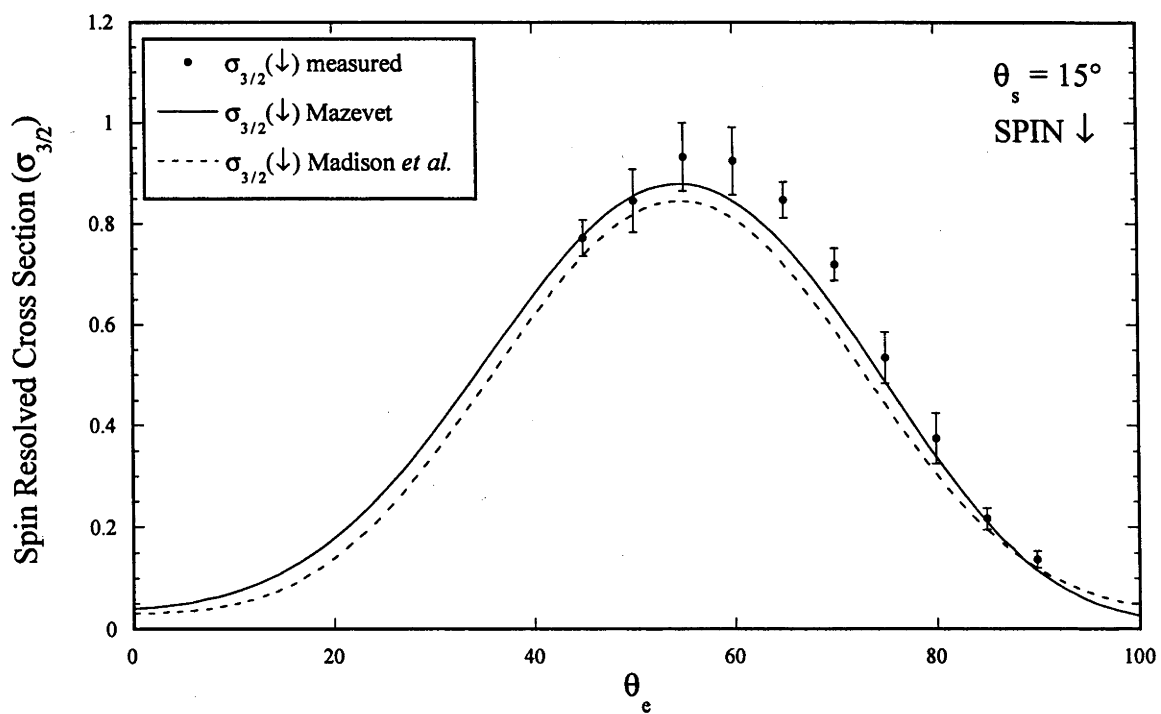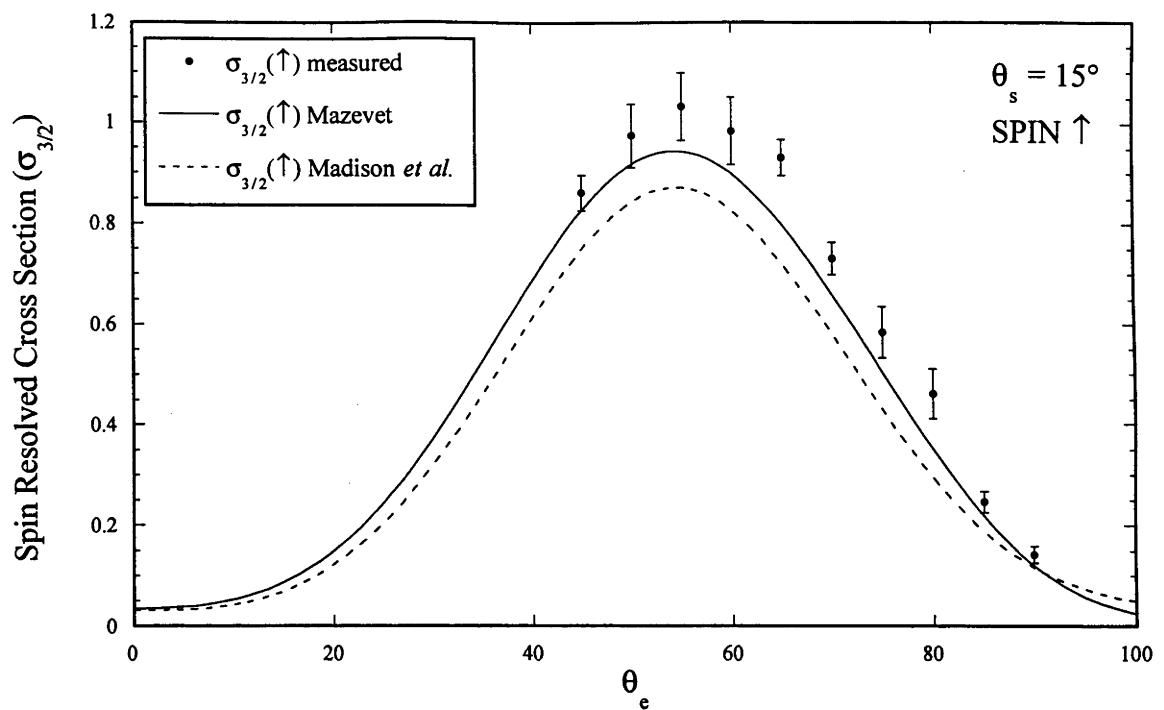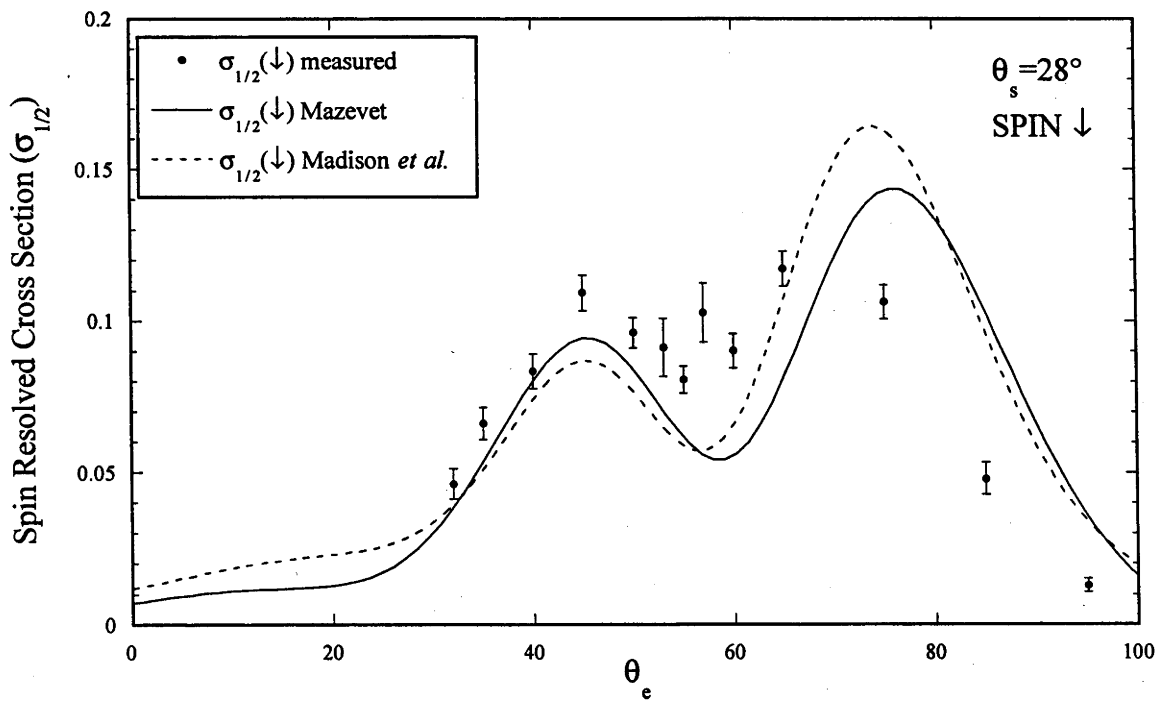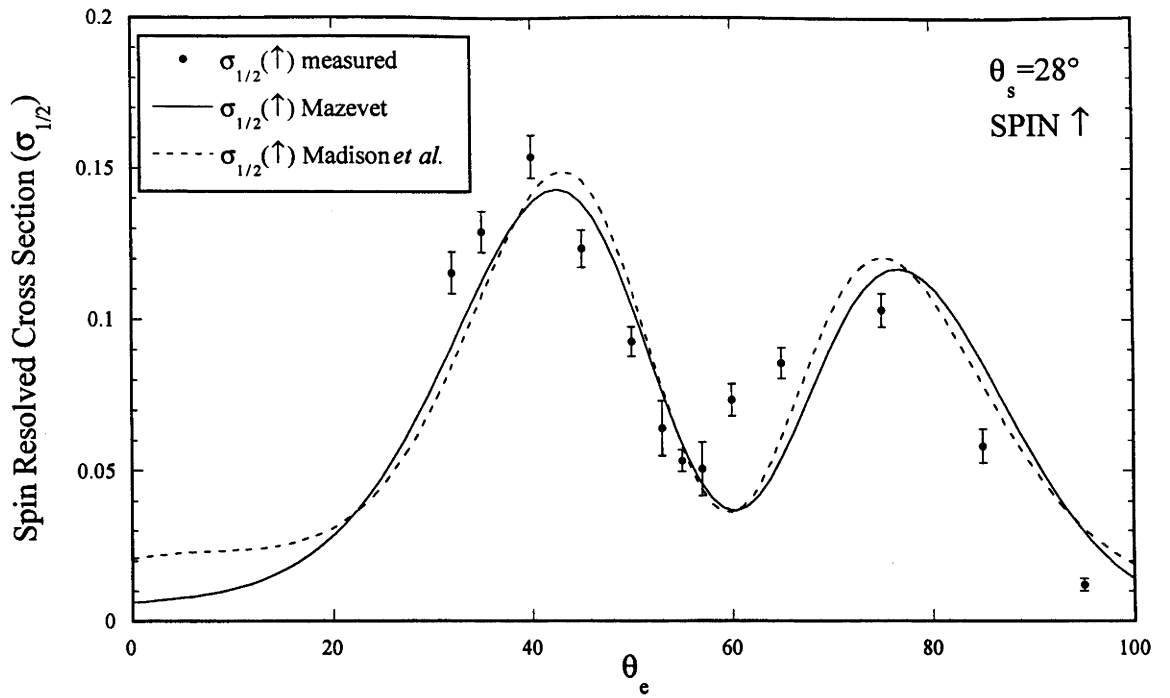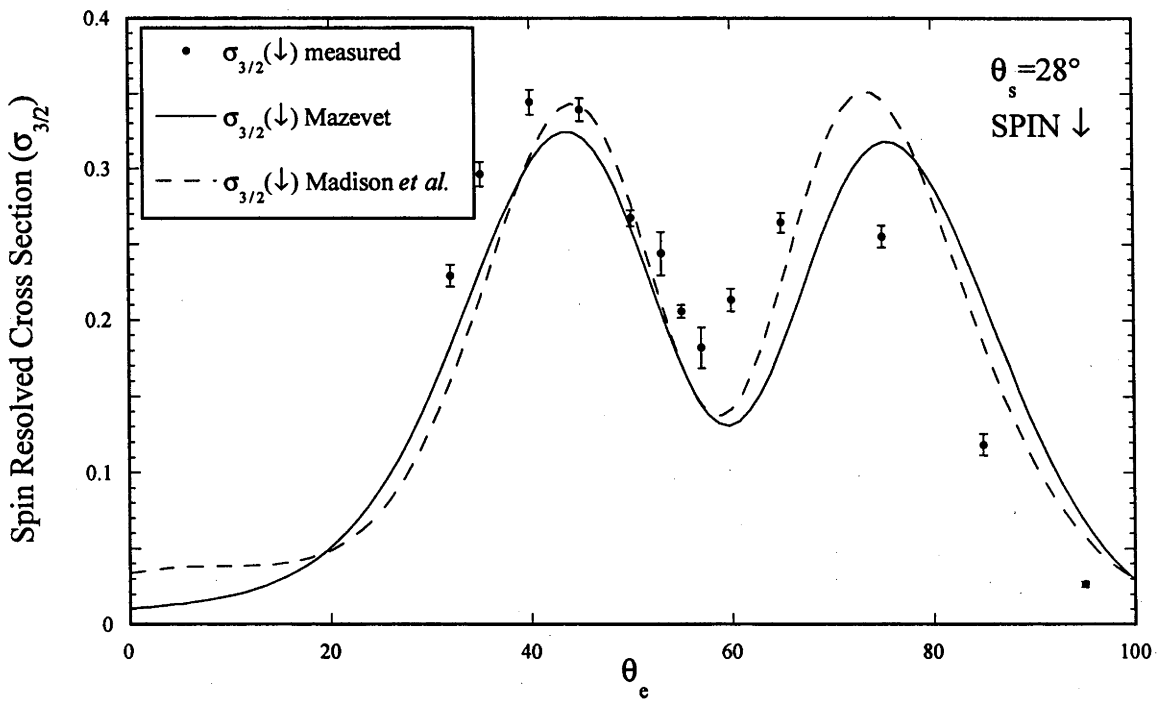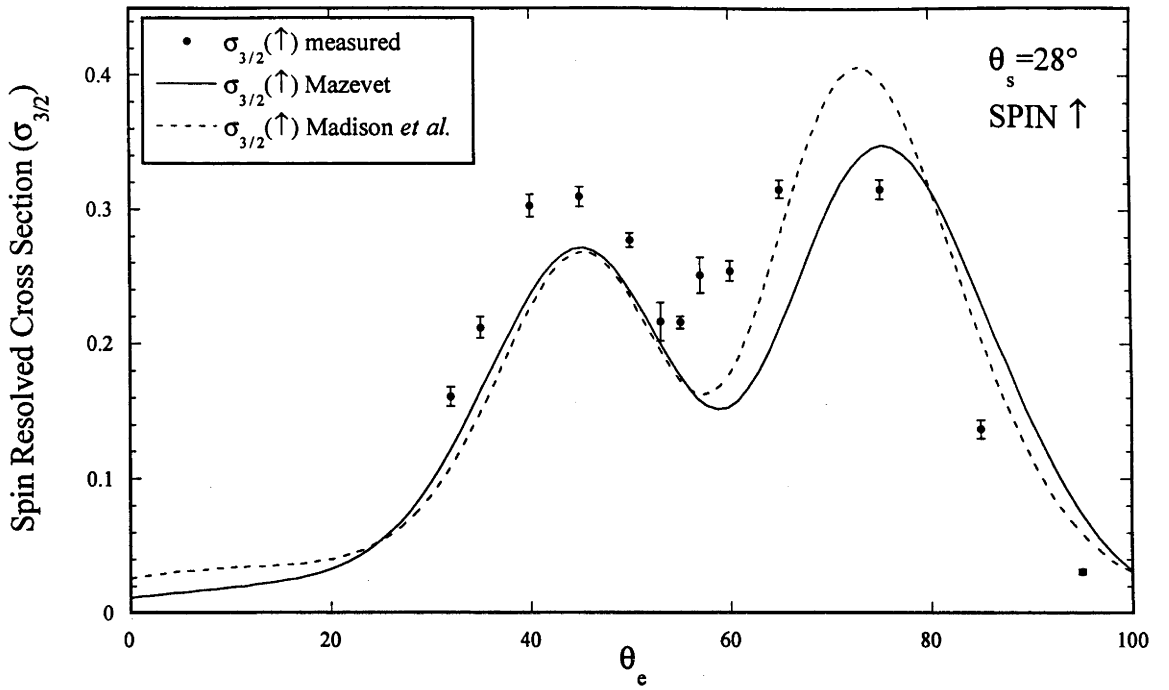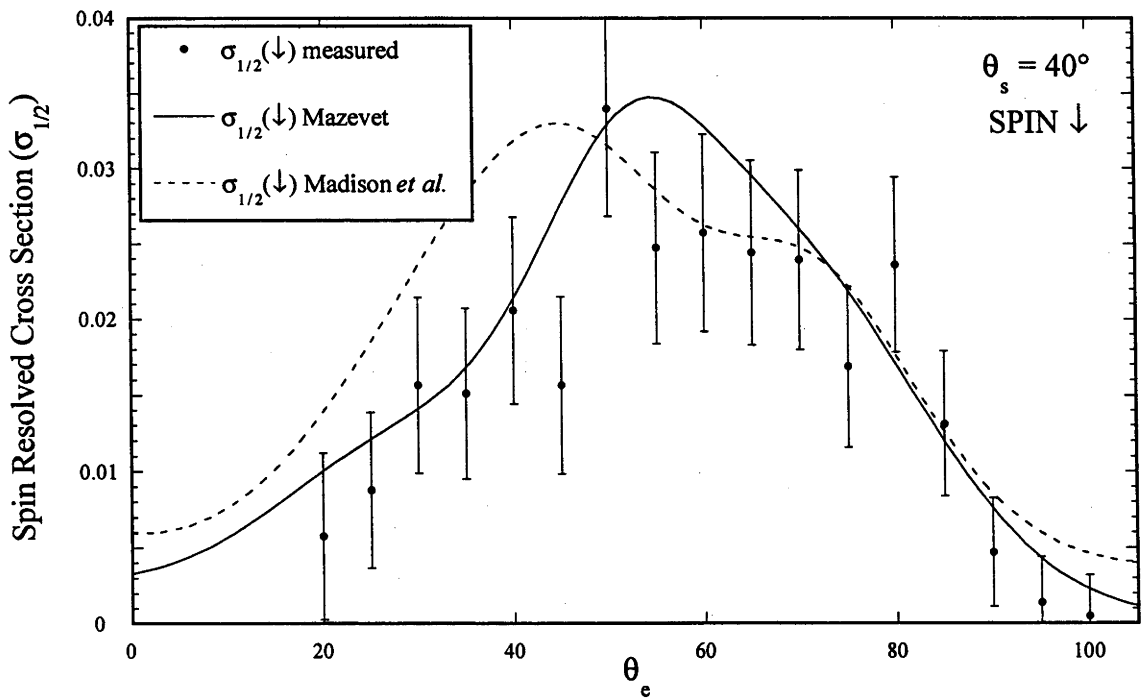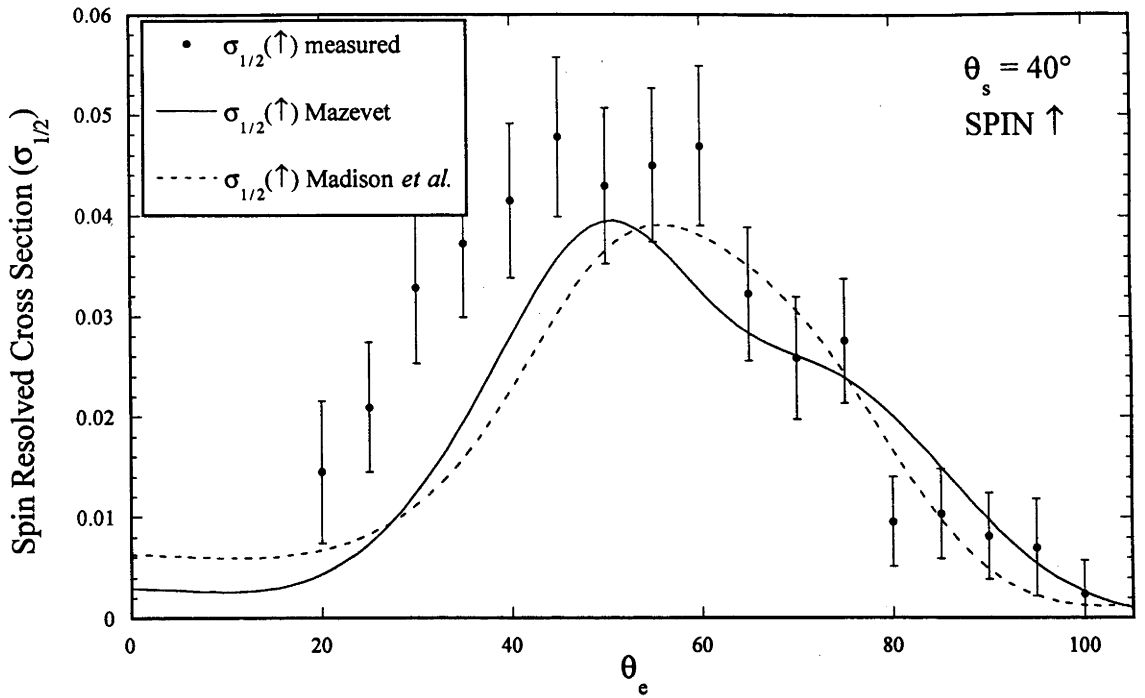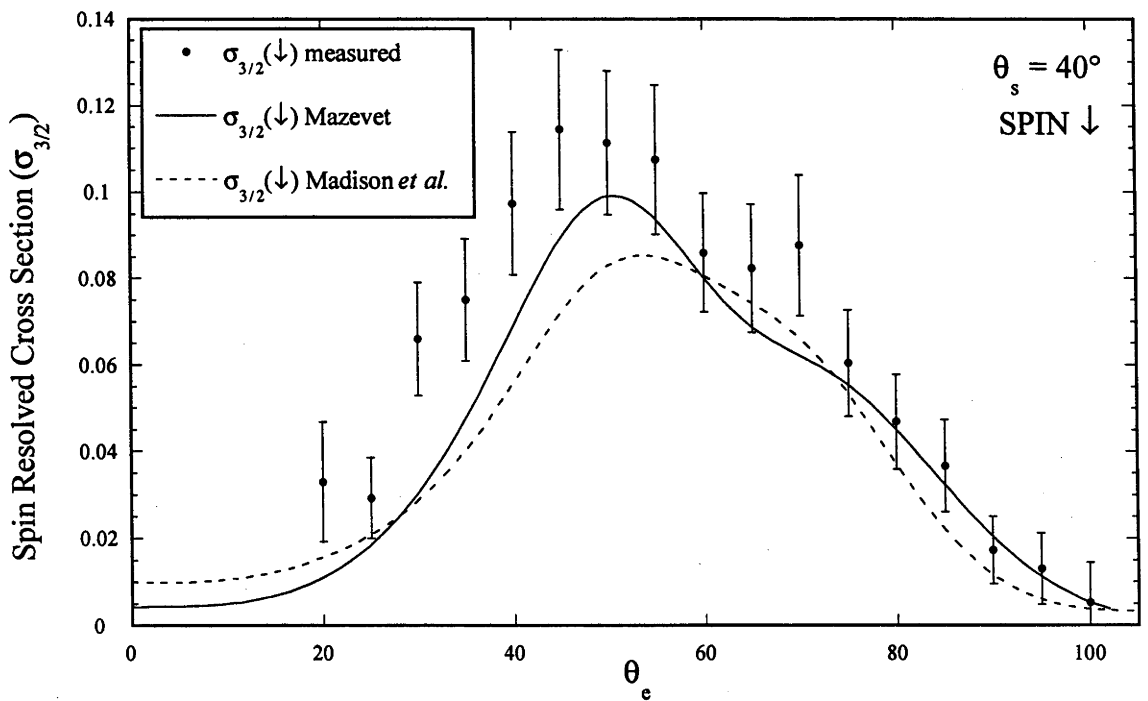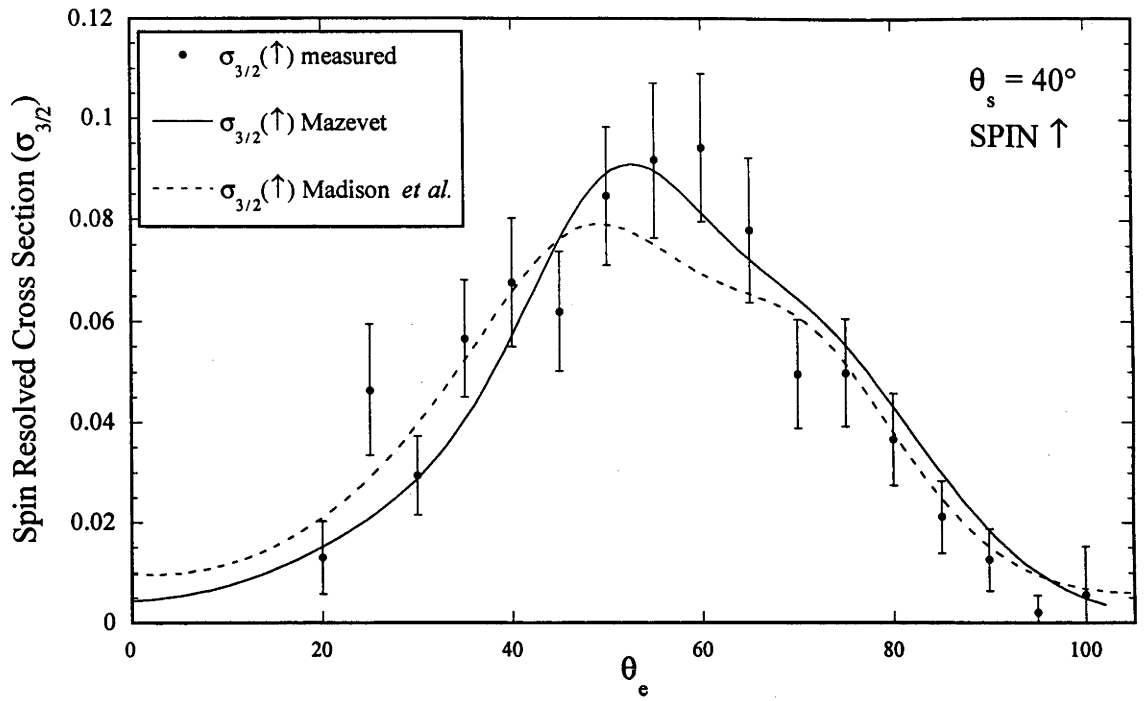
Figure 5.7f: Spin resolved cross sections for the $^2P_{3/2}$ state, compared to the theories of Mazevet (1996) and Madison *et al.* (1996) at $\theta_s = 40°$.

5.5.2 Asymmetry in the Fine-Structure Cross Sections

The $^2P_{1/2}$ state displays an interesting variation in the asymmetry for the three different scattering angles as shown in figures 5.8. The biggest asymmetry is seen at $\theta_s =$ 28°, which shows large, positive asymmetries at the forward ejected electron angles, the largest, 0.43 ± 0.6, being measured at $\theta_e = 32°$. The figure also indicates that the zero in the calculated asymmetry is at $\theta_e = 55°$, (and where the sign of the asymmetry changes), which corresponds to the direction of momentum transfer. The experimental asymmetry zero is at $\theta_e = 50°$, showing the relative angular shift between the theory and the experiment. The theories agree well with each other and give a reasonable description of the data.

As mentioned in section 5.1, the l•s interaction has a negligible effect on the asymmetry parameter (see figure 5.8b). If there were to be a significant difference, it would be expected to be seen at the minima in the cross section, as any such effects would be magnified. However, clearly there is very little difference in the region where the asymmetry parameter is experimentally measured. It appears that both of the theoretical descriptions, which do not include the l•s interaction are satisfactory for this kinematics (at $\theta_s = 28°$).

The experimental asymmetry at $\theta_s = 40°$ displays little agreement with the theoretical calculations. The experimental data has nearly all positive values, except at $\theta_e = 80°$ and $\theta_e = 85°$, where the values are negative. The large errors in this data indicate that more data would be needed to correctly identify the trend. The theories here do not agree in shape or magnitude, although the shape of the calculations with the density matrix formalism of Mazevet (1996), appears to be closer to the experimental data than the calculations of Madison *et al.* (1996).

At $\theta_s = 15°$ where the momentum transfer is small, the theories and the experimental data all agree that there is still a significant, although small, asymmetry evident, which is largest at the forward angles. Both theories predict asymmetries as high as 0.3 at $\theta_e \sim 10°$, but unfortunately, due to the size of the hemispherical analysers, the experiment cannot take measurements in this region. In the region where experimental data is available, the agreement between the theories and the measured results is poor. The DWBA calculation of Madison *et al.* (1996) is consistently higher in magnitude, with a varying shape. Agreement between the asymmetry calculated from the density matrix formalism of Mazevet (1996) and the experimental data is better, although the experimental results show some scatter, whereas the theory is relatively flat between $\theta_e = 45°$ and $\theta_e = 90°$.

For the $^2P_{3/2}$ state, figures 5.9, the general trends are the same as for the $^2P_{1/2}$ state. That is, the asymmetry at $\theta_s = 15°$ is very small, except for the forward angles, where an asymmetry as high as -0.15 is predicted by the density matrix formalism of Mazevet (1996). It is this density matrix formalism calculation which is in better agreement with the experimental results, as it is almost constant about 0.025, while the calculations of Madison *et al.* (1996) is much smaller and becomes negative at $\theta_e \sim 65°$. The largest discrepancy is at $\theta_e = 80°$, which shows an experimental value three times

larger than the theory of Mazevet (1996). It is here where the cross section becomes smaller, which is reflected in the size of the errors.

Again the $\theta_s = 28°$ data is the most varied, while showing smaller asymmetry values than the $^2P_{1/2}$ state. In fact, at most ejected electron angles, the measured asymmetry for the $^2P_{1/2}$ state is approximately twice the magnitude, but opposite in sign to the measured asymmetry values of the $^2P_{3/2}$ state. This is to be expected from equation 5.15, in the limiting case of the non-relativistic fine-structure effect. The largest value here is only -0.17 ± 0.04, at the same angle ($\theta_e = 32°$) of the largest asymmetry (0.43 ± 0.06) for the $^2P_{1/2}$ state. While at $\theta_s = 40°$, the agreement with the theories and between the theories and experiment is again poor, although the theory of Mazevet (1996) fares best with regard to the measured asymmetries.

To demonstrate that the asymmetries in both the fine-structure states, $^2P_{1/2}$ and $^2P_{3/2}$, arise from the fine-structure effect, the quantity $(A_{1/2} + 2A_{3/2})/3$, (as per equation 5.16), is plotted. These are shown in figures 5.10. It is clear that for both $\theta_s = 15°$ and $\theta_s = 28°$, the experimental data is consistently zero, within the errors.

The $\theta_s = 28°$ measured data shows some evidence for a small non-zero asymmetry contribution at the larger ejected electron angles. This slight variation from zero, may indicate that it is not a pure fine-structure effect which is responsible for the asymmetries. The theories both show an essentially zero distribution for this quantity, showing that relativistic effects are small.

The greatest deviation from zero is at $\theta_s = 40°$, but this is most likely be due to the poor statistics available at $\theta_s = 40°$. Where the statistics are better, between $\theta_e = 35°$ and $\theta_e = 75°$ this parameter is indeed close to zero. This region also corresponds to the larger cross section at this setting.

Overall, this averaged asymmetry parameter, which is approximately zero for each kinematic considered here, confirms the presence of the fine-structure effect in xenon. That is, for each fine-structure state there is a non-zero asymmetry parameter, but when the fine-structure is not resolved, *i.e.* figures 5.10, there is essentially no observed spin dependence. It can be seen, especially from the $\theta_s = 40°$, that the semi-relativistic DWBA calculation of Mazevet (1996), which includes the exchange between the continuum electrons and the ion, is a better description of the asymmetry parameter. Further, it can be seen from the asymmetry for ionisation to the $^2P_{1/2}$ fine-structure state at $\theta_s = 28°$, that the spin-orbit interaction is not important in the region where the experimental data was measured.
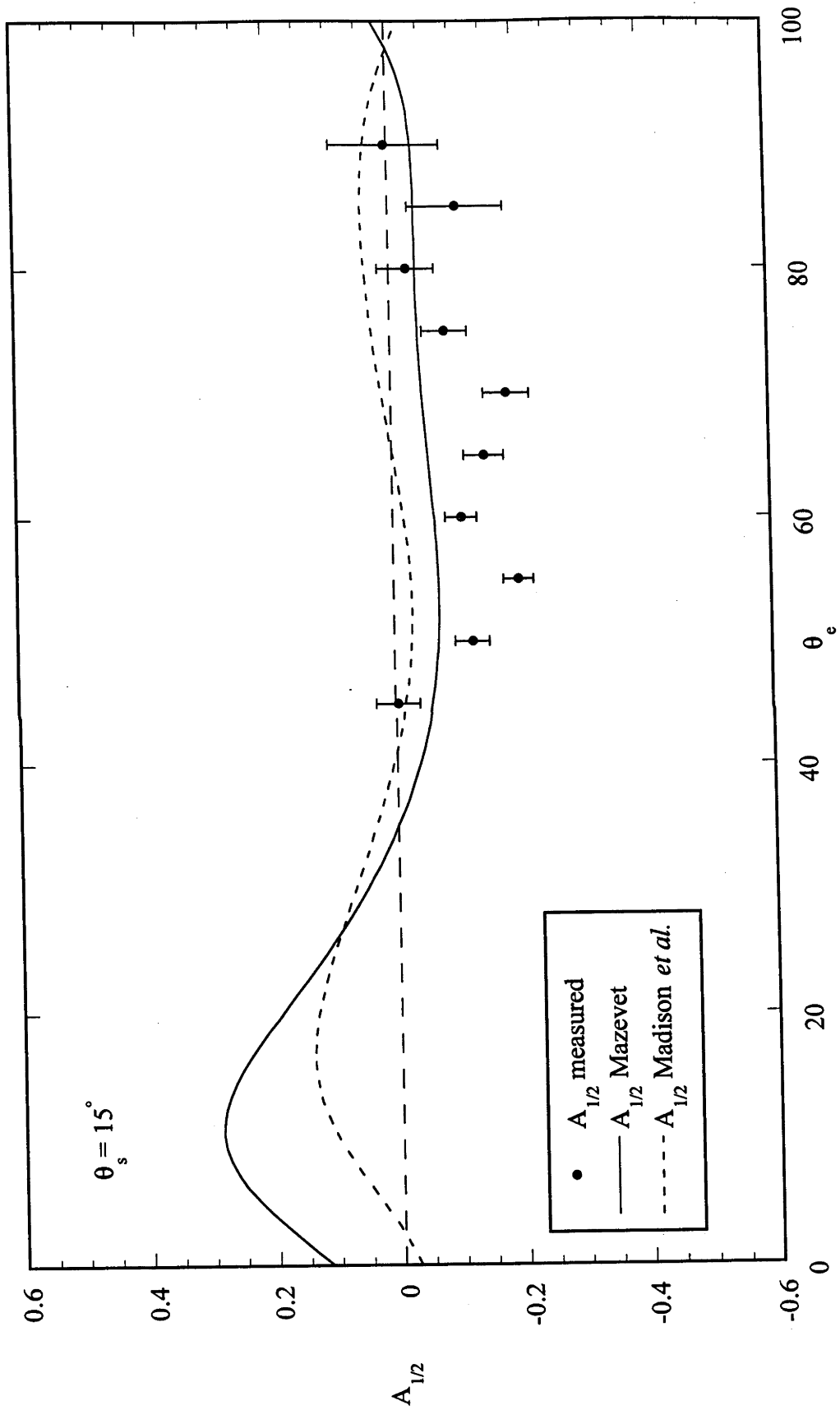
Figure 5.8a: Asymmetry for $^2P_{1/2}$ compared to the theories of Mazevet (1996) and Madison *et al.* (1996).
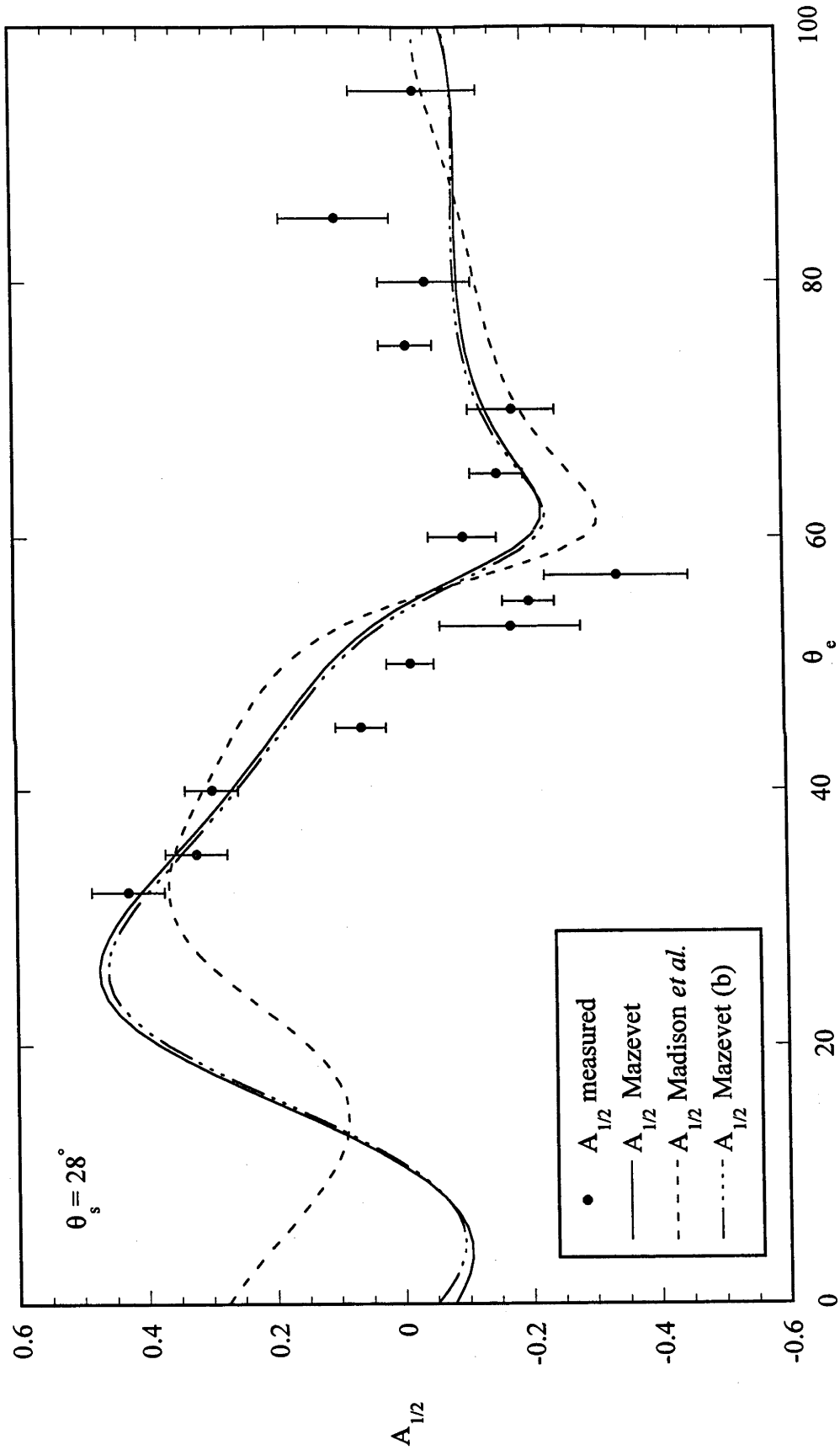
Figure 5.8b: Asymmetry for $^2P_{1/2}$ compared to the theories of Mazevet (1996) and Madison *et al.* (1996). Here an example of a calculation with the **l•s** interaction is given (Mazevet (b)). See text for details.
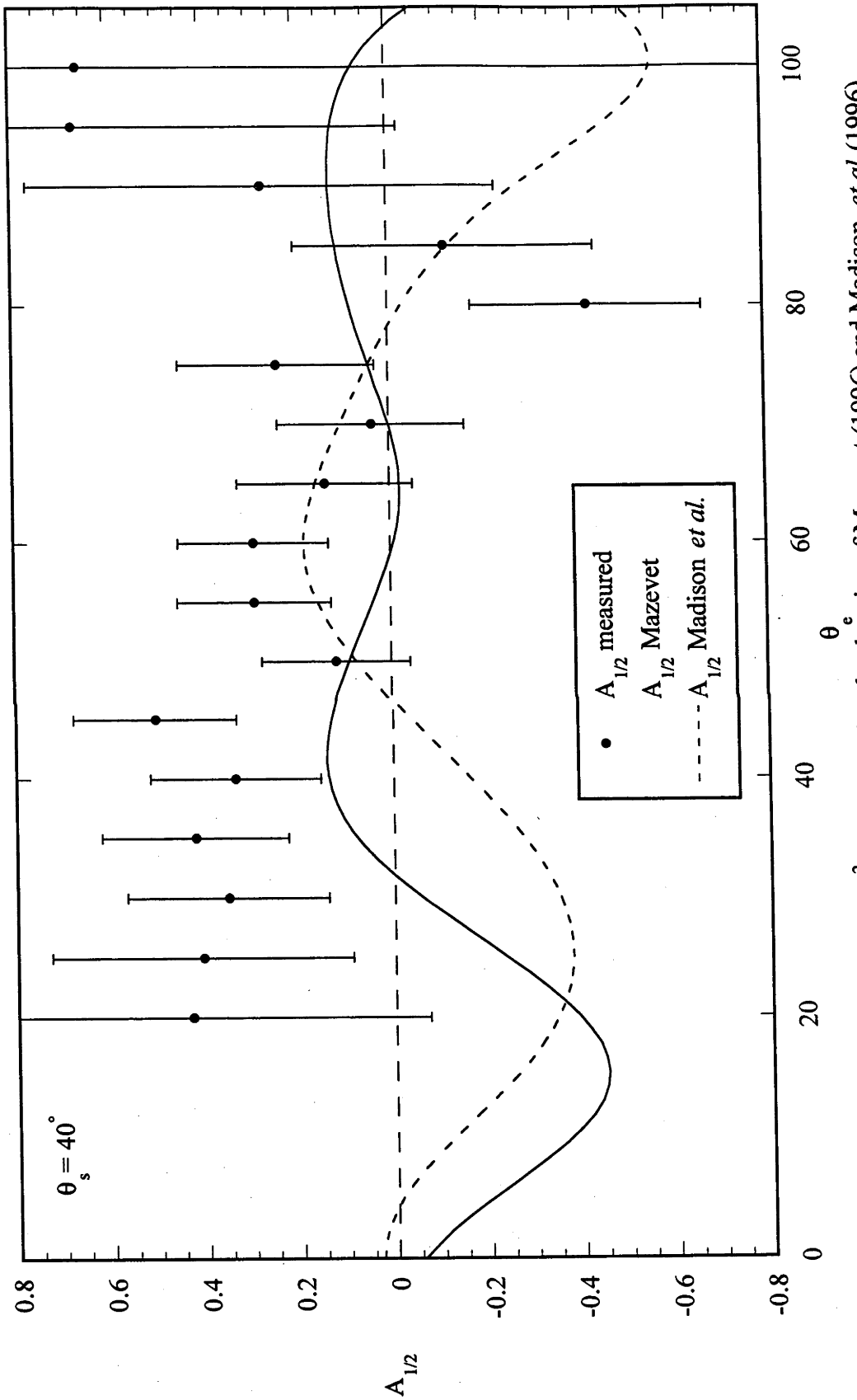
Figure 5.8c: Asymmetry for $^2P_{1/2}$ compared to the theories of Mazevet (1996) and Madison *et al.* (1996).
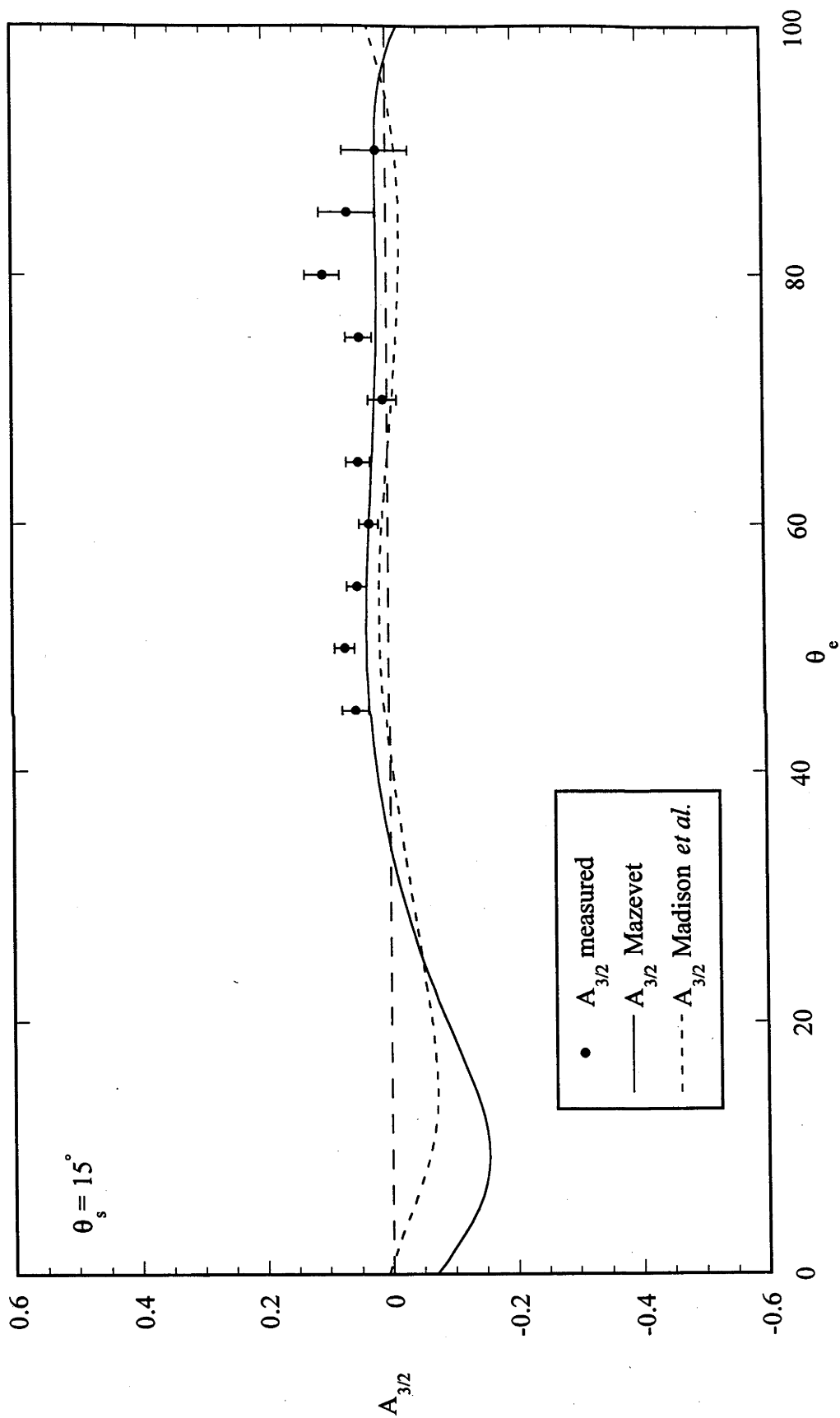
Figure 5.9a: Asymmetry for $^2P_{3/2}$ compared to the theories of Mazevet (1996) and Madison *et al.*(1996).

Figure 5.9b: Asymmetry for $^2P_{3/2}$ compared to the theories of Mazevet (1996) and Madison *et al.* (1996).

Figure 5.9c: Asymmetry for $^2P_{3/2}$ compared to the theories of Mazevet (1996) and Madison *et al.* (1996).

Figure 5.10a: Averaged asymmetry compared to the theories of Mazevet (1996) and Madison *et al.* (1996).

Figure 5.10b: Averaged asymmetry compared to the theories of Mazevet (1996) and Madison *et al.*(1996).

Figure 5.10c: Averaged asymmetry compared to the theories of Mazevet (1996) and Madison *et al.* (1996).

5.5.3 Branching Ratios

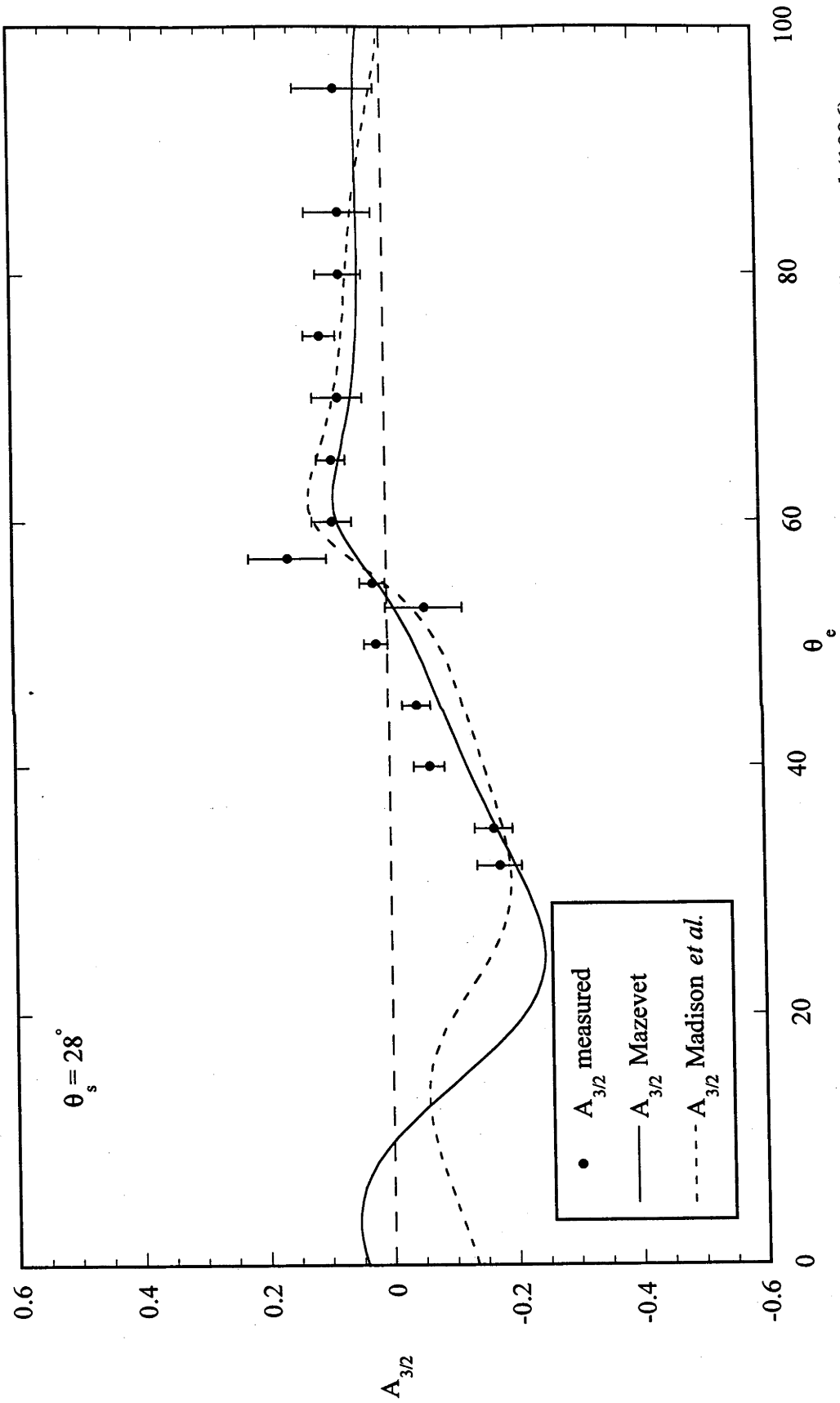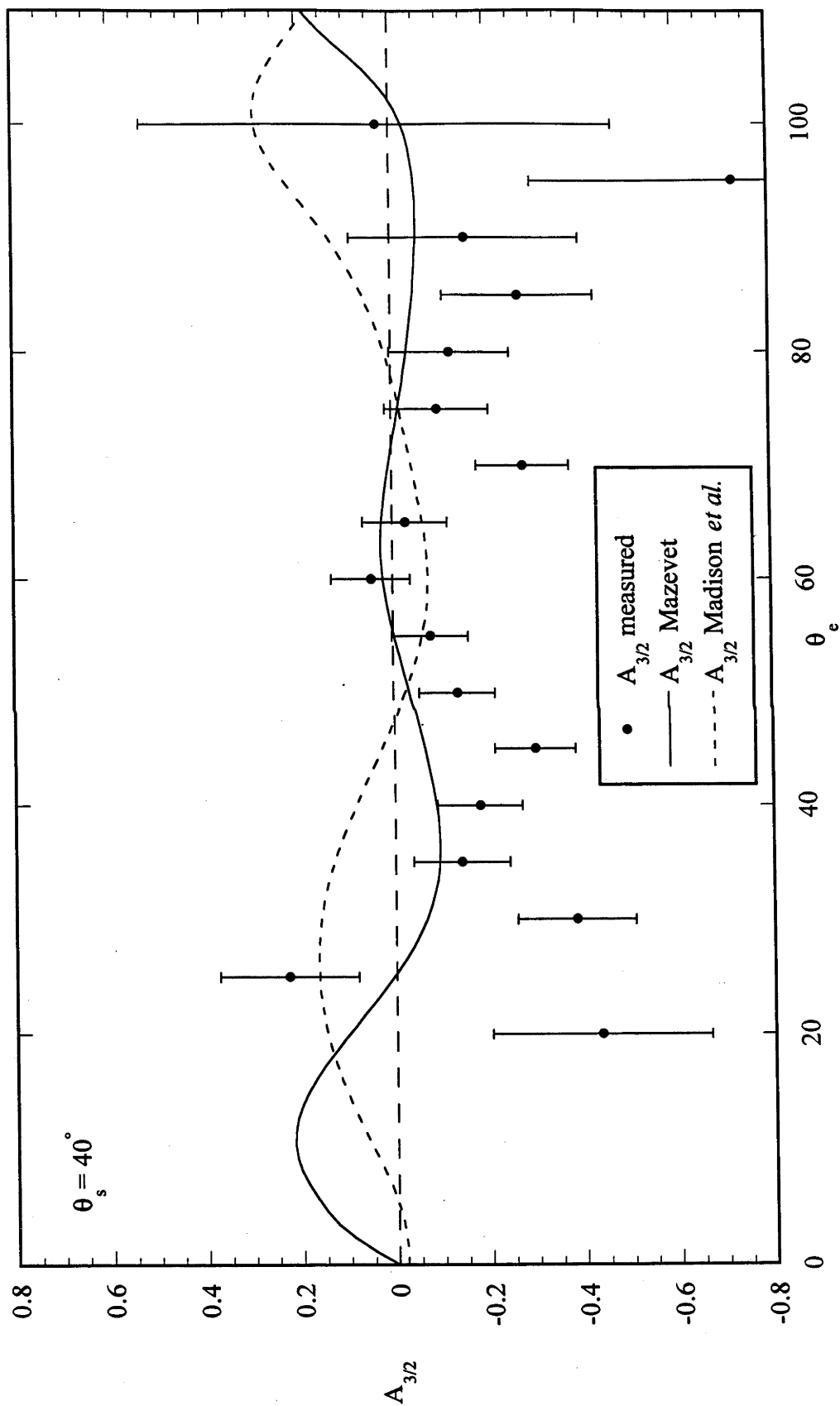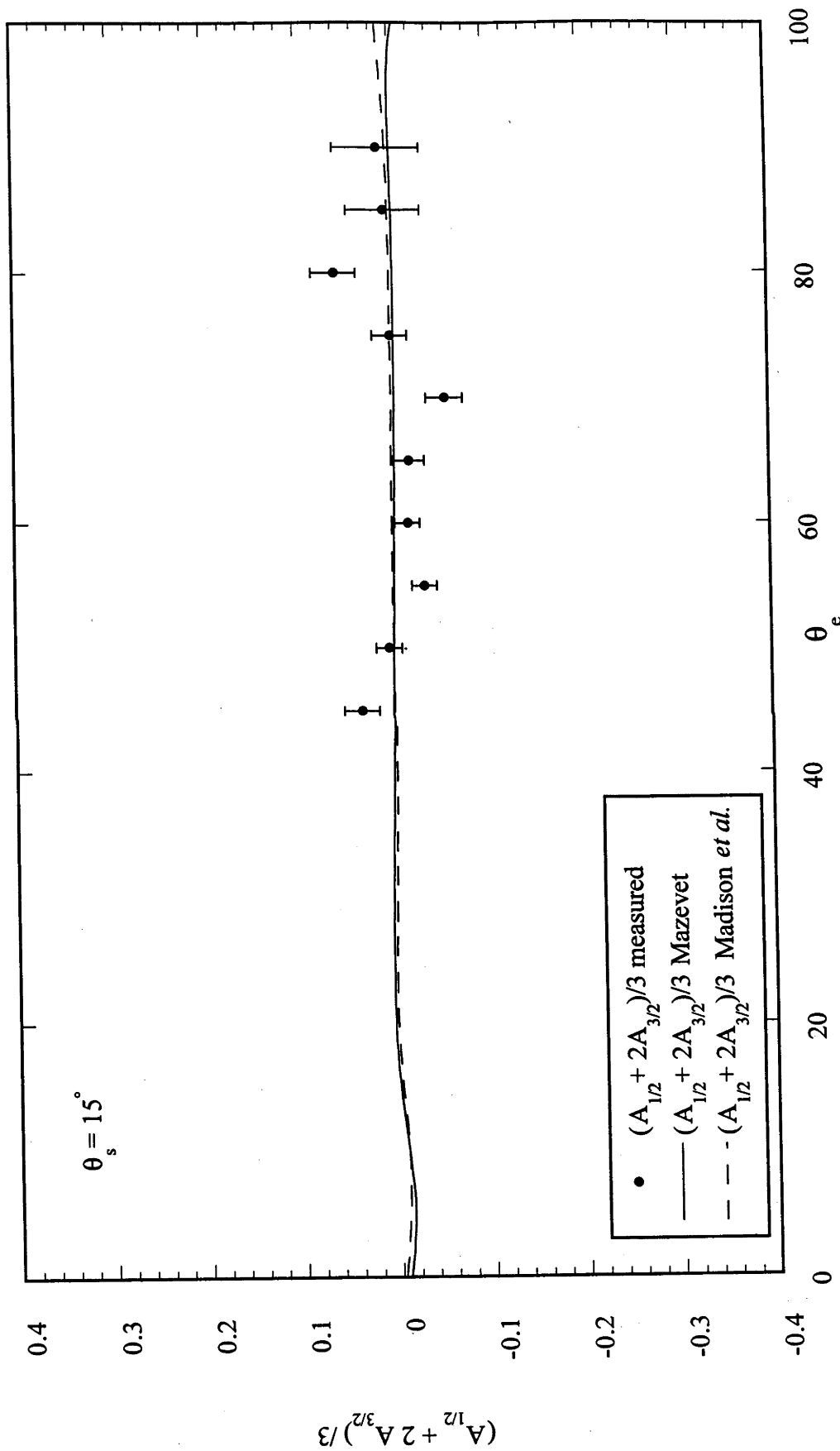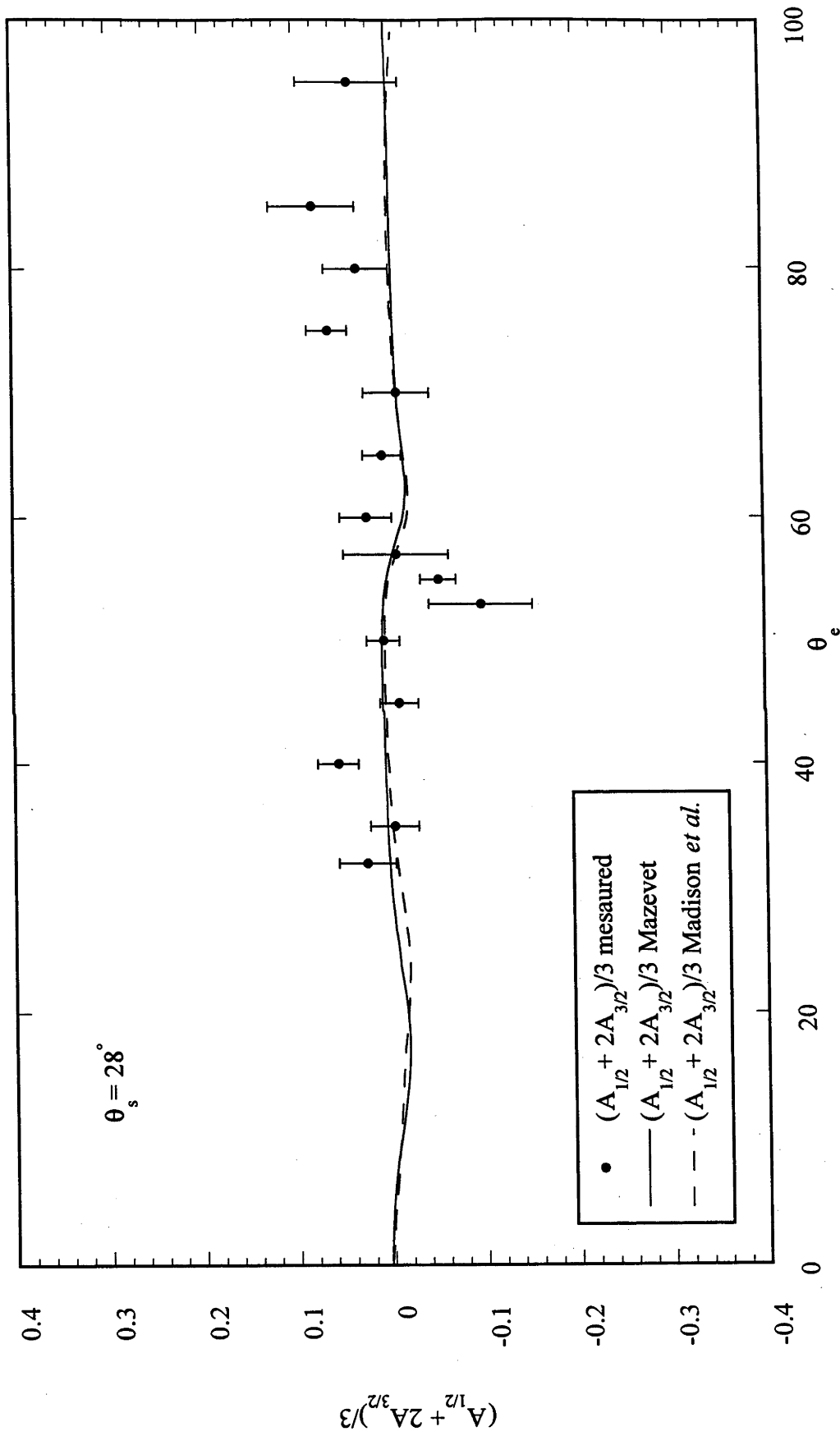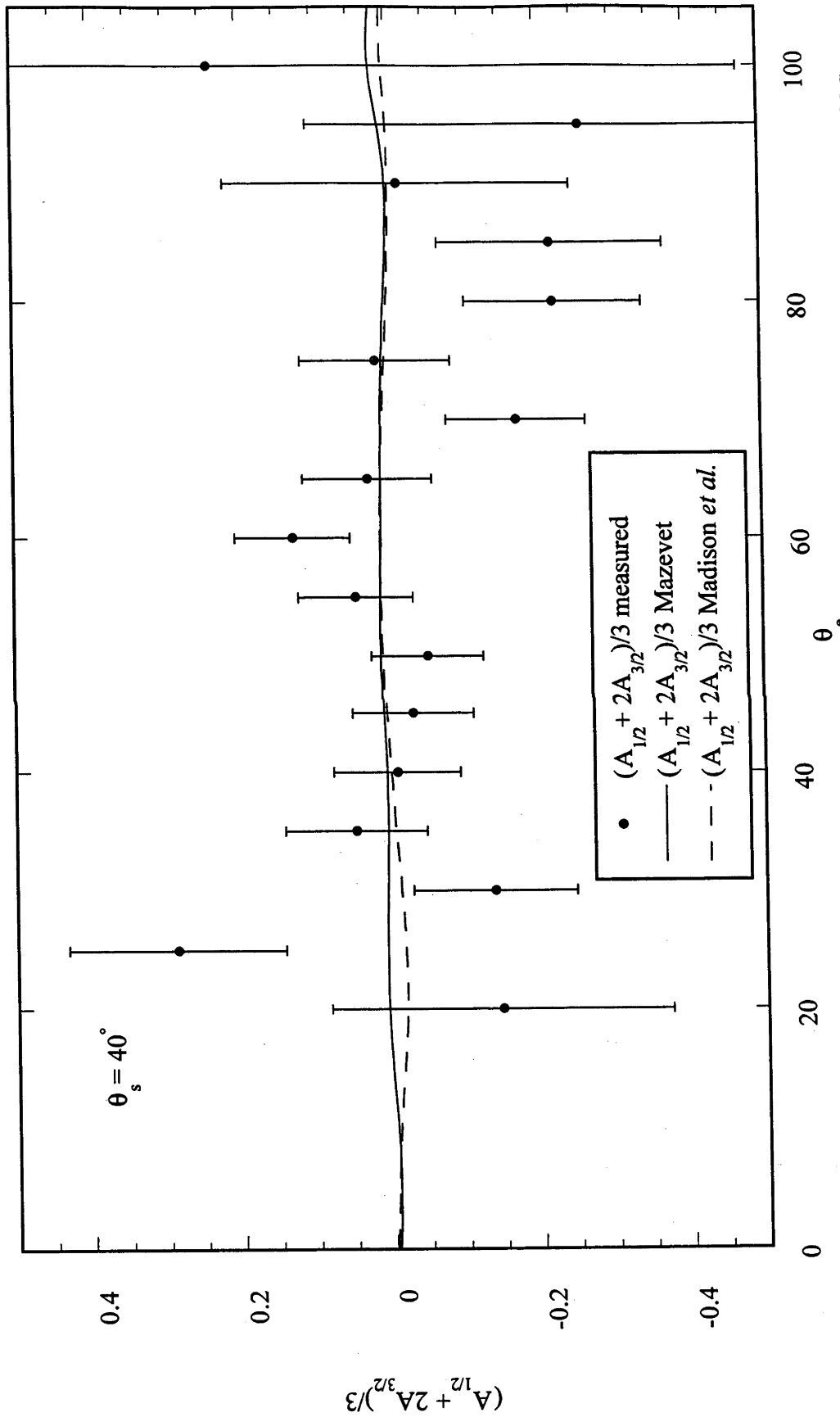The branching ratios depend on the relative areas of the $^2P_{1/2}$ and $^2P_{3/2}$ peaks and it would be expected that the statistical branching ratio would be 2, due to the statistical weighting of the $^2P_{1/2}$ and $^2P_{3/2}$ states. The branching ratios shown are labelled with respect to the direction of the incident polarised electron beam, perpendicular to the scattering plane, either spin up (denoted spin ↑, in figures 5.11) or spin down (denoted spin ↓, in figures 5.12).

Experimental data for $\theta_s = 15°$ (spin up), shows a branching ratio as high as 3.1 ± 0.1 at $\theta_e = 55°$ and is consistently greater than 2. The theory of Mazevet predicts a minima of about 1.4 at $\theta_e = 10°$ and is 2 at $\theta_e = 32°$ but is never greater than 2.5. The calculation of Madison *et al.* (1996) is similar in shape to the other theory, but is smaller in magnitude. This result is a reflection of the underestimation of the $^2P_{3/2}$ state contribution in the cross section calculations of the theories as mentioned earlier.

The $\theta_s = 28°$ (spin up) data, (figure 5.11b) shows significant structure. It peaks at $\theta_e = 55°$, with a value of 5.0 ± 0.9 (note that the error bars are larger in this region, which corresponds to the smallest cross section for $\theta_s = 28°$). There is an angular shift of approximately 5° between the experimental data and the theoretical calculations. In this case, the theory of Madison *et al.* (1996) is larger in magnitude than the theory of Mazevet (1996) but the shapes of the theories are very similar.

The general trend agreement of the theoretical calculation of Mazevet (1996) at $\theta_s = 40°$ (spin down), is quite good (figure 5.11c). The theory of Madison *et al.* (1996) does not agree well with the experimental branching ratio, especially at forward and backward angles. In the region of $\theta_e = 50°$ to $\theta_e = 75°$, the values are close to 2, however, the theory of Mazevet (1996) predicts values to be slightly higher than 2, while the theory of Madison *et al.* (1996) predicts values slightly less than 2.

The spin down data is in reasonable agreement with the theoretical calculations in most of the three cases (figures 5.12). The first case, $\theta_s = 15°$, shows excellent agreement, with the values being consistently around 2, within experimental error. Again, the theoretical calculation of Mazevet (1996) predicts higher values than the measured branching ratio (spin down), while the theory of Madison *et al.* (1996) predicts slightly lower values than the measured values, although both calculations are in quite good agreement with the experimental data..

There is more structure to the $\theta_s = 28°$ data. However, the ratios at the backward angles are flat at about 2.5. At the forward angles the branching ratio increases to a maximum value, 5.0 ± 0.5 at $\theta_e = 32°$. The semi-relativistic calculation, which includes the exchange interaction between the continuum electrons and the ion (Mazevet, 1996) is in much better agreement with the experimentally measured branching ratio (spin down), than the theory of Madison *et al.* (1996). In this case, the prediction of Madison *et al.* (1996) is lower than the measured values, which is converse to the spin up case, where it was larger than the measured values.

As the cross section is smaller for the $^2P_{1/2}$ state, by definition of the branching ratio, $(\sigma_{3/2} / \sigma_{1/2})$ it is not surprising that the agreement at $\theta_s = 40°$ is not good and the errors are very large. The shape, however, does agree with the theory of Mazevet, although the measurements give a uniformly higher magnitude. The theory of Madison *et al.* (1996) appears not to agree with the experimental data at all, except between $\theta_e = 50°$ and $\theta_e = 80°$, however this is a peak for the theoretical predictions, but a trough for the measured branching ratio.

An unpolarised branching ratio plot shows how the data would look if the experiment did not use a polarised electron beam. In this case the incident polarisation is averaged over. These results are shown in figures 5.13. Both theories underestimate the unpolarised branching ratios at $\theta_s = 15°$, although the data agrees in shape. This is consistent with the poor agreement for the spin up data at the same setting. The theory of Madison *et al.* (1996) is consistently lower than the theory of Mazevet (1996), although both agree in shape.

At $\theta_s = 28°$ the agreement between the theories and the experimental data is good, although there is again evidence of the angular shift between the experimental data and the theoretical calculations. The theoretical calculations begin to differ at the forward angles, where the theory of Madison *et al.* (1996) predicts a minima at $\theta_e = 18°$, which is not evident in the theory of Mazevet (1996). Unfortunately, the experimental apparatus is unable to take measurements in this region, or at the backward angles, which is again where the theories differ. This graph, figure 5.13b, also includes another calculation of Mazevet (1996), which is labelled as Mazevet (b). This calculation uses a Hartree-Fock wave function for the target states. The calculation with the Hartree-Fock description (a non-relativistic description) shows an almost constant value of 2, except where the cross section has a minimum. It is clear then, that a relativistic calculation is required and that the branching ratio depends sensitively on the description of the target state.

The $\theta_s = 40°$ (figure 5.13c) experimental data are rather scattered, which is a reflection of both spin dependent branching ratios and the low cross section for this kinematics. The unpolarised branching ratio of 3.85 ± 1.8 at $\theta_e = 100°$ is certainly due to the extremely low cross section and hence the difficulty in distinguishing between the $^2P_{1/2}$ and $^2P_{3/2}$ peaks in that energy spectrum. The semi-relativistic calculation of Mazevet (1996) agrees well with the experimental data, but the theory of Madison *et al.* (1996) underestimates the experimental data, except for $\theta_e = 30°$ and $\theta_e = 95°$.

Mazevet (1996) and Madison *et al.* (1996) both use the Dirac-Fock wave function to describe the xenon target, yet the calculations are consistently different. Therefore, these experiments give information on the reaction dynamics as well as the structure of the target. The sensitivity to the target wave function is clearly demonstrated in figure 5.13b. It is essential that Dirac-Fock wave functions be used.
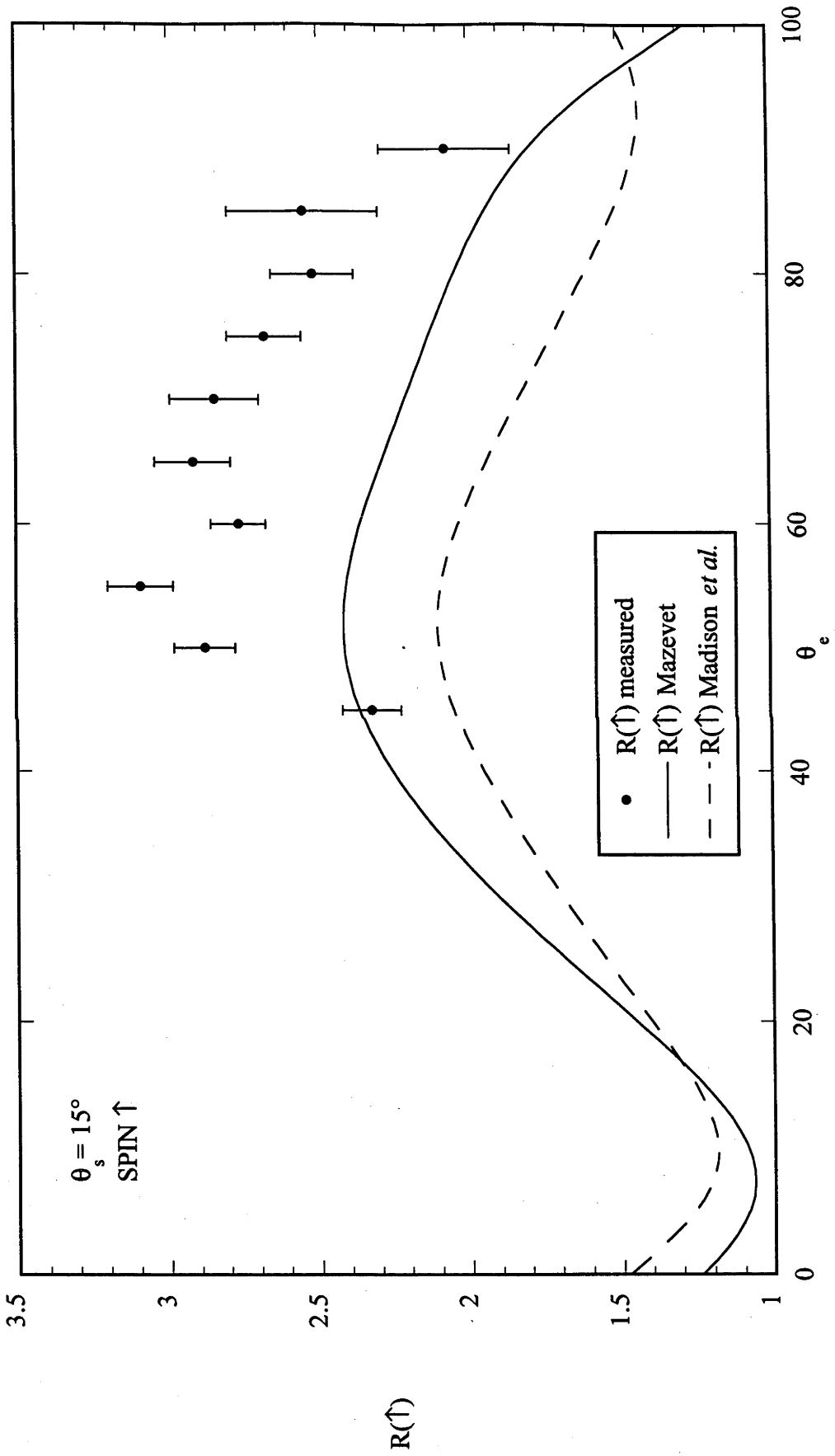
Figure 5.11a: Branching ratios for spin up incident electrons compared to the theories of Mazevet (1996) and Madison *et al.* (1996).
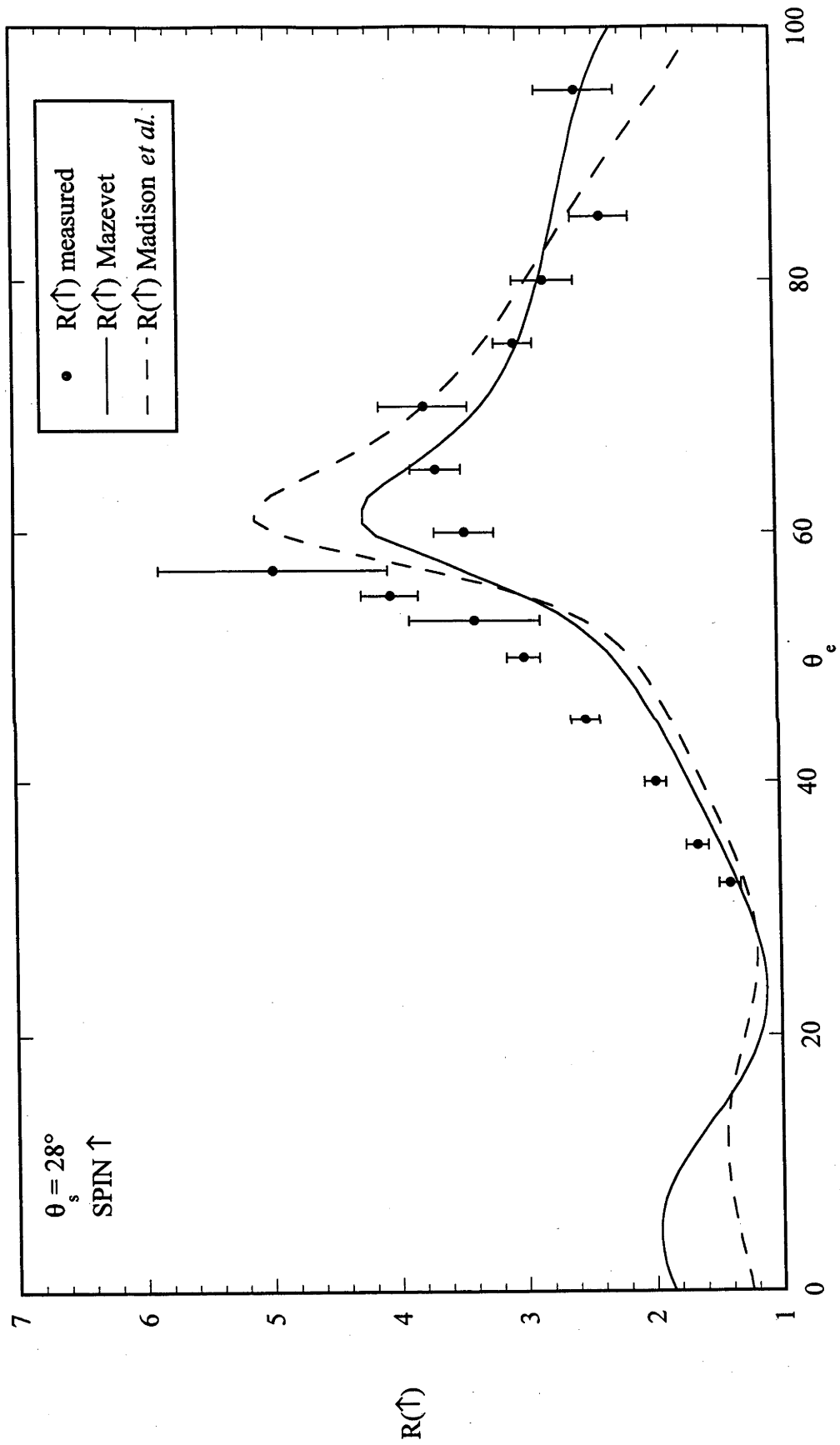
Figure 5.11b: Branching ratios for spin up incident electrons compared to the theories of Mazevet (1996) and Madison *et al.*(1996).
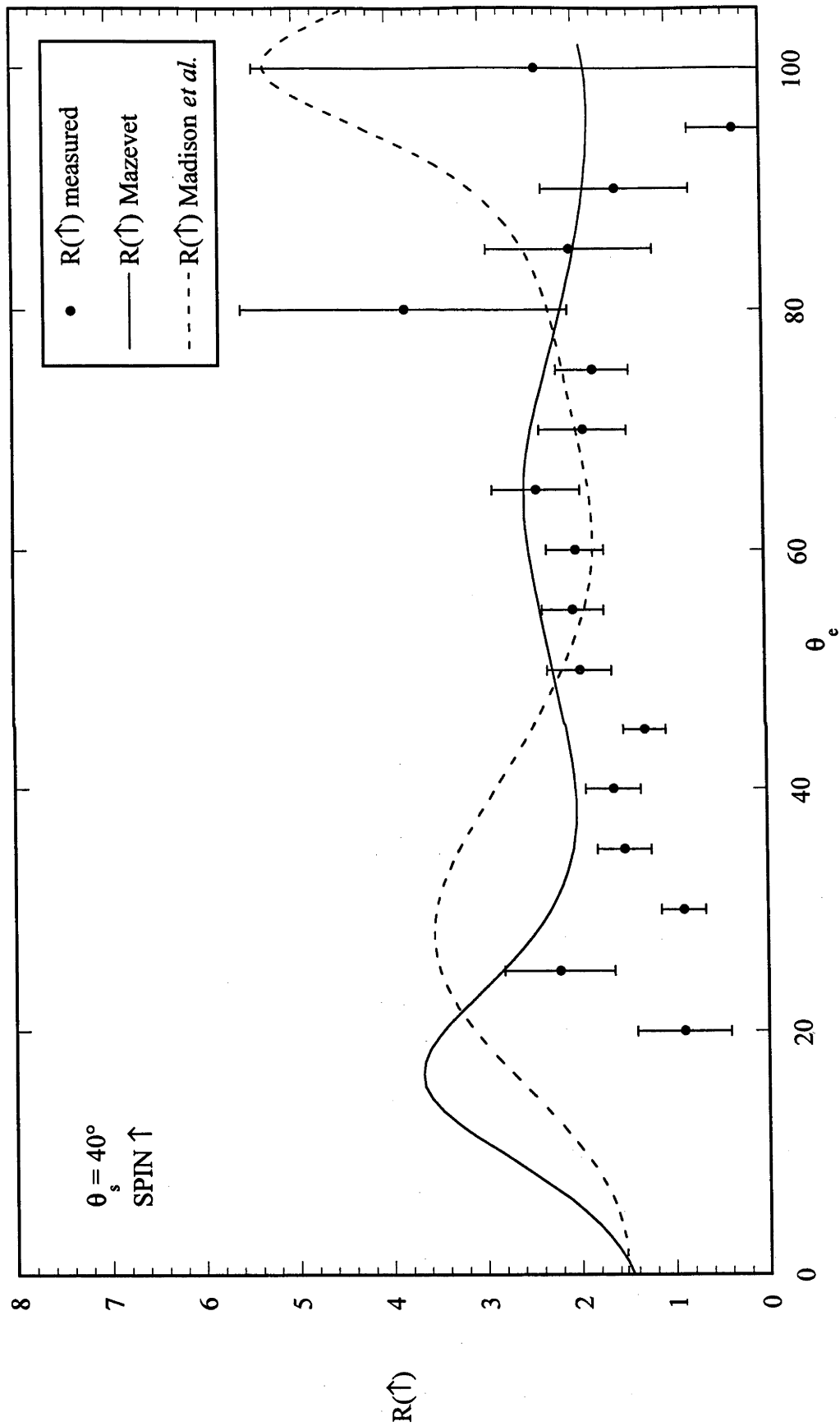
Figure 5.11c: Branching ratios for spin up incident electrons compared to the theories of Mazevet (1996) and Madison *et al.*(1996).
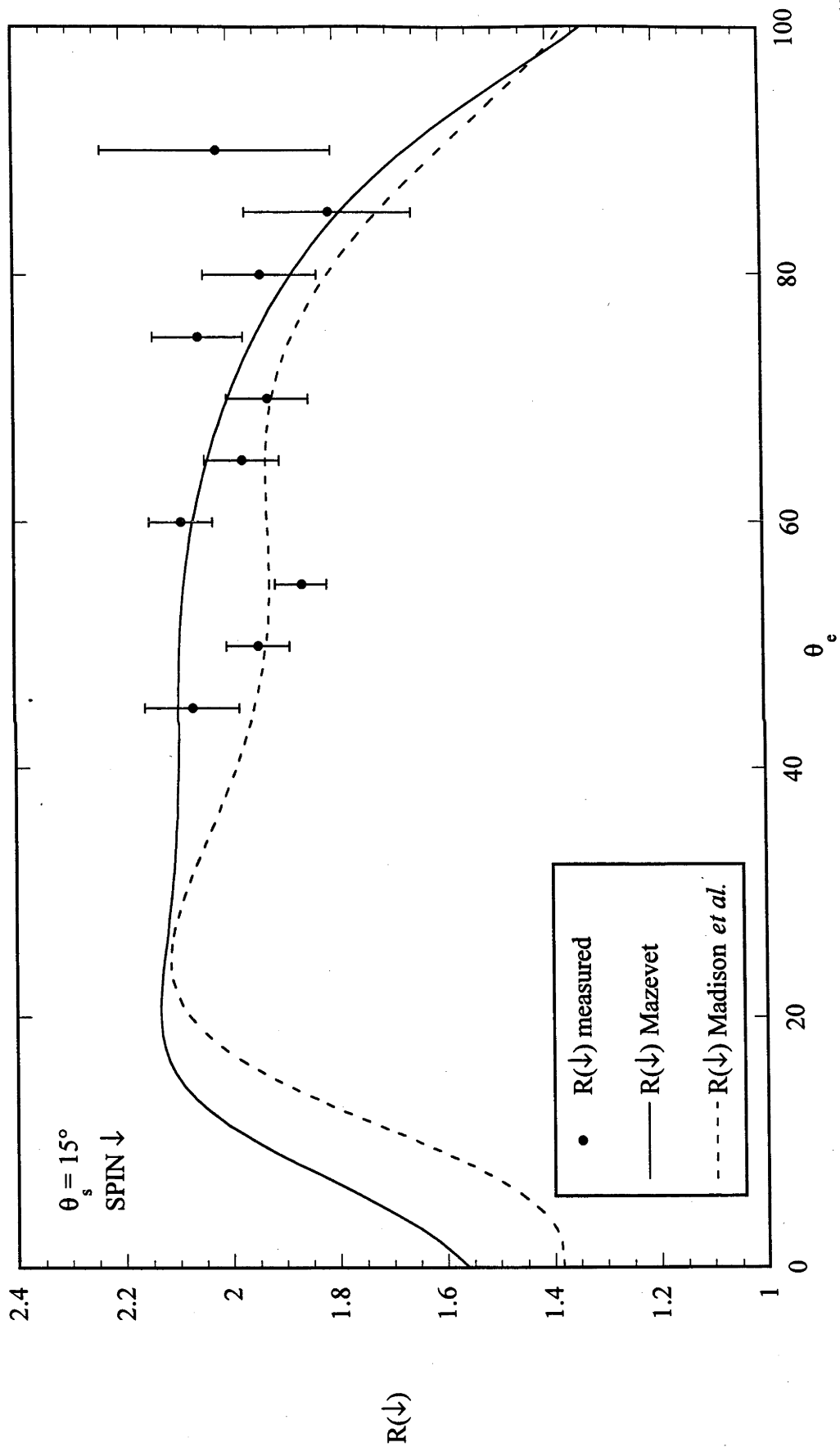
Figure 5.12a: Branching ratios for spin down incident electrons compared to the theories of Mazevet (1996) and Madison *et al.* (1996).
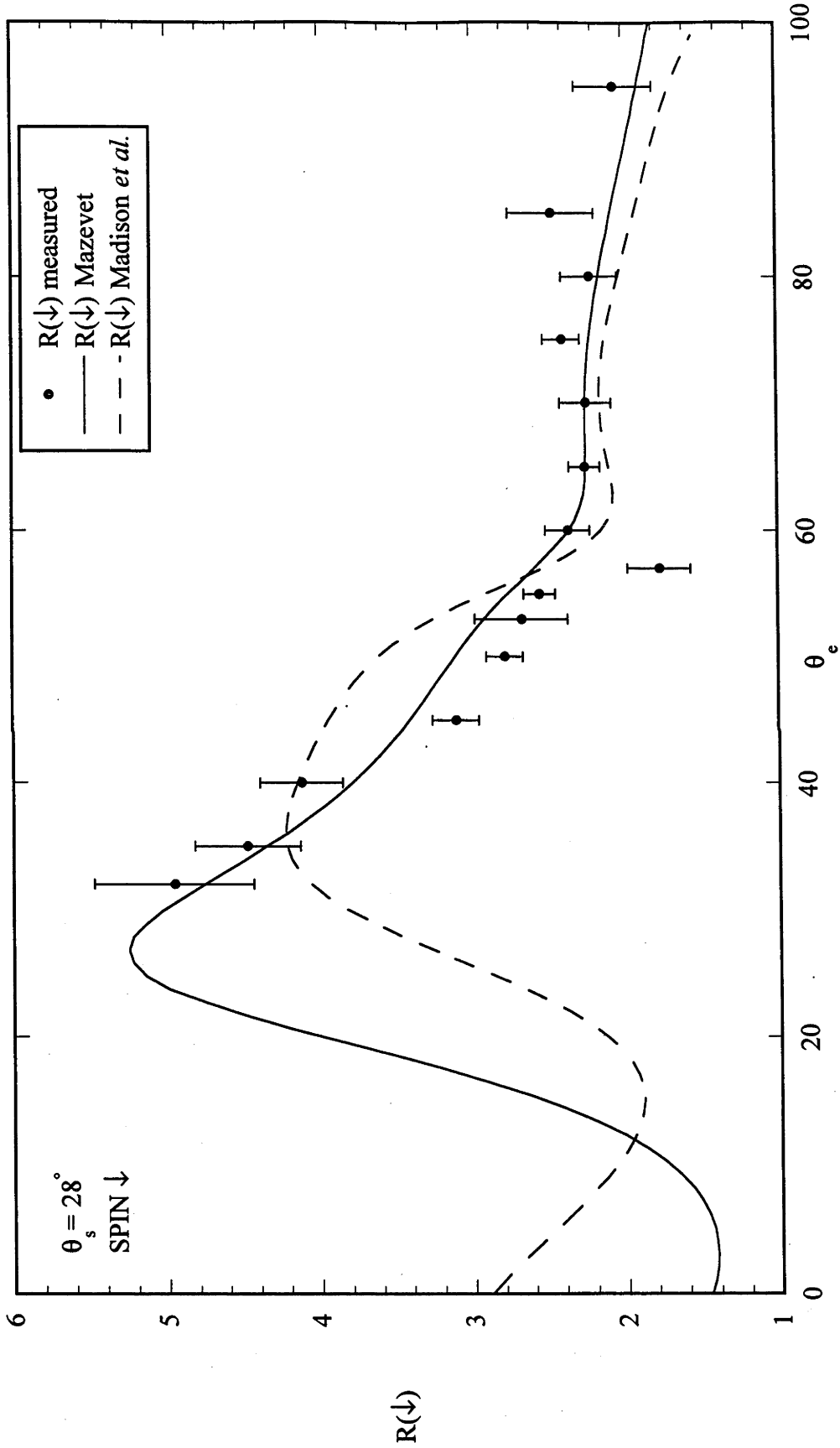
Figure 5.12b: Branching ratios for spin down incident electrons compared to the theories of Mazevet (1996) and Madison *et al.* (1996).
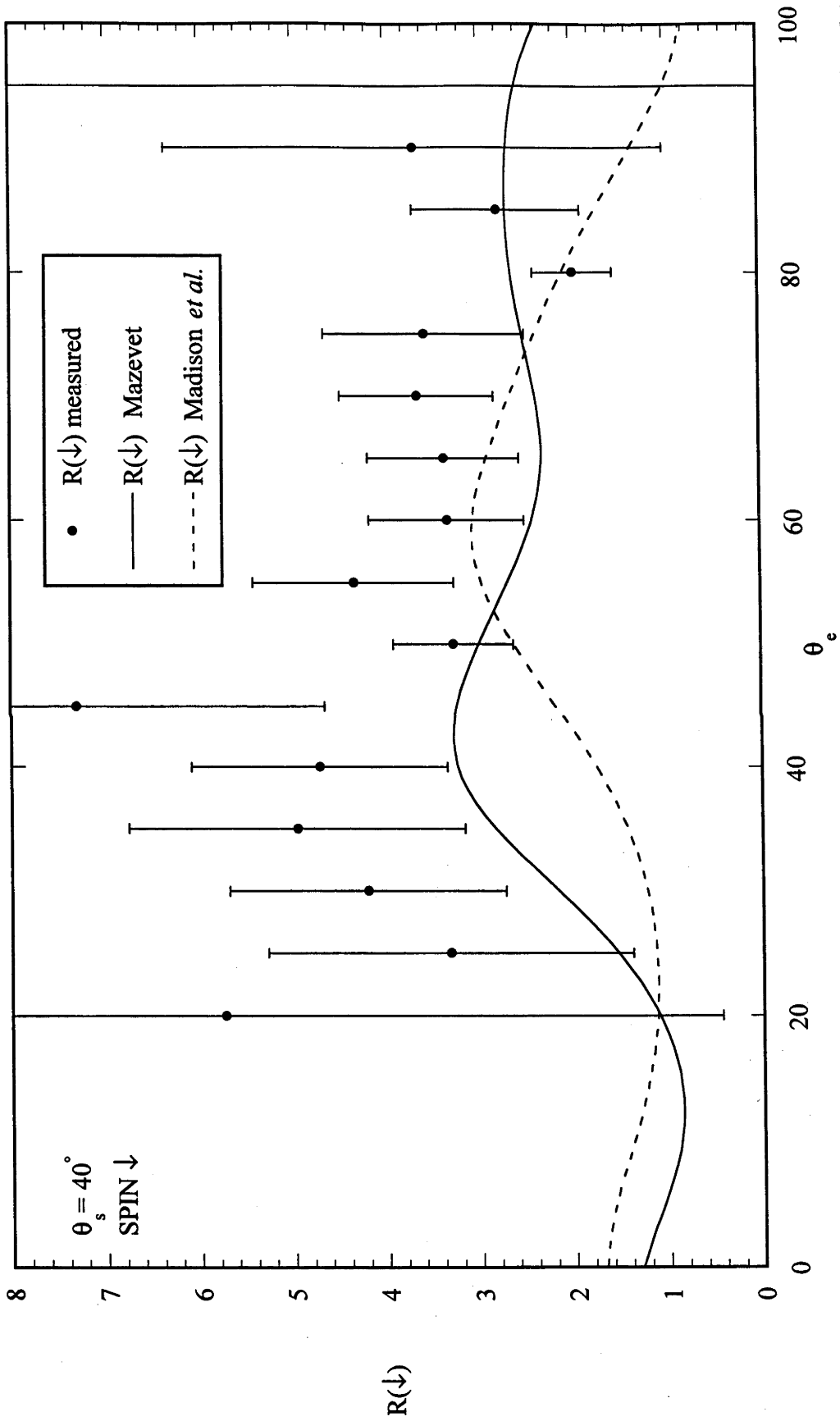
Figure 5.12c: Branching ratios for spin down incident electrons compared to the theories of Mazevet (1996) and Madison *et al.* (1996).
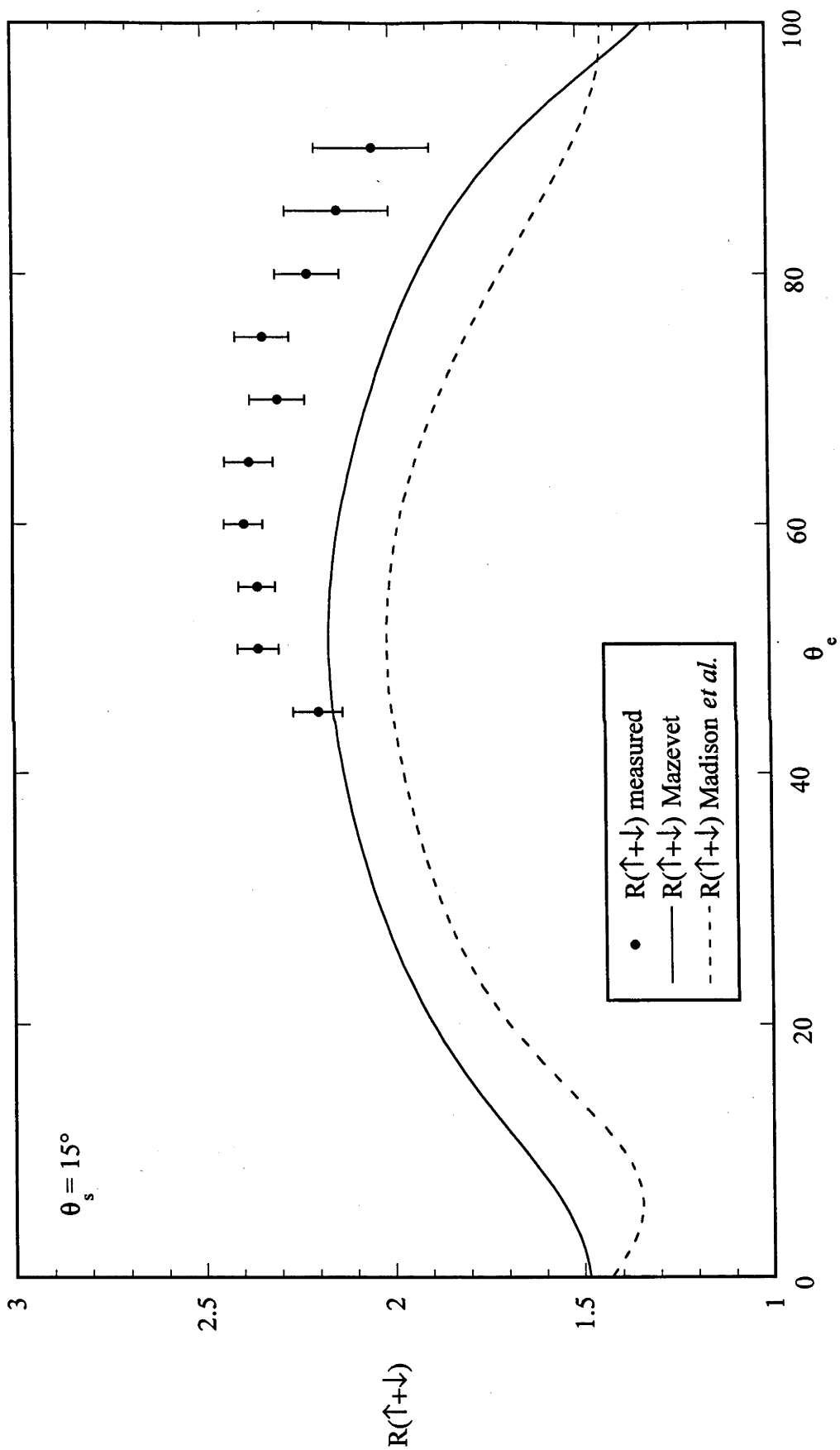
Figure 5.13a: Averaged branching ratios compared to the theories of Mazevet (1996) and Madison *et al.* (1996).
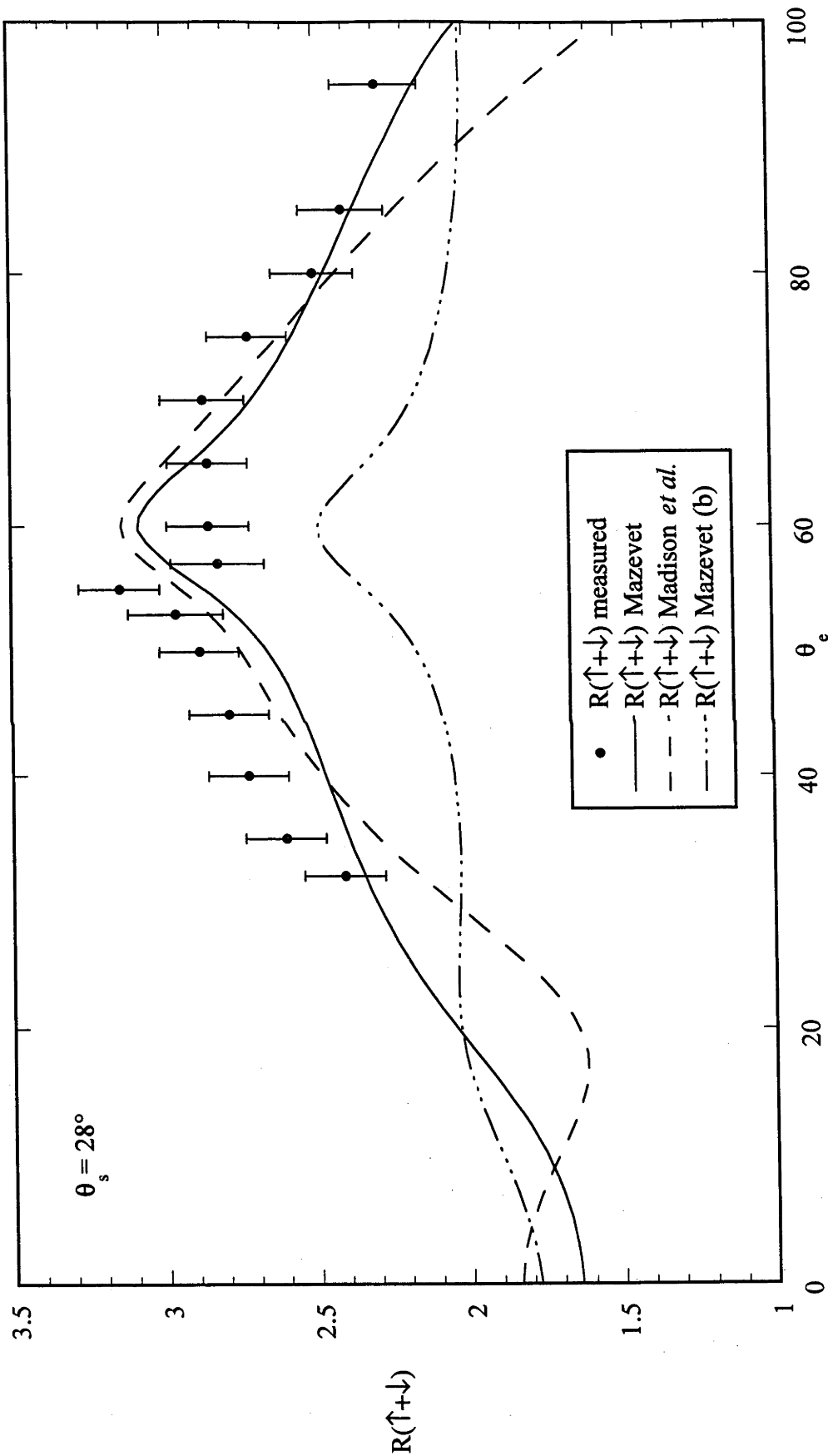
Figure 5.13b: Averaged branching ratios compared to the theories of Mazevet (1996) and Madison *et al.*(1996). Also included in this graph is a Hartree-Fock calculation of Mazevet (labelled Mazevet (b)). See text for details.
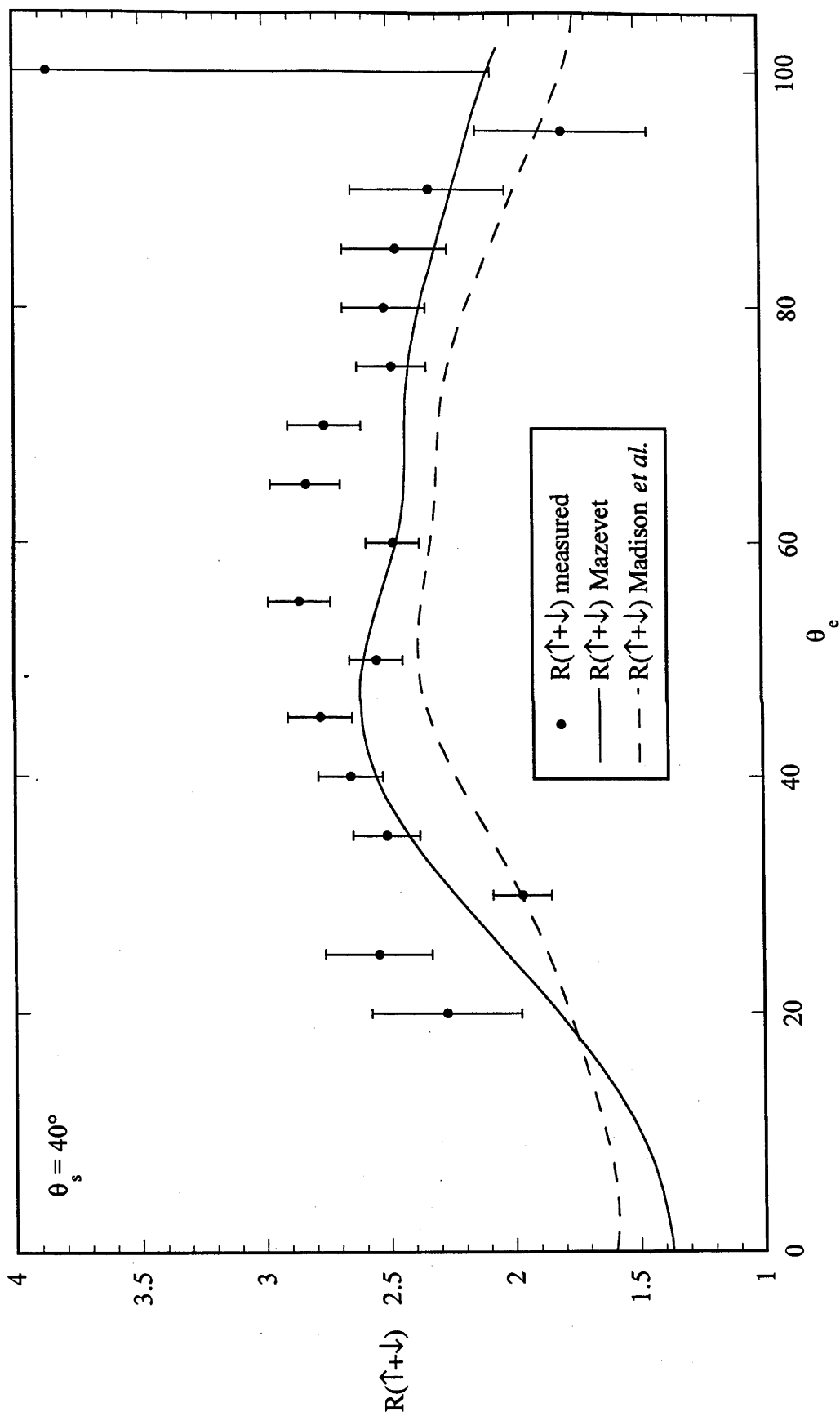
Figure 5.13c: Averaged branching ratios compared to the theories of Mazevet (1996) and Madison *et al.* (1996).

Chapter 6

Summary and Conclusions

An (e,2e) experiment investigating spin effects in electron-atom collisions has been performed. The (e,2e) multiparameter detection technique combined with a polarised electron source was used to investigate the dynamical processes within the electron impact ionisation process. Specifically, the analogue of the fine-structure effect was observed in electron impact ionisation of xenon.

The (e,2e) experiment has been extended to include a spin polarised electron source. The type of polarised electron source used in these experiments is based upon emission of electrons from a GaAs crystal by polarised photons. Spin orbit splitting of the energy bands within the crystal means that it is possible to excite the two different m_l sub-levels by irradiating the crystal with circularly polarised light. In this case a GaAlAs laser diode of wavelength 780nm together with a $\lambda/4$ plate was used to give $\sigma^{\pm}$ light. A negative electron affinity on the crystal surface was produced by layering the surface alternately with caesium and oxygen. The electrons produced have a transverse polarisation which was converted to a longitudinal polarisation by a 90° electrostatic spherical deflector. Transporting the electrons to the experimental region was relatively simple. The transport tube was floated at 1000eV and was protected from magnetic fields by μ-metal shielding.

To be a useful technique, the polarisation of the electron beam must be able to be easily measured. This was done in a Mott polarimeter. By measuring the scattering asymmetries at large backward angles from a high energy electron beam scattered off a gold foil, the polarisation of the incoming electron beam can be deduced. In deriving the electron polarisation, the effective Sherman function is used and due care must be paid to possible asymmetric instrumental responses. The polarisation measured in this experiment is $P = 0.24 \pm 0.03$. The polarisation of the electron beam could be improved by the use of a strained GaAs crystal. This has been reported by Maruyama *et al.* (1992) and Nakanishi *et al.* (1991) as yielding polarisation values up to 90%.

The experiments were conducted in the scattering chamber, where the target, gaseous xenon was introduced via a needle valve. The polarised electron beam was adjusted to yield a current of ~100nA, at the interaction region, as measured in the inner Faraday cup. The cathode voltage for the polarised electron beam was set to 147eV.

Two hemispherical analysers were employed to detect two outgoing electrons in coincidence. These electrons were detected at energies of $35 \pm 3\text{eV}$ and $100 \pm 3\text{eV}$. At the exit planes of the hemispherical analysers was a detection system which included multichannel plates and a resistive anode. From this detection unit pulses were generated which correspond to either energy or timing information. These pulses were synthesised through a variety of electronic units to produce timing and energy spectra, which contained the relevant information. The energy resolution of the (e,2e) spectrum, including the polarised electron source, is 0.6eV. This resolution is good enough to resolve the two peaks corresponding to the $5p^5\ ^2P_{1/2}$ and $^2P_{3/2}$ ground state transitions in xenon.

After collecting the information the data needed to be analysed in a systematic manner. The following set of points is a summary of the analysis procedure as discussed in chapter 5,

* data is extracted, as signal minus background, using an in-house developed program
* each data set is thoroughly checked for any anomalies, *i.e.*, energy drifts
* the energy spectra are corrected for the background transmission function
* the areas under the two peaks are estimated using the globe fit program
* using the sum program, which simply sums all counts in a specified range, these areas are roughly checked for each fine-structure state, to ensure the results are similar to that given by globe fitting the energy spectra
* the errors for each peak are obtained from the sum program (as the errors in globe fit are believed to be inadequate)
* the required parameters are produced for presentation using equations 5.11 → 5.20
* the statistical errors are calculated for each observable *e.g.* as per Bevington (1969)

A series of experiments was conducted at three different kinematic settings. The fast, scattered electron is detected at a fixed angle, which defines the different settings, θ_s = 15°, 28° and 40°. At each fixed, θ_s angle the slow, ejected electron angle θ_e, is scanned according to the physical constraints of the experimental apparatus. Results for each kinematic condition are presented as relative cross sections (total, state resolved and spin resolved), asymmetries and branching ratios.

The two theories which have been used for comparison to the experimental results are discussed. The first is the theoretical calculations of Mazevet (1996) where a semi-relativistic DWBA approach with Dirac-Fock wave functions is used. In this case the distorted waves are calculated in the static exchange potential of the target (or ion) with the addition of the Thomas precession term. The asymmetry in this theory is calculated in the density matrix formalism. The second comparison is with the calculation of Madison, Kravtsov, Jones and McEachran (1995, 1996) (and Jones *et al.*, 1994). The Madison *et al.* (1996) theory calculates the scattering amplitudes with the DWBA using a Dirac-Fock orbital, omitting the spin-orbit interaction term for the continuum electrons.

The aim of this work is to investigate spin effects in electron-atom collisions. The results are presented as an asymmetry parameter and a branching ratio. Also presented are the cross sections which are a relative measure, that is, they are not absolute

measurements, hence a normalisation procedure is necessary. All cross sections (experimental and those calculated by Madison *et al.* (1996)) are normalised to the theory of Mazevet (1996) at $\theta_e = 45°$ on the $^2P_{1/2}$ state resolved cross section. This point was chosen because of the good statistics in the region near the maximum cross section. Note that the asymmetry and branching ratios need not be normalised and provide a direct comparison between the theory and the experimental data.

The cross sections best compared to the theoretical calculations are the spin resolved state resolved cross sections, as the total and state resolved cross sections can be derived from that information. The total cross sections show reasonable agreement with theory in both shape and magnitude at $\theta_s = 15°$ and $40°$, although the poor statistics at $\theta_s = 40°$ may be misleading. At $\theta_s = 28°$ the cross section has two lobes and the theories agree in shape, although there is a difference in magnitude between both theories and the experimental data. At $\theta_s = 28°$ there is also an angular shift of about $5°$ evident between the theoretical calculations and the experimental data.

The trends in agreement between the experimental data and the theories are similar for all state and spin resolved cross sections. In the state resolved cross sections, where transition to the $^2P_{3/2}$ state is about twice as likely as to the $^2P_{1/2}$ state, the agreement between the experimental data and the theory of Mazevet (1996) is better than the theory of Madison *et al.* (1996). For the state resolved cross section at $\theta_s = 15°$ and $\theta_s = 40°$ the theory of Madison *et al.* (1996) underestimates the $^2P_{3/2}$ state contribution, but at $\theta_s = 28°$ the $^2P_{3/2}$ state is overestimated. However, both theories approximate the $^2P_{1/2}$ state cross section well.

In the spin resolved cross section, the effect of the polarised electron beam becomes apparent. The most significant difference is for $\theta_s = 28°$, where there is a clear difference between the spin up cross section and the spin down cross section. For the $^2P_{1/2}$ fine-structure state it is clear that the forward lobe is much larger for spin up incident electrons than for spin down incident electrons. The agreement with the theoretical calculations is very good, although again the theory of Madison *et al.* (1996) overestimates the backward lobe. Conversely, both theories and the experimental data agree that for the $^2P_{3/2}$ fine-structure state the forward lobe is smaller for incident spin up electrons, where the theoretical agreement is the same as for the $^2P_{1/2}$ state.

At $\theta_s = 15°$, the agreement between the theoretical calculations and the experimental data is excellent for the $^2P_{3/2}$ fine-structure state, where the cross section for incident spin down data is slightly smaller than for incident spin up electrons. The agreement with the theory is poorer for the $^2P_{1/2}$ fine-structure state, but the theory of Mazevet (1996) is closer to the experimental data. In this case, the cross section for incident spin down electrons is the smaller of the two spin resolved state cross sections. For $\theta_s = 40°$, the spin down cross section for the $^2P_{1/2}$ fine-structure state is smaller than for incident spin up and conversely, for the $^2P_{3/2}$ fine-structure state the cross section is smaller for incident spin up electrons. The experimental data does not agree well with the theoretical data, although the predictions of Mazevet (1996) are closer to the experimental data.

Spin effects are clearly indicated by the presence of a significant asymmetry for the $\theta_s = 28°$ data. For both the $^2P_{1/2}$ and the $^2P_{3/2}$ fine-structure states there is a significant asymmetry which varies as a function of the ejected electron angle. The density matrix calculation of Mazevet (1996) agrees well with the experimentally determined asymmetry, although the angular shift is again present at this angle. Also at $\theta_s = 28°$, another calculation of Mazevet is presented, which includes the spin-orbit interaction of the continuum electrons for the calculation of the asymmetry for the $^2P_{1/2}$ fine-structure state. This comparison shows that the spin-orbit interaction has a negligible effect on the asymmetry parameter in the region where the experiment is conducted.

At $\theta_s = 15°$ there is evidence of spin polarisation effects, although the asymmetry is small over the range scanned. However, the theory indicates that there may be some interesting asymmetries (*i.e.*, larger asymmetries), at the forward scattering angles. Both theories underestimate the asymmetry for the $^2P_{1/2}$ state, while showing reasonable agreement for the $^2P_{3/2}$ state. At $\theta_s = 40°$ there is an obvious asymmetry, although the agreement with the theoretical calculations is poor. It is at this angle that the two theories disagree the most and where the density matrix formalism method of Mazevet fares best. In both cases ($^2P_{1/2}$ state and $^2P_{3/2}$ state) the measured asymmetry is larger than that predicted by the theory.

In all cases ($\theta_s = 15°$, 28° and 40°) the averaged asymmetry parameter ($A_{1/2}$ + 2$A_{3/2}$)/3, is approximately zero. The largest deviation is at $\theta_s = 40°$, which is a reflection of the small cross section at this angle, (the asymmetry is closet to zero in the region of the largest cross section, between $\theta_e = 35°$ and 75°). Each fine-structure state shows a non-zero asymmetry as a function of the ejected electron angle, but when the fine-structure states are not resolved, *i.e.*, the asymmetry is averaged over the final states, there is essentially no spin dependence. This indicates that the spin effects observed are largely due to the fine-structure effect.

The branching ratio of the fine-structure states is also presented, which in theory, due to the statistical weighting of the states, should be 2. The results show that the polarised branching ratios vary smoothly with the angle of the ejected electron. The greatest variation occurs in the kinematic setting of $\theta_s = 28°$, where the theory agrees quite well with the experimental results, for both spin up and spin down incident electrons. The theory of Mazevet (1996) is in better agreement with the experimental data than the calculations of Madison *et al.* (1996). The calculations of Madison *et al.* (1996) overestimate the spin up branching ratio and underestimates the spin down branching ratio. Again at this kinematics, an angular shift between the theory and the experimentally measured asymmetry is evident.

At $\theta_s = 15°$, there is a marked difference in the agreement between the theoretical calculations and the experimental data. For incident electrons with spin up, the theory predicts consistently lower values than the results show. However, at the same kinematics, but for incident electrons with spin down, the experimental data agrees with the theoretical calculations. In both of these branching ratios the theoretical calculations of Madison *et al.* (1996) are lower than the theoretical predictions of Mazevet (1996). At $\theta_s = 40°$, the theories do not agree with each other, although the theory of Mazevet (1996) predicts the trend of the experimental data. The agreement between the

theoretical calculations of Mazevet (1996) and the experimental data is better for incident spin up electrons than for incident spin down electrons. This kinematics shows that both theories are inadequate in the prediction of the branching ratios.

The unpolarised branching ratios are also presented. As expected these reflect the degree of agreement with the theory by the spin polarised branching ratios. That is, the $\theta_s = 15°$ setting does not agree at all well with the theory, while the $\theta_s = 28°$ data shows excellent agreement with both theories. A calculation of Mazevet (1996), using a Hartree-Fock description of the target states is shown to be inferior to the calculations with Dirac-Fock wave functions. The experimental data at $\theta_s = 40°$ shows a good agreement with the theoretical calculations, although the experimental data shows some scatter. Again, the semi-relativistic calculation of Mazevet (1996) is the better calculation, with respect to agreement with the experimental data. The comparisons with the theory for all branching ratios are a reflection of the agreement between theory and experimental cross section data.

To improve the theoretical calculations it may be necessary for relativistic effects to be included more precisely in the calculations. The average branching ratio calculation at $\theta_s = 28°$ with a Hartree-Fock wave function indicates that a non-relativistic calculation is inadequate. The theory may also improve with the inclusion of more exact collision approximations. In the results shown, the semi-relativistic calculation of Mazevet (1996), which neglects the spin-orbit interaction of the continuum electrons, but includes the exchange interaction between the continuum electrons and the ion, generally agrees well with the data.

Currently the experiment is being fine-tuned before collating more data. It is intended that this new set of experiments will link the results shown in this work together. The next step is to take a set of measurements at a fixed ejected angle and to scan the angle of the scattered electron. This would enable a normalisation across the range of fixed scattered angles presented. Thus all observables would be scaled relative to one kinematic setting.

Appendix A

Derivation of Measured Quantities

As the data analysis was such an important part of this work, it is appropriate to include the steps involved in the derivation of the various quantities. The full set of data is included for each of the three kinematic settings. In each case the polarisation remained the same, P = 0.24. The errors, ΔX, are shown in brackets after the number.

The starting point is the raw data (signal - background) for $\theta_s = 15°$.

$\theta_e^{(o)}$	$N_{1/2}(\uparrow)$	$N_{1/2}(\downarrow)$	$N_{3/2}(\uparrow)$	$N_{3/2}(\downarrow)$
45	14722(176)	14752(176)	32781(233)	31950(231)
50	21224(201)	22535(202)	52362(280)	50631(278)
55	22751(205)	25045(183)	56973(292)	55621(291)
60	22833(202)	24062(204)	56470(286)	55649(285)
65	14258(162)	15304(163)	35521(226)	34733(225)
70	10764(141)	11764(143)	25960(199)	25864(198)
75	12830(162)	13378(162)	30990(222)	30334(221)
80	9450(147)	9573(144)	21639(203)	20594(197)
85	3981(107)	4192(107)	8875(133)	8611(131)
90	3882(117)	3873(117)	7969(143)	7903(142)

Now adjust the for 100% polarisation, as per equations 5.12 and 5.13 (omitting the corresponding errors).

$\theta_e^{(o)}$	$N'_{1/2}(\uparrow)$	$N'_{1/2}(\downarrow)$	$N'_{3/2}(\uparrow)$	$N'_{3/2}(\downarrow)$
45	14675	14800	34097	30634
50	19148	24611	55103	47890
55	19119	28677	59114	53480
60	20887	26008	57770	54349
65	12602	16960	36769	33485
70	9181	13347	26112	25712
75	11962	14246	32029	29295
80	9256	9767	23294	18939
85	3646	4526	9293	8193
90	3896	3860	8074	7798

Appendix A: Derivation of Measured Quantities

The asymmetry parameter is derived using equations 5.14 and 5.16. This is easily checked using equation 5.11 with a polarisation value of P = 0.24. The errors are calculated from equations A.5 and A.6.

$\theta_e^{(o)}$ $(\theta_s=15°)$	$A_{1/2}$	$A_{3/2}$	$\frac{A_{1/2}+2A_{3/2}}{3}$
45	-0.004(0.035)	0.053(0.021)	0.034(0.018)
50	-0.125(0.027)	0.070(0.016)	0.005(0.014)
55	-0.200(0.024)	0.050(0.015)	-0.033(0.013)
60	-0.109(0.025)	0.031(0.015)	-0.016(0.013)
65	-0.147(0.032)	0.047(0.019)	-0.018(0.017)
70	-0.185(0.037)	0.008(0.023)	-0.057(0.019)
75	-0.087(0.036)	0.045(0.021)	0.001(0.019)
80	-0.027(0.045)	0.103(0.028)	0.060(0.024)
85	-0.108(0.077)	0.063(0.044)	0.006(0.039)
90	0.005(0.089)	0.017(0.053)	0.013(0.046)

The branching ratios are calculated using equations 5.17 and 5.18, while the errors are derived using equations A.7 and A.8.

$\theta_e^{(o)}$ $(\theta_s=15°)$	*R(avg)*	*Ratio(↑)*	*Ratio(↓)*
45	2.20(0.02)	2.32(0.10)	2.07(0.09)
50	2.35(0.02)	2.88(0.10)	1.95(0.06)
55	2.36(0.02)	3.09(0.11)	1.86(0.05)
60	2.39(0.02)	2.77(0.09)	2.09(0.06)
65	2.38(0.02)	2.92(0.13)	1.97(0.07)
70	2.30(0.02)	2.84(0.15)	1.93(0.08)
75	2.34(0.02)	2.68(0.12)	2.06(0.08)
80	2.22(0.03)	2.52(0.14)	1.94(0.11)
85	2.14(0.05)	2.55(0.25)	1.81(0.16)
90	2.05(0.05)	2.07(0.22)	2.02(0.22)

Appendix A: Derivation of Measured Quantities

The unnormalised total cross section is from an angular correlation run. The above information yields the unnormalised state resolved cross sections via equations in 5.19 and the associated errors as per equations A.9 and A.10.

$\theta_e^{(o)}$ $(\theta_s=15°)$	$\sigma(total)$	$\sigma_{1/2}$	$\sigma_{3/2}$
45	6686(219)	2092(70)	4594(165)
50	7295(449)	2175(134)	5120(321)
55	7874(491)	2346(147)	5527(350)
60	7614(498)	2245(147)	5368(357)
65	7106(216)	2105(65)	5002(170)
70	5859(198)	1775(61)	4084(154)
75	4500(375)	1347(113)	3152(268)
80	3421(354)	1062(110)	2358(248)
85	1917(131)	611(43)	1306(98)
90	1172(113)	385(38)	787(80)

The state resolved cross sections are derived from equation 5.20 and the associated errors as per equations A.11 and A.12.

$\theta_e^{(o)}$ $(\theta_s=15°)$	$\sigma_{1/2}(\uparrow)$	$\sigma_{1/2}(\downarrow)$	$\sigma_{3/2}(\uparrow)$	$\sigma_{3/2}(\downarrow)$
45	2083(101)	2101(102)	4840(199)	4349(184)
50	1904(132)	2447(162)	5478(353)	4761(310)
55	1877(130)	2816(185)	5804(377)	5251(343)
60	2000(143)	2491(173)	5532(376)	5205(355)
65	1794(88)	2415(101)	5235(201)	4768(188)
70	1447(83)	2104(98)	4115(180)	4052(178)
75	1230(114)	1465(132)	3293(288)	3012(265)
80	1034(117)	1091(123)	2601(281)	2115(232)
85	545(60)	676(67)	1389(119)	1224(108)
90	387(51)	383(51)	801(92)	774(89)

Appendix A: Derivation of Measured Quantities

The raw data (signal-background) for $\theta_s = 28°$.

$\theta_e^{(o)}$	$N_{1/2}(\uparrow)$	$N_{1/2}(\downarrow)$	$N_{3/2}(\uparrow)$	$N_{3/2}(\downarrow)$
32	4620(84)	3760(77)	9690(121)	10538(124)
35	5585(87)	4785(83)	12981(137)	14056(141)
40	6819(93)	5913(88)	17104(145)	17635(147)
45	8119(108)	7886(107)	22079(174)	22566(176)
50	10962(139)	11053(139)	31907(206)	31626(205)
53	995(39)	1082(39)	3034(65)	3122(65)
55	2668(38)	2943(39)	8879(63)	8782(61)
57	941(38)	1108(40)	3003(62)	2783(61)
60	4796(90)	5035(89)	14323(153)	13740(151)
65	7037(101)	7583(103)	21304(164)	20434(161)
70	2848(68)	3105(69)	8698(117)	8387(117)
75	7194(101)	7248(101)	20133(171)	19158(165)
80	2467(61)	2523(61)	6352(80)	6136(79)
85	1660(48)	1587(47)	3974(72)	3839(71)
95	1297(44)	1317(45)	3050(66)	2941(67)

Conversion to 100% polarisation.

$\theta_e^{(o)}$	$N'_{1/2}(\uparrow)$	$N'_{1/2}(\downarrow)$	$N'_{3/2}(\uparrow)$	$N'_{3/2}(\downarrow)$
32	5983	2397	8347	11882
35	6852	3518	11280	15757
40	8254	4478	16264	18476
45	8487	7518	21307	23338
50	10817	11197	32352	31180
53	857	1220	2894	3261
55	2233	3377	9032	8629
57	675	1374	3353	2433
60	4416	5414	15246	12816
65	6172	8448	22681	19056
70	2440	3512	9190	7894
75	7109	7332	21676	17616
80	2380	2610	6692	5796
85	1777	1470	4187	3627
95	1266	1348	3223	2767

Appendix A: Derivation of Measured Quantities

The asymmetry parameter.

$\theta_e^{(o)}$ ($\theta_s=28°$)	$A_{1/2}$	$A_{3/2}$	$\frac{A_{1/2}+2A_{3/2}}{3}$
32	0.428(0.056)	-0.175(0.036)	0.026(0.030)
35	0.321(0.048)	-0.166(0.030)	-0.003(0.026)
40	0.297(0.042)	-0.064(0.025)	0.056(0.022)
45	0.061(0.040)	-0.045(0.023)	-0.010(0.020)
50	-0.017(0.037)	0.018(0.019)	0.007(0.018)
53	-0.175(0.110)	-0.060(0.062)	-0.098(0.055)
55	-0.204(0.040)	0.023(0.021)	-0.053(0.019)
57	-0.341(0.112)	0.159(0.063)	-0.008(0.056)
60	-0.102(0.054)	0.087(0.032)	0.024(0.028)
65	-0.156(0.041)	0.087(0.023)	0.006(0.021)
70	-0.180(0.068)	0.076(0.040)	-0.009(0.035)
75	-0.015(0.041)	0.103(0.025)	0.064(0.022)
80	-0.046(0.072)	0.072(0.037)	0.032(0.035)
85	0.095(0.087)	0.072(0.054)	0.079(0.046)
95	-0.031(0.100)	0.076(0.065)	0.040(0.055)

The branching ratios.

$\theta_e^{(o)}$ ($\theta_s=28°$)	$R(avg)$	$Ratio(\uparrow)$	$Ratio(\downarrow)$
32	2.41(0.04)	1.40(0.08)	4.96(0.52)
35	2.61(0.04)	1.65(0.09)	4.48(0.35)
40	2.73(0.03)	1.97(0.09)	4.13(0.27)
45	2.79(0.03)	2.51(0.12)	3.10(0.15)
50	2.89(0.03)	2.99(0.13)	2.78(0.12)
53	2.96(0.09)	3.38(0.52)	2.67(0.30)
55	3.15(0.03)	4.04(0.23)	2.55(0.10)
57	2.82(0.09)	4.96(0.90)	1.77(0.20)
60	2.85(0.04)	3.45(0.24)	2.37(0.15)
65	2.85(0.03)	3.67(0.20)	2.26(0.10)
70	2.87(0.05)	3.77(0.35)	2.25(0.17)
75	2.72(0.03)	3.05(0.15)	2.40(0.12)
80	2.50(0.05)	2.81(0.24)	2.22(0.18)
85	2.41(0.06)	2.36(0.23)	2.47(0.28)
95	2.29(0.07)	2.55(0.31)	2.05(0.25)

Appendix A: Derivation of Measured Quantities

The unnormalised total cross section is from an angular correlation run. The above information yields the unnormalised state resolved cross sections via equations in 5.19 and the associated errors as per equations A.9 and A.10.

$\theta_e^{(o)}$ $(\theta_s=28°)$	$\sigma(total)$	$\sigma_{1/2}$	$\sigma_{3/2}$
32	3689(160)	1081(48)	2608(134)
35	4704(176)	1304(50)	3400(154)
40	5914(189)	1586(52)	4328(171)
45	5894(189)	1556(51)	4339(170)
50	4905(175)	1262(46)	3642(152)
53	4116(162)	1039(47)	3078(239)
55	3715(156)	896(38)	2819(140)
57	3917(156)	1025(47)	2893(219)
60	4216(161)	1094(43)	3122(155)
65	5225(174)	1355(47)	3869(159)
75	5205(171)	1399(47)	3806(153)
85	2416(125)	709(39)	1707(113)
95	552(24)	168(24)	384(57)

The state resolved cross sections are derived from equation 5.20 and the associated errors as per equations A.11 and A.12.

$\theta_e^{(o)}$ $(\theta_s=28°)$	$\sigma_{1/2}(\uparrow)$	$\sigma_{1/2}(\downarrow)$	$\sigma_{3/2}(\uparrow)$	$\sigma_{3/2}(\downarrow)$
32	1543(92)	618(67)	2153(144)	3064(183)
35	1723(92)	885(72)	2837(165)	3963(207)
40	2057(95)	1116(76)	4053(193)	4604(211)
45	1650(82)	1461(78)	4141(191)	4536(204)
50	1240(65)	1284(66)	3710(169)	3575(164)
53	857(121)	1220(127)	2894(295)	3261(318)
55	713(47)	1078(59)	2884(154)	2755(148)
57	675(119)	1374(131)	3353(311)	2433(258)
60	983(70)	1205(76)	3392(195)	2852(173)
65	1144(68)	1566(77)	4205(194)	3533(170)
75	1377(74)	1421(75)	4200(194)	3413(167)
85	776(75)	642(71)	1829(152)	1584(140)
95	162(28)	173(30)	413(66)	355(53)

Appendix A: Derivation of Measured Quantities

The raw data (signal - background) for $\theta_s = 40°$.

$\theta_e^{(o)}$	$N_{1/2}(\uparrow)$	$N_{1/2}(\downarrow)$	$N_{3/2}(\uparrow)$	$N_{3/2}(\downarrow)$
20	149(23)	121(23)	275(24)	339(24)
25	218(22)	179(21)	533(24)	478(26)
30	351(24)	296(23)	578(26)	695(28)
35	385(24)	314(23)	849(30)	908(31)
40	448(26)	381(25)	1054(33)	1149(34)
45	475(26)	372(24)	1093(33)	1261(35)
50	528(28)	499(27)	1266(35)	1351(36)
55	498(27)	433(25)	1305(36)	1355(37)
60	519(27)	451(26)	1217(34)	1190(34)
65	390(24)	365(24)	1062(32)	1076(33)
70	335(23)	329(22)	854(30)	976(31)
75	313(21)	279(21)	718(27)	752(28)
80	199(18)	244(19)	540(24)	573(24)
85	152(17)	161(17)	361(20)	411(22)
90	91(15)	80(14)	192(16)	207(17)
95	65(13)	47(13)	83(14)	118(15)
100	22(12)	16(12)	74(13)	73(12)

Now adjust the data for 100% polarisation.

$\theta_e^{(o)}$	$N'_{1/2}(\uparrow)$	$N'_{1/2}(\downarrow)$	$N'_{3/2}(\uparrow)$	$N'_{3/2}(\downarrow)$
20	193	77	174	440
25	280	117	620	391
30	438	209	393	880
35	497	202	756	1001
40	554	275	904	1299
45	638	209	827	1527
50	574	453	1131	1486
55	601	330	1226	1434
60	627	343	1260	1147
65	430	325	1040	1098
70	345	320	661	1169
75	367	225	664	806
80	128	315	488	625
85	138	175	282	490
90	108	63	168	231
95	94	19	28	173
100	32	7	76	71

Appendix A: Derivation of Measured Quantities

The asymmetry parameter.

$\theta_e^{(o)}$ $(\theta_s=40°)$	$A_{1/2}$	$A_{3/2}$	$\frac{A_{1/2}+2A_{3/2}}{3}$
20	0.432(0.505)	-0.434(0.232)	-0.146(0.228)
25	0.409(0.319)	0.227(0.147)	0.288(0.145)
30	0.354(0.214)	-0.383(0.125)	-0.137(0.110)
35	0.423(0.198)	-0.140(0.102)	0.048(0.095)
40	0.337(0.181)	-0.180(0.090)	-0.008(0.085)
45	0.507(0.174)	-0.297(0.085)	-0.029(0.081)
50	0.118(0.158)	-0.135(0.080)	-0.051(0.075)
55	0.291(0.164)	-0.078(0.081)	0.045(0.077)
60	0.292(0.161)	0.047(0.083)	0.129(0.077)
65	0.138(0.187)	-0.027(0.090)	0.028(0.086)
70	0.038(0.200)	-0.278(0.098)	-0.173(0.093)
75	0.239(0.209)	-0.096(0.110)	0.016(0.101)
80	-0.423(0.246)	-0.124(0.127)	-0.223(0.118)
85	-0.120(0.320)	-0.270(0.160)	-0.220(0.151)
90	0.268(0.499)	-0.157(0.243)	-0.015(0.232)
95	0.670(0.693)	-0.726(0.427)	-0.260(0.366)
100	0.658(1.884)	0.028(0.501)	0.238(0.711)

The branching ratios.

$\theta_e^{(o)}$ $(\theta_s=40°)$	$R(avg)$	$Ratio(\uparrow)$	$Ratio(\downarrow)$
20	2.27(0.30)	0.90(0.50)	5.74(5.31)
25	2.55(0.21)	2.22(0.59)	3.33(1.95)
30	1.97(0.12)	0.90(0.24)	4.21(1.48)
35	2.51(0.13)	1.52(0.29)	4.97(1.80)
40	2.66(0.13)	1.63(0.29)	4.73(1.37)
45	2.78(0.13)	1.30(0.22)	7.31(2.65)
50	2.55(0.11)	1.97(0.34)	3.28(0.64)
55	2.86(0.13)	2.04(0.33)	4.34(1.07)
60	2.48(0.11)	2.01(0.31)	3.34(0.83)
65	2.83(0.14)	2.42(0.47)	3.37(0.81)
70	2.76(0.15)	1.92(0.47)	3.66(0.83)
75	2.48(0.14)	1.81(0.39)	3.58(1.08)
80	2.51(0.17)	3.82(1.75)	1.98(0.43)
85	2.47(0.21)	2.05(0.89)	2.80(0.90)
90	2.33(0.31)	1.55(0.78)	3.69(2.67)
95	1.79(0.35)	0.30(0.48)	9.37(20.10)
100	3.87(1.79)	2.40(3.03)	10.99(61.73)

Appendix A: Derivation of Measured Quantities

The unnormalised total cross section is from an angular correlation run. The above information yields the unnormalised state resolved cross sections via equations in 5.19 and the associated errors as per equations A.9 and A.10.

$\theta_e^{(o)}$ ($\theta_s=40°$)	$\sigma(total)$	$\sigma_{1/2}$	$\sigma_{3/2}$
20	442(142)	135(45)	307(118)
25	704(141)	199(42)	506(128)
30	960(153)	324(53)	637(113)
35	1228(165)	350(49)	879(145)
40	1516(180)	415(51)	1102(167)
45	1601(181)	424(50)	1177(174)
50	1822(192)	514(56)	1309(172)
55	1796(192)	466(52)	1330(189)
60	1689(185)	485(55)	1204(161)
65	1447(173)	378(47)	1069(170)
70	1247(162)	332(45)	915(155)
75	1031(148)	296(44)	735(129)
80	778(130)	222(38)	557(114)
85	543(116)	157(35)	386(101)
90	286(94)	86(29)	200(79)
95	157(83)	56(31)	101(58)
100	93(74)	19(17)	74(120)

The state resolved cross sections are derived from equation 5.20 and the associated errors as per equations A.11 and A.12.

$\theta_e^{(o)}$ ($\theta_s=40°$)	$\sigma_{1/2}(\uparrow)$	$\sigma_{1/2}(\downarrow)$	$\sigma_{3/2}(\uparrow)$	$\sigma_{3/2}(\downarrow)$
20	193(94)	77(73)	174(98)	440(184)
25	280(86)	117(68)	620(174)	391(124)
30	438(100)	209(77)	393(106)	880(175)
35	497(98)	202(75)	756(154)	1001(188)
40	554(102)	275(83)	904(169)	1299(220)
45	638(105)	209(78)	827(158)	1527(247)
50	574(103)	453(95)	1131(181)	1486(221)
55	601(102)	330(85)	1226(204)	1434(230)
60	627(106)	343(87)	1260(196)	1147(183)
65	430(89)	325(82)	1040(191)	1098(199)
70	345(81)	320(79)	661(143)	1169(217)
75	367(83)	225(71)	664(142)	806(163)
80	128(59)	315(77)	488(123)	625(147)
85	138(59)	175(63)	282(96)	490(142)
90	108(57)	63(48)	168(82)	231(103)
95	94(64)	19(40)	28(46)	173(109)
100	32(45)	7(36)	76(129)	71(122)

The error analysis equations are as follows, where for simplicity the following notation is used, $\Delta^2 X \equiv (\Delta X)^2$.

For 100% polarisation:

$$\Delta^2 N'_J(\uparrow) = \left(\frac{1+P}{2P}\right)^2 \Delta^2 N_J(\uparrow) + \left(\frac{1-P}{2P}\right)^2 \Delta^2 N_J(\downarrow), \qquad \dots \text{A.1}$$

$$\Delta^2 N'_J(\downarrow) = \left(\frac{1-P}{2P}\right)^2 \Delta^2 N_J(\uparrow) + \left(\frac{1+P}{2P}\right)^2 \Delta^2 N_J(\downarrow), \qquad \dots \text{A.2}$$

$$\Delta N'_J = \left(\frac{1}{2}\right)\sqrt{\Delta^2 N_J(\uparrow) + \Delta^2 N_J(\downarrow)} \quad , \qquad \dots \text{A.3}$$

$$\Delta N'_{total} = \sqrt{\Delta^2 N'_{1/2} + \Delta^2 N'_{3/2}} \ . \qquad \dots \text{A.4}$$

This is used to calculate the error for the total cross section for the angular correlation run. $\Delta\sigma_{total}$ is then used in equations A.9 to A.12 to calculate the errors for the state resolved and spin resolved cross sections which have had the asymmetry and ratio parameters folded in.

The errors for the asymmetry:

$$\Delta A_J = \frac{2}{P}\frac{\sqrt{N_J^2(\downarrow)\Delta^2 N_J(\uparrow) + N_J^2(\uparrow)\Delta^2 N_J(\downarrow)}}{\left(N_J(\uparrow) + N_J(\downarrow)\right)^2} \qquad \dots \text{A.5}$$

$$\Delta\left(\frac{A_{1/2} + 2A_{3/2}}{3}\right) = \frac{\sqrt{\Delta^2 A_{1/2} + 4\Delta^2 A_{3/2}}}{3} \qquad \dots \text{A.6}$$

The branching ratio errors are:

$$\Delta^2 R^{(\uparrow)} = \frac{(1+P)^2 \Delta^2 N_{3/2}^{(\uparrow)} + (1-P)^2 \Delta^2 N_{3/2}^{(\downarrow)}}{\left((1+P)N_{1/2}^{(\uparrow)} - (1-P)N_{1/2}^{(\downarrow)}\right)^2} \ +$$

$$\frac{\left((1+P)^2 \Delta^2 N_{1/2}^{(\uparrow)} + (1-P)^2 \Delta^2 N_{1/2}^{(\downarrow)}\right)\left((1+P)N_{3/2}^{(\uparrow)} - (1-P)N_{3/2}^{(\downarrow)}\right)^2}{\left((1+P)N_{1/2}^{(\uparrow)} - (1-P)N_{1/2}^{(\downarrow)}\right)^4} \qquad \dots \text{A.7}$$

Equation A.7 is used to calculate the error, $\Delta R^{(\downarrow)}$, by simply inverting all spin directions.

$$\Delta^2 R = \frac{\Delta^2 N_{3/2}^{(\uparrow)} + \Delta^2 N_{3/2}^{(\downarrow)}}{\left(N_{1/2}^{(\uparrow)} + N_{1/2}^{(\downarrow)}\right)^2} \ + \ \frac{\left(\Delta^2 N_{1/2}^{(\uparrow)} + \Delta^2 N_{1/2}^{(\downarrow)}\right)\left(N_{3/2}^{(\uparrow)} + N_{3/2}^{(\downarrow)}\right)^2}{\left(N_{1/2}^{(\uparrow)} + N_{1/2}^{(\downarrow)}\right)^4} \qquad \dots \text{A.8}$$

Then the errors for the cross sections calculated from the asymmetry and branching ratio information are:

$$\Delta\sigma_{1/2} = \frac{1}{1+R}\sqrt{\Delta^2\sigma_{total} + \frac{\sigma^2_{total}\Delta^2 R}{(1+R)^2}} \qquad \dots A.9$$

$$\Delta\sigma_{3/2} = \frac{1}{1+\frac{1}{R}}\sqrt{\Delta^2\sigma_{total} + \frac{\sigma^2_{total}\Delta^2 R}{R^4\left(1+\frac{1}{R}\right)^2}} \qquad \dots A.10$$

$$\Delta\sigma_J(\uparrow) = \sqrt{(1+A_J)^2\Delta^2\sigma_J + \sigma^2_J\Delta^2 A_J} \qquad \dots A.11$$

$$\Delta\sigma_J(\downarrow) = \sqrt{(1-A_J)^2\Delta^2\sigma_J + \sigma^2_J\Delta^2 A_J} \qquad \dots A.12$$

References

Amaldi, U.Jr., Egidi, A., Marconero, R. and Pizzella, G., *Rev. Sci. Instrum.* **40** (1969) 1001

Anderson, N., Gallagher, J.W. and Hertel, I., *Phys. Rep.* **165** (1988) 1

Bartschat, K., *Comm. At. Mol. Phys.* **27(5)** (1992) 239

Bartschat, K. and Madison, Don H., *J. Phys. B* **21** (1988) 2621

Baum, G., Blask, W., Freienstein, P., Frost, L., Hesse, S., Raith, W., Rappolt, P. and Streun, M., *Phys. Rev. Lett.* **69(21)** (1992) 3037

Baum, G., Moede, M., Raith, W. and Schröder, W., *J. Phys. B* **18** (1985) 531

Bederson, B., *Comm. At. Mol. Phys.* **1** (1969) 41, 65

Berger, O. and Kessler, J., *J. Phys. B* **19** (1986) 3539

Bevington, P.R., *Data Reduction and Error Analysis for the Physical Sciences* (McGraw-Hill, New York) 1969

Brauner, M., Briggs, J.S. and Klar, H., *J. Phys. B* **22** (1989) 2265

Brauner, M., Briggs, J.S., Klar, H., Broad, J.T., Rosel, T., Jung, K. and Ehrhardt, H., *J. Phys. B* **24** (1991) 657

Bray, Igor, Konovalov, Dmitry A. and McCarthy, Ian E., *Phys. Rev. A* **43** (1991) 5878

Bray, Igor and Stelbovics, Andris T., *Adv. At. Mol. Phys.* **35** (1995) 209

Dümmler, M., Barscht, M., Geesmann, H., Hanne, G.F. and Kessler, J., *J. Phys. B* **23** (1990) 3407

Dümmler, M., Hanne, G.F. and Kessler, J., *J. Phys. B* **28** (1995) 2985

Ehrhardt, H., Jung, K., Knoth, G. and Schlemmer, P., *Z. Phys. D* **1** (1986) 3

Ehrhardt, H., Schultz, M., Tekaat, T. and Willmann, K., *J. Phys. B* **22** (1969) 89

Garcia-Rosales, C., Müller, H. and Kessler, J., *J. Phys. B* **21** (1988) L477

Gay, T.J., *J. Phys. B* **16** (1983) L553

References

Gay, T.J. and Dunning, F.B., *Rev. Sci. Instrum.* **63(2)** (1992a) 1635

Gay, T.J., Khakoo, M.A., Brand, J.A., Furst, J.E., Meyer, W.V., Wijayaratna, W.M.K.P and Dunning, F.B., *Rev. Sci. Instrum.* **63(1)** (1992b) 114

Geesmann, H., Bartsch, M., Hanne, G.F. and Kessler, J., *J. Phys. B* **24** (1991) 2817

Granitza, B., Guo, X., Hurn, J.M., Lower, J., Mazevet, S., McCarthy, I.E., Shen, Y. and Weigold, E., *Aust. J. Phys.* **49** (1996) 383

Granitza, B., Guo, X., Hurn, J., Shen, Y. and Weigold, E., *Abstracts of Contributed Papers, XVIII International Conference on the Physics of Electronic and Atomic Collisions,* eds. Anderson, T., Fastrup, B., Folkmann, F. and Knudsen, H. Ahrhus, Denmark (1993) 201

Gulley, R.J., Alle, D.T., Brennan, M.J., Brunger, M.J. and Buckman, S.J., *J. Phys. B* **27** (1994) 2593

Guo, X., private communication (1993)

Guo, X., Hurn, J., Lower, J., Mazevet, S., Shen, Y., McCarthy, I.E. and Weigold, E., *The Physics of Electronic and Atomic Collisions, XIX International Conference,* eds, Dubé, L.J., Mitchell, J.B.A., McConkey, J.W. and Brion, C.E., IOP Press (1995) 795

Guo, X., Hurn, J.M., Lower, J., Mazevet, S., Shen, Y., and Weigold, E., Granitza, B. and McCarthy, I.E., *Phys. Rev. Lett.* **76(8)** (1996) 1228

Hanne, G.F., *Phys. Rep.* **95C** (1983) 95

Hanne, G.F., In *Correlations and Polarization Electronic and Atomic Collisions and (e,2e) Reactions,* eds, Teubner, P.J.O. and Weigold, E., (IOP, Bristol) (1992) 15

Hanne, G.F., McClelland, J.J., Scholten, R.E. and Celotta, R.J., *J. Phys. B* **26** (1993) L753

Hodge, L.A., Moravec, T.J., Dunning, F.B. and Walters, G.K., *Rev. Sci. Instrum.* **50(1)** (1979) 5

Jones, S., Madison, D.H. and Hanne, G.F., *Phys. Rev. Lett.* **72** (1994) 2554

Kessler, J., *Polarised Electrons (2nd edition)* (Springer-Verlag, Berlin) (1985)

Kessler, J., *Adv. At. Mol. and Opt. Phys.* **27** (1991) 81

Kolac, U., Donath, M., Ertl, K., Liebl, H. and Dose, V., *Rev. Sci. Instrum.* **59(9)** (1988) 1933

Kuyatt, C.E. and Simpson, J. Arol, *Rev. Sci. Instrum.* **38** (1967) 103

Lower, J. and Weigold, E., *J. Phys. E* **22** (1989) 421

Madison, D.H., Kravtsov, V.D., Jones, S. and McEachran, R.P., *Can. J. Phys.* (1995) in press

References

Madison, D.H., Kravtsov, V.D., Jones, S. and McEachran, R.P., *Phys. Rev. A* **53(4)** (1996) 2399

Maruyama, T., Garwin, E.L., Prepost, R. and Zapalac, G.H., *Phys. Rev. B* **46(7)** (1992) 4261

Mazevet, S.F., (1996) Australian National University Ph.D. thesis in preparation

McCarthy, I.E., *Aust. J. Phys.* **48** (1995) 1

McCarthy, I.E., Noble, C.J., Phillips, B.A. and Turnbull, A.D., *Phys. Rev. A* **15(6)** (1977) 2173

McCarthy, I.E. and Weigold, E., *Phys. Rep.* **27C** (1976) 275

McCarthy, I.E. and Weigold, E., *Rep. Prog. Phys.* **51** (1988) 299

McCarthy, I.E. and Weigold, E., *Adv. At. Mol. Phys.* **27** (1991a) 201

McCarthy, I.E. and Weigold, E., *Rep. Prog. Phys.* **54** (1991b) 789

McCarthy, I.E. and Weigold, E., *Electron-atom collisions* (Cambridge University Press) (1995)

McClelland, J.J., Kelley, M.H. and Celotta, R.J., *Phys. Rev. Lett.* **58(21)** (1987) 2198

McClelland, J.J., Kelley, M.H. and Celotta, R.J., *Phys. Rev. A* **40** (1989a) 2321

McClelland, J.J., Scheinfein, M.R. and Pierce, D.T., *Rev. Sci. Instrum.* **60(4)** (1989b), 683

Müller, H. and Kessler, J., *J. Phys. B* **27** (1994) 5893

Nakanishi, T., Aoyagi, H., Horinaka, H., Kamiya, Y., Kato, T., Nakamura, S., Saka, T. and Tsubata, M., *Phys. Lett. A* **158** (1991) 345

Nickich, V., Hegemann, T., Bartsch, M. and Hanne, G.F., *Z. Phys. D.* **16** (1990) 261

Pierce, D.T., Celotta, R.J., Wang, G.-C., Unertl, W.N., Galejs, A., Kuyatt, C.E. and Mielczarek, S.R., *Rev. Sci. Instrum.* **51(4)** (1980) 478

Pierce, D.T., Meier, F. and Zürcher, P., *Phys. Lett.* **51A** (1975) 465

Prinz, H.-Th., Besch, K.-H. and Nakel, W., *Phys. Rev. Lett.* **74(2)** (1995) 243

Ross, A.W. and Fink, M., *Phys Rev. A,* **38(12)** (1988) 6055

Samardzic, O., Brunger, M.J., Grisogono, A-M. and Weigold, E., *J. Phys. B* **26** (1993) 3921

Scheer, J.J. and van Laar, J., *Solid State Comm.* **3** (1965) 189

References

Shen, Y., *Spin-Resolved (e, 2e) Collisions* (1995) Australian National University Ph.D. thesis

Shi, Z., Ying, C.H. and Vuškovic, L., *Phys. Rev. A* **53** (1996) R16

Sin Fai Lam, L.J., *Aust. J. Phys.* **33** (1980) 261

Sohn, M. and Hanne, G.F., *J. Phys. B* **25** (1992) 4627

Stefani, G., Avaldi, L. and Camilloni, R., *Journal De Physique IV* **3** (1993) 1

Tang, F.C., Lubell, M.S., Rubin, K., Vasilakis, A., Eminyan, M. and Slevin, J., *Rev. Sci. Instrum.* **57(12)** (1986) 3004

Uhrig, M., Beck, A., Goeke, J., Eschen, F., Sohn, M., Hanne, G.F., Jost, K. and Kessler, J., *Rev. Sci. Instrum.* **60(5)** 1989 872

Uhrig, M., Hanne, G.F. and Kessler, J., *J. Phys. B* **27** (1994) 4009

van den Brink, J.P., Nienhuis, G., van Eck, J. and Heideman, H.G.M., *J. Phys. B* **22** (1989) 3501

Vos, M., Storer, P., Cai, Y.Q., McCarthy, I.E. and Weigold, E., *Phys. Rev. B* **51** (1995) 1866

Zhang, X., Whelan, Colm T. and Walters, H.R.J., *J. Phys. B* **25** (1992) L457

Zheng, Y., *Electron Momentum Spectroscopy of Molecules and Laser Excited Atoms* (1989) Flinders University of S.A. Ph.D. thesis

Zheng, Y., McCarthy, I.E., Weigold, E. and Zhang, D., *Phys. Rev. Lett.* **64** (1990) 1358

Zheng, Y., Neville, J.J. and Brion, C.E., *Science* **270** (1995) 786